

Eidesstattliche Erklärung

Ich erkläre an Eides statt, dass ich die vorliegende Arbeit selbstständig verfasst, andere als die angegebenen Quellen/Hilfsmittel nicht benutzt, und die den benutzten Quellen wörtlich und inhaltlich entnommenen Stellen als solche kenntlich gemacht habe.

Graz, am

.....

(Unterschrift)

Statutory declaration

I declare that I have authored this thesis independently, that I have not used other than the declared sources / resources, and that I have explicitly marked all material which has been quoted either literally or by content from the used sources.

Graz,

.....

(signature)

Danksagung

Ich möchte mich recht herzlich bei meinem Betreuer Prof. Helmut F. Schweiger, der mich während des Verfassens dieser Arbeit immer tatkräftig und fachlich unterstützt hat, bedanken. Außerdem blicke ich gerne auf die interessanten Vorlesungen zurück, die mich von der Geotechnik überzeugt haben.

Des Weiteren möchte ich meinen Eltern, die mir das Studium in Graz überhaupt ermöglicht haben, danken. Auch bei meiner Schwester, die meine Arbeit korrigiert hat, möchte ich mich bedanken.

Den Mitgliedern und Freunden des Stahlbauzeichensaales, in dem ich einige Stunden während meines Studiums verbracht habe, gebührt auch ein großer Dank. Es waren viele nette Stunden, die wir beim Feiern oder Lernen gemeinsam verbracht haben. Auf diese Zeit werde ich mich bestimmt noch oft zurück erinnern.

Meinen Kollegen im Bodenmechanik „Kammerl“ danke ich auch besonders für die oft konstruktiven Diskussionen während des Verfassen meiner Arbeit.

Kurzfassung

In der Geotechnik werden für Baugrundverbesserungen bzw. Gründungselemente oft säulenartige Strukturelemente verwendet. Zu diesen zählen mixed-in-place Säulen und Düsenstrahlsäulen. Im Standardfall sind diese Säulen unbewehrt und daher sensibel bezüglich Biegung und Zug. Aus diesem Grund ist es notwendig, um die Auswirkungen von Einschnürungen, Lastexzentrizität, Schiefstellung und Krümmung von Säulen zu beurteilen, ein hochwertiges Stoffgesetz anzuwenden. Dabei handelt es sich um das shotcrete model, welches die zeitabhängige Festigkeit und Steifigkeit des Betons berücksichtigt. Außerdem ist es möglich ein Rissbild der belasteten Säule zu plotten. Zum einen haben Risse im Beton keinen großen Einfluss auf den Sicherheitsfaktor, zum anderen ist es jedoch eine wichtige zusätzliche Information für die Dimensionierung von solchen Bauten. Ziel dieser Arbeit ist die Untersuchung von Last-Setzungs-Kurven einer Säule mit verschiedenen Imperfektionen in einem weichen Boden. Zusätzlich werden die vertikalen Spannungen und die effektive Hauptnormalspannung σ'_3 (nur Zug) der verschiedenen Stoffgesetze verglichen. Von Interesse sind auch die Normalkraftverläufe und die Momentenverläufe in der Säule die sich aus den verschiedenen Stoffgesetzen ergeben.

Abstract

For ground improvement, columnlike structural elements are often used. These include mixed-in-place columns and jet grouting techniques. Usually these columns are not reinforced and therefore sensitive concerning bending and tension. Due to this reason, a more sophisticated constitutive model should be used to assess the consequence of effects such as necking and bulging, load eccentricity, inclination and curvature of columns. The shotcrete model, which takes time dependent strength and stiffness into account is used in this thesis. Furthermore, it is possible to plot the crack pattern of the columns. On the one hand cracks in concrete usually do not have a large impact on the safety factor of the structure, but on the other hand it is important to have this information for designing such structures. Aim of this thesis is to investigate the load–settlement behavior of a column with different imperfections in a soft soil layer. In addition, vertical stresses and the principle effective stresses σ'_3 (only tension) from different constitutive models are compared. The structural forces in the column obtained from the Mohr Coulomb model are compared to the structural forces, obtained from the shotcrete model.

Table of contents

1	Introduction	1
2	Shotcrete model for ground improvement techniques	2
2.1	Parameters of the shotcrete model.....	2
2.2	Yield surfaces and strain hardening/softening.....	3
2.3	Time dependent stiffness and strength.....	4
3	General information about 2D and 3D models used.....	5
3.1	2D-Model	5
3.1.1	Calculation phases	6
3.1.2	Soil parameters	6
3.2	3D-Model	9
3.2.1	Calculation phases and input parameters	10
4	Necking and Bulging	12
4.1	Necking.....	13
4.1.1	Load-settlement curves	13
4.1.2	Vertical stresses and principal effective stresses σ'_3	14
4.1.3	Crack pattern for columns with necking.....	17
4.2	Bulging.....	19
4.2.1	Load-settlement curves	19
4.2.2	Vertical stresses and principal effective stresses σ'_3	20
5	Inclination.....	22
5.1	Load-settlement curves	23
5.2	Vertical stresses and principal effective stresses σ'_3	25
5.3	Crack pattern for columns with inclination $e = 10 \% D$	27
5.4	Normal force and bending moment	29
5.5	Activation of the “updated mesh” option	30
6	Load eccentricity	32
6.1	Load-settlement curves	32
6.2	Vertical stresses	33

6.3	Normal force and bending moment.....	35
7	Curvature	36
7.1	Load-settlement curves.....	36
7.2	Vertical stresses and principal effective stresses σ'_3	37
7.3	Normal force and bending moment.....	39
7.4	Activation of the “updated mesh” option	39
7.5	Curved column with $r = 50$ m	42
7.6	Load-settlement curves.....	42
7.7	Vertical stresses.....	43
8	Conclusion	45
9	Embankment.....	47
9.1	Model for <i>FEM</i> analysis in PLAXIS 2D	47
9.1.1	Calculation phases	47
9.1.2	Soil parameters.....	48
9.2	<i>FEM</i> analysis with columns modelled as “block” with “smeared properties” ..	52
9.3	<i>FEM</i> analysis with columns modelled as “wall”	54
9.4	<i>FEM</i> analysis with columns modelled as plate	58
9.5	<i>FEM</i> analysis with columns modelled as embedded beam row	60
9.6	3D <i>FEM</i> analysis.....	62
10	Conclusion.....	65
11	Literature	66
12	Appendix A: Inclined Columns.....	I
13	Appendix B: Load-settlement trough embankment	VIII

List of figures

Fig. 1	Yield surfaces and failure envelope of the model (Schweiger et al., 2014)	3
Fig. 2	Normalized stress – strain curve in compression (Schweiger et al., 2014)	4
Fig. 3	Normalized stress – strain curve in tension (Schweiger et al., 2014)	4
Fig. 4	Axisymmetric model.....	6
Fig. 5	3D model	10
Fig. 6	Necking and bulging imperfections (Bohn, 2015)	12
Fig. 7	Necking and bulging with the interface following the shape of the column.....	12
Fig. 8	Load-settlement curves with necking for $B = 0.3$ m (linear elastic).....	13
Fig. 9	Load-settlement curves with necking for $B = 0.3$ m (shotcrete model).....	14
Fig. 10	Vertical stresses for necking at $0.25 D$ (<i>LE</i> and <i>SCM</i>).....	15
Fig. 11	Principal effective stresses σ'_3 (tensile stresses) for necking at $0.25 D$ (<i>LE</i> and <i>SCM</i>)	16
Fig. 12	Principal effective stresses σ'_3 (tensile stresses) for necking at $0.5 D$ (<i>LE</i> and <i>SCM</i>)	16
Fig. 13	Principal effective stresses σ'_3 (tensile stresses) for necking at $0.75 D$ (<i>LE</i> and <i>SCM</i>)	17
Fig. 14	Crack pattern - $G_{t,28} = 0.01$ for necking at $0.25 D$	18
Fig. 15	Crack pattern - $G_{t,28} = 0.01$ for necking at $0.5 D$	18
Fig. 16	Load-settlement curves with bulging for $B = 0.3$ m (<i>LE</i>)	19
Fig. 17	Load-settlement curves with bulging for $B = 0.3$ m (<i>SCM</i>).....	20
Fig. 18	Vertical stresses for bulging at $0.25 D$ (<i>LE</i> and <i>SCM</i>).....	21
Fig. 19	Principal effective stresses σ'_3 (tensile stresses) for bulging at $0.25 D$ (<i>LE</i> and <i>SCM</i>)	21
Fig. 20	Inclination levels from 1 % up to 10 % of D (Bohn, 2015).....	22
Fig. 21	Top view of an inclined column with cross section A - A.....	22
Fig. 22	Load-settlement curves with column inclination for $B = 0.3$ m (<i>MC</i>)	23
Fig. 23	Load-settlement curves with column inclination for $B = 0.3$ m (<i>SCM</i>).....	24
Fig. 24	Load-settlement curves with inclination for $B = 0.3$ m (<i>MC</i> and <i>SCM</i>).....	24
Fig. 25	Vertical stresses in the column for $e = 10\%$ D (<i>MC</i> and <i>SCM</i>)	25
Fig. 26	A – A: stress points with interpolation error for $e = 10\%$ D (<i>MC</i> and <i>SCM</i>).....	26
Fig. 27	A – A: principal effective stresses σ'_3 (tensile stresses) for <i>MC</i> and <i>SCM</i>	27
Fig. 28	A – A: Crack pattern - $G_{t,28} = 0.01$	28
Fig. 29	A – A: Crack pattern - $G_{t,28} = 0.05$	28
Fig. 30	Structural forces for a column with $e = 10\%$ D (<i>MC</i> and <i>SCM</i>).....	29

Fig. 31	Structural forces for a column with $e = 10 \% D$ for different $G_{t,28}$ values (MC and SCM)	30
Fig. 32	Load-settlement curves with activation of the „updated mesh“ option (MC and SCM)	31
Fig. 33	A – A: Crack pattern - $G_{t,28} = 0.01$	31
Fig. 34	Load eccentricity for $e = 1/8 B$ and $e = 1/7 B$	32
Fig. 35	Load-settlement curves for load eccentricity (MC and SCM)	33
Fig. 36	Vertical stresses for load eccentricity $B/8$ (MC and SCM)	34
Fig. 37	Tensile stresses for load eccentricity $B/7$ (MC and SCM)	34
Fig. 38	Structural forces for a column with load eccentricity for $e = 1/8$ & $1/7 B$ (MC and SCM)	35
Fig. 39	Column with different curvatures for 3D FEM calculation	36
Fig. 40	Load-settlement curves for columns with curvature (MC and SCM)	37
Fig. 41	Vertical stresses for curvature $r = 100$ m (MC and SCM)	38
Fig. 42	Principal effective stresses σ'_3 for curvature $r = 100$ m (MC and SCM)	38
Fig. 43	Structural forces for curved column with $r = 100$ m (MC and SCM)	39
Fig. 44	Load-settlement curves with curvature and “updated mesh“ option (SCM)	40
Fig. 45	Vertical stresses for curvature $r = 100$ m with “updated mesh“ option (MC and SCM)	41
Fig. 46	Principal effective stresses σ'_3 (tensile stresses) with „updated mesh“ option (MC and SCM)	41
Fig. 47	Comparison of the structural forces with „updated mesh“ option (MC and SCM)	42
Fig. 48	Load-settlement curves for curvature $r = 50$ m (MC and SCM)	43
Fig. 49	Vertical stresses for curvature $r = 50$ m (MC and SCM)	44
Fig. 50	Crack pattern – $G_{t,28} = 0.01$	44
Fig. 51	Soil profile for analysis	47
Fig. 52	phases explorer	48
Fig. 53	FEM model with exchanged “block” with “smeared properties”	52
Fig. 54	Settlement trough for “block” with “smeared properties”	53
Fig. 55	FEM model for columns modelled like a “wall”	54
Fig. 56	Plane strain approach	55
Fig. 57	Deformed mesh $ u $	56
Fig. 58	Normal stress distribution of the columns	57
Fig. 59	Settlement trough on top of the columns	57
Fig. 60	Stamping in of the columns in the LTP	58
Fig. 61	FEM model for columns modelled like a plate	58

Fig. 62	Deformed mesh $ u $	59
Fig. 63	Settlement trough on top of the plates	60
Fig. 64	<i>FEM</i> model for columns modelled with an embedded beam row	60
Fig. 65	Deformed mesh $ u $	61
Fig. 66	Settlement trough on top of the embedded beam row	62
Fig. 67	<i>3D</i> model.....	62
Fig. 68	Settlement trough on top of the columns	63
Fig. 69	Comparison of the settlement trough for different stiffness of the LTP	63
Fig. 70	Load-settlement trough on top for all different types of calculations	64
Fig. 71	Structural forces for a column with $e = 5 \% D$ (<i>MC</i> and <i>SCM</i>)	I
Fig. 72	Structural forces for a column with $e = 3 \% D$ (<i>MC</i> and <i>SCM</i>)	II
Fig. 73	Structural forces for a column with $e = 2 \% D$ (<i>MC</i> and <i>SCM</i>)	II
Fig. 74	Structural forces for a column with $e = 1 \% D$ (<i>MC</i> and <i>SCM</i>)	III
Fig. 75	Vertical stresses in the column for $e = 5 \% D$ (<i>MC</i> and <i>SCM</i>)	III
Fig. 76	Vertical stresses in the column for $e = 3 \% D$ (<i>MC</i> and <i>SCM</i>)	IV
Fig. 77	Vertical stresses in the column for $e = 2 \% D$ (<i>MC</i> and <i>SCM</i>)	IV
Fig. 78	Vertical stresses in the column for $e = 1 \% D$ (<i>MC</i> and <i>SCM</i>)	V
Fig. 79	Principal effective stresses σ'_3 (only tension) for $e = 5 \%$ (<i>MC</i> and <i>SCM</i>)	V
Fig. 80	Principal effective stresses σ'_3 (only tension) for $e = 3 \%$ (<i>MC</i> and <i>SCM</i>)	VI
Fig. 81	Principal effective stresses σ'_3 (only tension) for $e = 2 \%$ (<i>MC</i> and <i>SCM</i>)	VI
Fig. 82	Principal effective stresses σ'_3 (only tension) for $e = 1 \%$ (<i>MC</i> and <i>SCM</i>)	VII
Fig. 83	Settlement trough below the columns	VIII
Fig. 84	Settlement trough below the plates	VIII
Fig. 85	Settlement trough below the embedded beam row	IX
Fig. 86	Load-settlement trough below the columns for all examples	IX

List of tables

Tab. 1	Parameters of the shotcrete model.....	2
Tab. 2	Input parameters for soft soil layer	7
Tab. 3	Input parameters for stiff soil layer.....	7
Tab. 4	Input parameters for the column.....	7
Tab. 5	Input parameters for the shotcrete model.....	8
Tab. 6	Mohr Coulomb input parameters for the column	11
Tab. 7	Soil properties fill	48
Tab. 8	Soil properties alluvial sand	49
Tab. 9	Soil properties lower clay.....	50
Tab. 10	Soil properties residual clay	50
Tab. 11	Soil properties alluvial sediments.....	51
Tab. 12	Soil properties LTP.....	52
Tab. 13	Properties of the “block” below the embankment.....	53
Tab. 14	Properties of the column	54
Tab. 15	Plate properties	58
Tab. 16	Embedded beam row properties	61

List of symbols and abbreviations

Capital letters

B	[m]	width of the column
D	[m]	length of the column
D'	[m]	diameter of the column in a unit cell
E	[N/m ²]	Young's modulus
F_c	[-]	yield surface for deviatoric loading
F_t	[-]	yield surface in the tensile regime
G_c	[-]	fracture energy in compression
G_t	[N/m]	fracture energy in tension
$G_{t,28}$	[N/m]	fracture energy in tension after 28d
H_c	[-]	normalized hardening/softening parameter
H_t	[-]	normalized tension softening parameter
K_0	[-]	earth pressure coefficient
R	[N]	resultant force
R_{inter}	[-]	strength reduction factor

Small letters

c'	[N/m ²]	cohesion
f_t	[N/m ²]	tensile strength
$f_{t,28}$	[N/m ²]	uniaxial tensile strength after 28d
f_c	[N/m ²]	compressive strength
r	[m]	radius of curvature

Greek letters

γ	[N/m ³]	unit weight
ε_{cp}^p	[-]	plastic peak strain in uniaxial compression
ν	[-]	Poisson's ratio
σ'_3	[N/m ²]	major principle effective stress
φ^{\max}	[°]	maximum friction angle
ψ'	[°]	dilatancy angle

Abbreviations

<i>2D</i>	two-dimensional
<i>3D</i>	three-dimensional
<i>FEM</i>	Finite Element Method
<i>HS</i>	Hardening Soil
<i>HSS</i>	Hardening Soil small
<i>LE</i>	linear elastic
<i>LTP</i>	load transfer platform
<i>MC</i>	Mohr Coulomb
<i>SCM</i>	shotcrete model
<i>SSC</i>	Soft Soil Creep Model

1 Introduction

This thesis is dealing with imperfections in grouted columns. Imperfections like necking and bulging, inclination, curvature and load eccentricity can appear because of inaccurate work in the field and difficult ground conditions. Of course, the diameter of the columns that are used for ground improvement techniques plays a significant role on the bearing capacity. Columns with a smaller diameter in combination with imperfections are more sensitive concerning structural failure. For this reason, a single non-reinforced column with a diameter of 0.3 m is used in a *2D* and *3D FEM* analysis in PLAXIS. The consequence of loaded columns with imperfections are tensile stresses in different areas of the column and consequently cracks in concrete.

Numerical analysis of imperfections in grouted columns in soft soil conditions have been presented in different literatures. The bearing capacity and the load-settlement behavior of a single non-reinforced column is investigated assuming a linear elastic behavior and the Mohr Coulomb model. Result of these investigations reveal that none of the geometrical imperfections has a significant negative impact on the bearing capacity of the single column. Even a small increase of bearing capacity due to a passive soil support is apparent in some of the load-settlement curves. (Bohn, 2015)

It should be mentioned that constitutive models like Mohr Coulomb and a linear elastic behavior are not suitable to describe the mechanical behavior of unreinforced concrete, especially when the tensile strength is exceeded. (Schweiger, Sedighi, Henke, & Borchert, 2014) For this reason, it is necessary to use a more sophisticated model like the shotcrete model, which takes time dependent strength and stiffness, crack formation due high tensile stresses and tension/compression softening into account. The bearing capacity and the load-settlement curves are examined in order to compare it with simpler models mentioned above.

2 Shotcrete model for ground improvement techniques

The shotcrete model is a constitutive model, which is developed especially for numerical simulations of shotcrete and ground improvement techniques. It takes time dependent strength and stiffness, as well as creep and shrinkage of concrete into account. (Schweiger et al., 2014)

2.1 Parameters of the shotcrete model

Tab. 1 represents the parameters of the shotcrete model. It is important that these parameters have to be determined individually for each project. (Schweiger et al., 2014)

Tab. 1 Parameters of the shotcrete model

Name	Unit	Remarks
E_{28}	[GPa]	Young's modulus after 28d
ν	[-]	Poisson's ratio
$f_{c,28}$	[KN/m ²]	uniaxial compressive strength after 28d
$f_{t,28}$	[KN/m ²]	uniaxial tensile strength after 28d
ψ	[°]	angle of dilatancy
E_1/E_{28}	[-]	ratio of Young's modulus after 1d and 28d
$f_{c,1}/f_{c,28}$	[-]	ratio of f_c after 1d and 28d
$f_{c0,n}$	[-]	normalized initial yield stress (compr.)
$f_{cf,n}$	[-]	normalized failure strength (compr.)
$f_{cu,n}$	[-]	normalized residual strength (compr.)
ϵ_{cp}^p at 1 h	[-]	plastic peak strain in uniaxial compr. at shotcrete ages 1h
ϵ_{cp}^p at 8 h	[-]	plastic peak strain in uniaxial compr. at shotcrete ages 8h
ϵ_{cp}^p at 24 h	[-]	plastic peak strain in uniaxial compr. at shotcrete ages 24h
$G_{c,28}$	[KN/m]	fracture energy in compression after 28 d
$f_{tu,n}$	[-]	normalized residual tensile strength
$G_{t,28}$	[KN/m]	fracture energy in tension after 28d
L_{eq}	[m]	equivalent length

a	[-]	increase of ε_{cp} with increase of p'
φ^{\max}	[°]	maximum friction angle
γ_{fc}	[-]	safety factor for compr. strength
γ_{ft}	[-]	safety factor for tensile strength
t_{hydr}	[day]	time for full hydration

2.2 Yield surfaces and strain hardening/softening

The shotcrete model is based on a Mohr Coulomb yield surface F_c for deviatoric loading and a Rankine yield surface F_t , which is shown in Fig. 1. σ_{rot} describes the intersection of the Mohr-Coulomb failure line with the isotropic axis. Strain hardening/softening elastoplasticity is used to compute plastic strains.

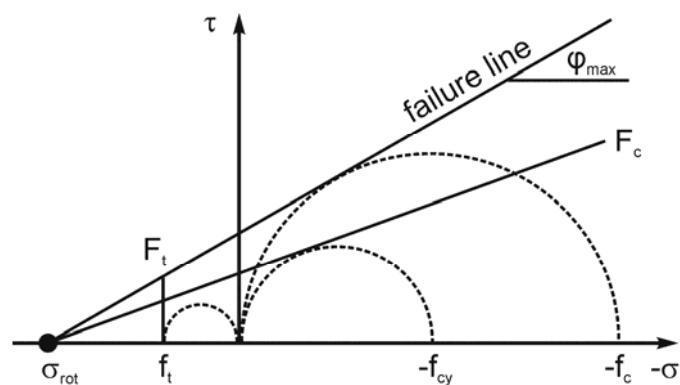


Fig. 1 Yield surfaces and failure envelope of the model (Schweiger et al., 2014)

Fig. 2 represents the hardening and softening process in compression. At first, quadratic strain hardening occurs and is followed by bilinear softening. H_c is a normalized softening parameter, which is involved due to time dependent material parameters. G_c describes the fracture energy in compression.

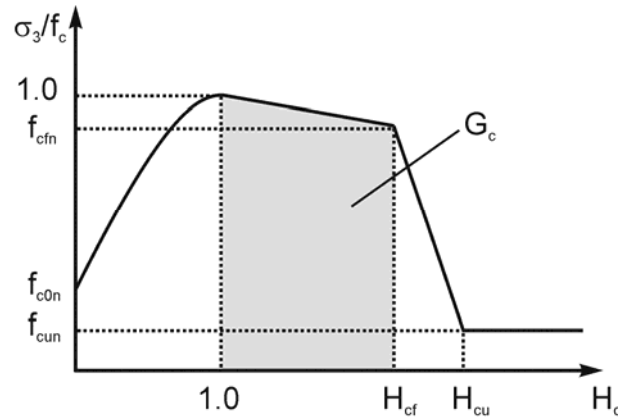


Fig. 2 Normalized stress – strain curve in compression (Schweiger et al., 2014)

In tension the model behaves different compared to compression. A linear elastic behavior can be noted until the tensile strength f_t is reached. Then linear strain softening, which is influenced by the major principal plastic strain and the fracture energy G_t (Fig. 3), takes place. A G_t value of 0.01 represents a rather brittle concrete whereas a G_t value of 0.05 stands for a more ductile concrete. Therefore, this parameter varies in the following *FEM* analyses.

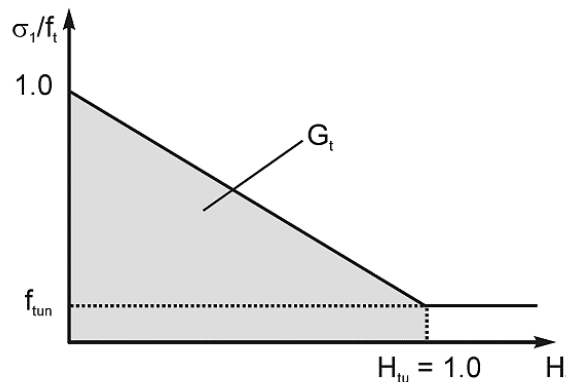


Fig. 3 Normalized stress – strain curve in tension (Schweiger et al., 2014)

2.3 Time dependent stiffness and strength

Time dependent parameters in the shotcrete model are the Young's modulus E , the ratio f_t/f_c and the ductility of shotcrete. The increase of E with time and the ratio f_t/f_c is described with the CEB-FIP model code (1990). To include the change of ductility of concrete, a plastic peak strain ϵ_{cp}^p at 1h, 8h and 24h is introduced. In the following research of grouted columns with imperfections in a soft soil layer, time dependency is not taken into account. (Schweiger et al., 2014)

3 General information about 2D and 3D models used

In order to get results for different imperfection types it is necessary to build a 2D and a 3D finite element model. All analyses in this thesis have been performed using the finite element code PLAXIS 2D and 3D.

3.1 2D-Model

Based on the work “Serviceability and safety in the design of rigid inclusions and combined pile-raft foundations” of Cécilia Bohn an axisymmetric model was generated. The dimensions of the symmetric model are 10 times 20 m. The geometry consists of a 5 m thick stiff soil layer at the bottom and a 15 m thick soft soil layer with the installed column above. The column without reinforcement has a length of 10 m and a diameter of 0.3 m. The mesh coarseness factors for the different soil materials are adapted in order to get a good mesh quality for more accurate results. Except for the area 2 m around the column a coarseness factor of 1.0 is used for the soft and the stiff soil layer. The area 2 m around the column has a coarseness factor of 0.5 and the column itself 0.125. This leads to smaller elements and a more accurate calculation. At the side of the column and under the column tip, an interface is defined with a R_{inter} factor of 0.67 for the adjacent soil. In case of no groundwater, the non-permeable material (column) is set to non-porous. In order to simulate a displacement pile, K_0 is set to 1.0 for the soft soil layer. The applied constitutive models are the Hardening Soil Model, linear elastic behaviour and the shotcrete model. Fig. 4 represents the axisymmetric model with its dimensions, the different mesh coarseness factors and the constitutive models that are used.

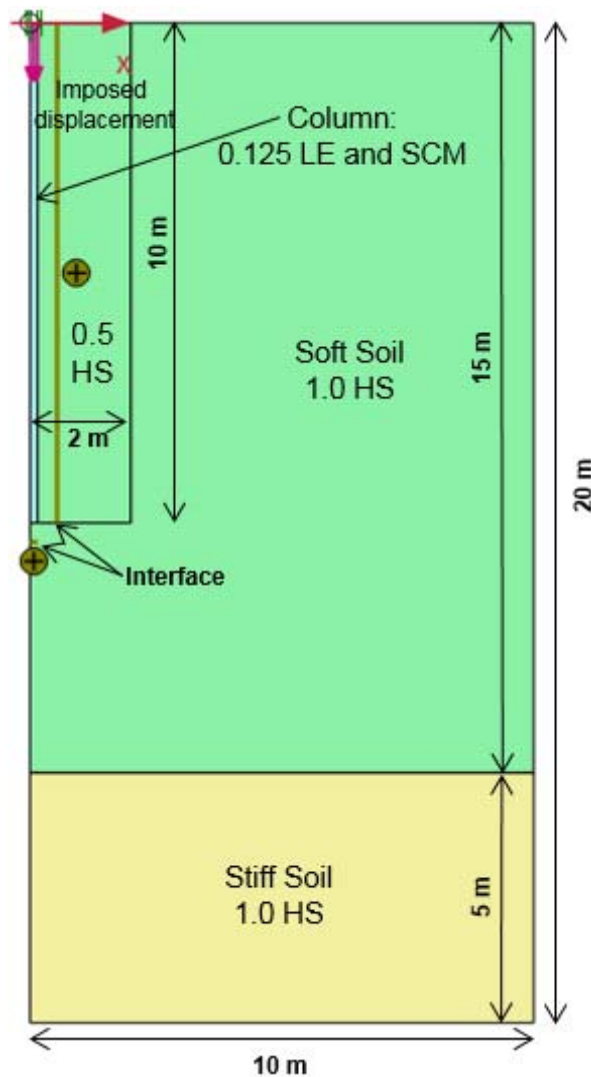


Fig. 4 Axisymmetric model

3.1.1 Calculation phases

Three different phases are introduced. The initial phase consists of the K_0 procedure. The second phase is the installation of the column and the activation of the interfaces. Displacements are reset to zero in this calculation step. The last step consists of the loading phase where an imposed displacement of 10 % of the diameter (0.03 m) of the column is introduced. The tolerated error is set to 0.005 for a more accurate calculation. The maximum load fraction per step, which controls the size of load step in staged construction, is set to 0.1 (default 0.5).

3.1.2 Soil parameters

Soil parameters have been taken from "Serviceability and safety in the design of rigid inclusions and combined pile-raft foundations". The following tables represent the input parameters for the different soil layers. (Bohn, 2015)

Tab. 2 Input parameters for soft soil layer

Parameter	Name	Value	Unit
material model	HS	[-]	[-]
oedometer modulus	$E_{\text{oed,soil}}^{\text{ref}}$	6.5	[MPa]
secant stiffness	E_{50}^{ref}	6.5	[MPa]
unloading/reloading stiffness	$E_{\text{ur}}^{\text{ref}}$	19.5	[MPa]
reference pressure	p_{ref}	100	[KPa]
power for stress-level dependency	m	0.7	[-]
friction angle	φ'	23	[°]
cohesion	c'	10	[KPa]
specific weight	γ	18	[KN/m ³]
earth pressure coefficient	K_0	1.0	[-]

Tab. 3 Input parameters for stiff soil layer

Parameter	Name	Value	Unit
material model	HS	[-]	[-]
oedometer modulus	$E_{\text{oed,soil}}^{\text{ref}}$	50	[MPa]
secant stiffness	E_{50}^{ref}	50	[MPa]
unloading/reloading stiffness	$E_{\text{ur}}^{\text{ref}}$	150	[MPa]
reference pressure	p_{ref}	100	[KPa]
power for stress-level dependency	m	0.5	[-]
friction angle	φ'	30	[°]
cohesion	c'	30	[KPa]
specific weight	γ	18	[KN/m ³]

Tab. 4 Input parameters for the column

Parameter	Name	Value	Unit
material model	LE	[-]	[-]

Young's modulus	E'	20	[GPa]
Poisson's ratio	ν	0.2	[-]
specific weight	γ	22	[KN/m ³]

The parameters for the shotcrete model are already described in chapter 2.1. The input parameters (Tab. 5) are chosen similar to the recommended parameters in "Shotcrete Model – Implementation, validation and application". (Schädlich & Schweiger, 2016) Time dependency is not taken into account and therefore E_1/E_{28} and $f_{c,1}/f_{c,28}$ is set to 1.0. The uniaxial failure strain ϵ_{cp}^p at 1 h, 8 h and 24 h is set to -0.0005. One of the most important input parameter is the tensile fracture energy of cured concrete $G_{t,28}$. This value varies in the following examples between 0.01 and 0.05.

Tab. 5 Input parameters for the shotcrete model

Name	Value	Unit
E_{28}	20	[GPa]
ν	0.2	[-]
$f_{c,28}$	10000	[KN/m ²]
$f_{t,28}$	1000	[KN/m ²]
ψ	0	[°]
E_1/E_{28}	1.0	[-]
$f_{c,1}/f_{c,28}$	1.0	[-]
$f_{c0,n}$	0.7	[-]
$f_{cf,n}$	0.75	[-]
$f_{cu,n}$	0.1	[-]
ϵ_{cp}^p at 1 h	-0.0005	[-]
ϵ_{cp}^p at 8 h	-0.0005	[-]
ϵ_{cp}^p at 24 h	-0.0005	[-]
$G_{c,28}$	50	[KN/m]
$f_{tu,n}$	0	[-]
$G_{t,28}$	0.01/0.05	[KN/m]

L_{eq}	0	[m]
a	18	[-]
φ^{max}	37	[°]
γ_{fc}	1.0	[-]
γ_{ft}	1.0	[-]
t_{hydr}	28	[day]

3.2 3D-Model

For piles with inclination, curvature and load eccentricity a 3D model has to be applied. Therefore the axisymmetric model is extended to a 3D model. The dimension of the models are 20 m x 20 m x 20 m with a 5 m thick stiff soil layer at the bottom and 15 m thick soft soil layer above. The pile is 10 m long and has a diameter of 0.3 m. Again, around the column and along the tip of the column an interface is defined. R_{inter} for the adjacent soil is set to 0.67. K_0 is equal to 1.0 in the soft soil layer to simulate a displacement pile. Groundwater is not taken into account and therefore the material for the column is set to non-porous. The *FEM* analysis is done with the Hardening Soil Model, Mohr Coulomb model and the shotcrete model. A surface load of 5600 KN/m², which corresponds to a settlement of 30 mm for a column without imperfection, is applied. Mesh refinements around the column are made to ensure accurate results. Fig. 5 represents the 3D model with its dimensions, different soil layers and the applied load on the column.

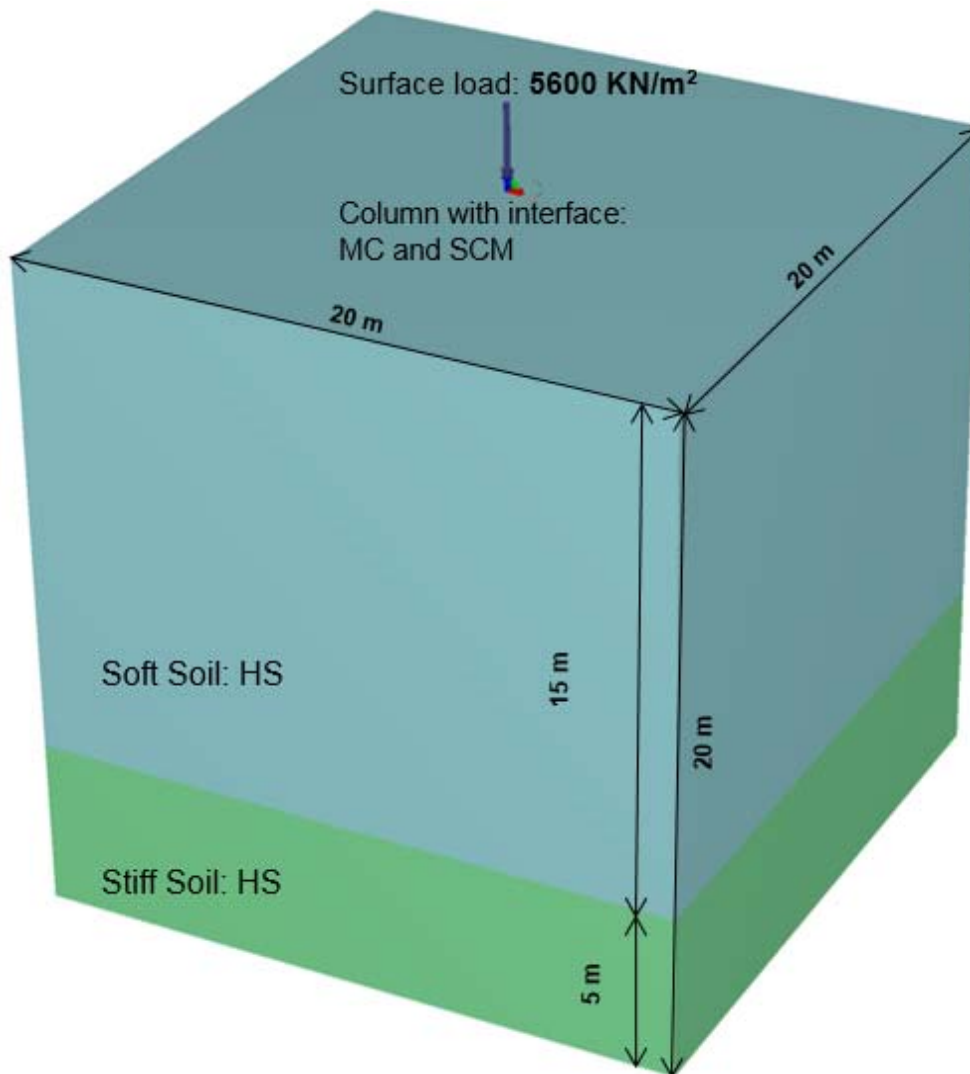


Fig. 5 3D model

3.2.1 Calculation phases and input parameters

The calculation phases and the input parameters for both soil layers, except for the column, are the same as for the axisymmetric model (see Tab. 2 and 3). For all 3D FEM analyses, the Mohr Coulomb model is applied for the column. Tab. 6 represent the input parameters for the column. The parameters for the shotcrete model are the same as in Tab. 5.

Tab. 6 Mohr Coulomb input parameters for the column

Parameter	Name	value	unit
Young's modulus	E'	20	[GPa]
Poisson's ratio	ν'	0.2	[-]
friction angle	ϕ'	37	[°]
cohesion	c'	2500	[KPa]
unit weight	γ	22	[KN/m ³]

4 Necking and Bulging

Necking and bulging is an imperfection type where the diameter of the column is increased or decreased in a certain area of the column. For the *FEM* analysis the diameter is decreased or increased by 0.05 m. Therefore, the interface around the column is redefined along the necking and bulging area (Bohn, 2015).

Fig. 6 represents in detail the geometry for necking and bulging in three different depths. The detail of necking and bulging with the interface following the shape of the column is shown in Fig. 7.

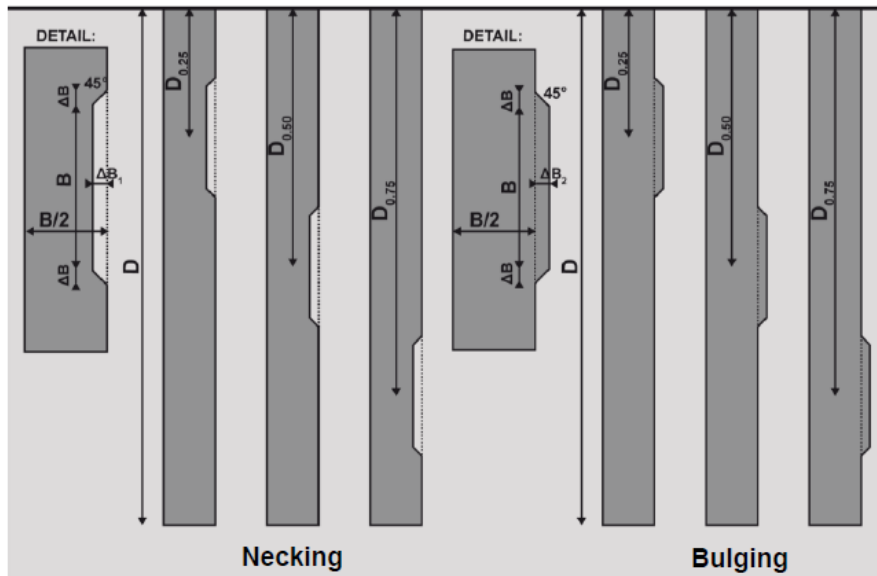


Fig. 6 Necking and bulging imperfections (Bohn, 2015)

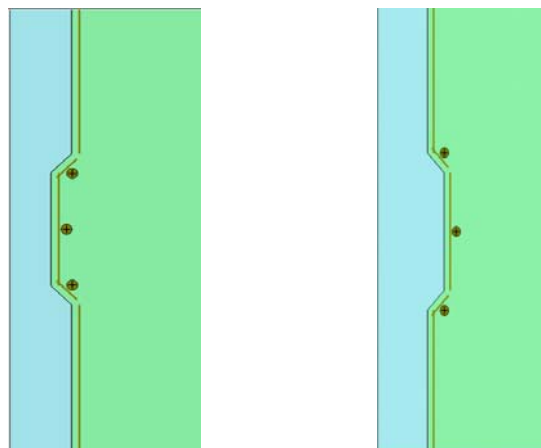


Fig. 7 Necking and bulging with the interface following the shape of the column

4.1 Necking

The calculation for necking is performed for three different depths assuming a linear elastic behavior for the column and subsequently with the shotcrete model.

4.1.1 Load-settlement curves

Fig. 8 shows the load-settlement curves for all necking positions compared to a column without imperfection. There is a slight increase of the bearing capacity for all necking positions due to higher skin friction in the necking area.

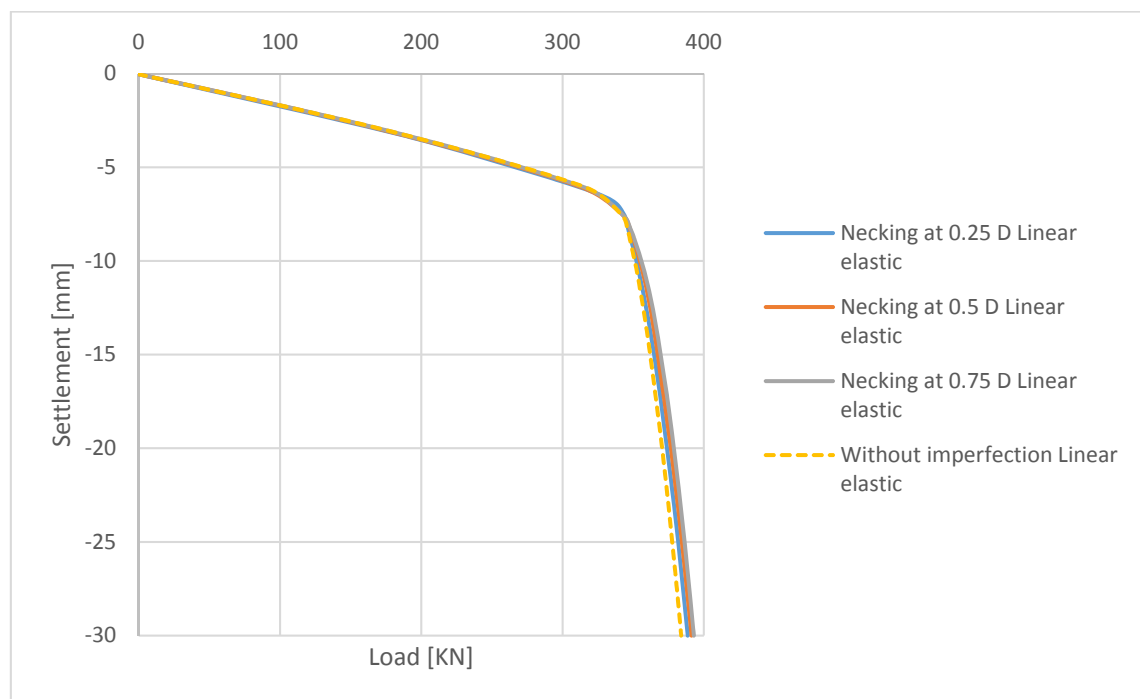


Fig. 8 Load-settlement curves with necking for $B = 0.3$ m (linear elastic)

Fig. 9 shows the results of the calculation with the shotcrete model and similar results are obtained for all necking positions except of necking at $0.25 D$. Necking at $0.25 D$ shows a slight decrease of bearing capacity due to the appearance of some cracks (see Fig. 14).

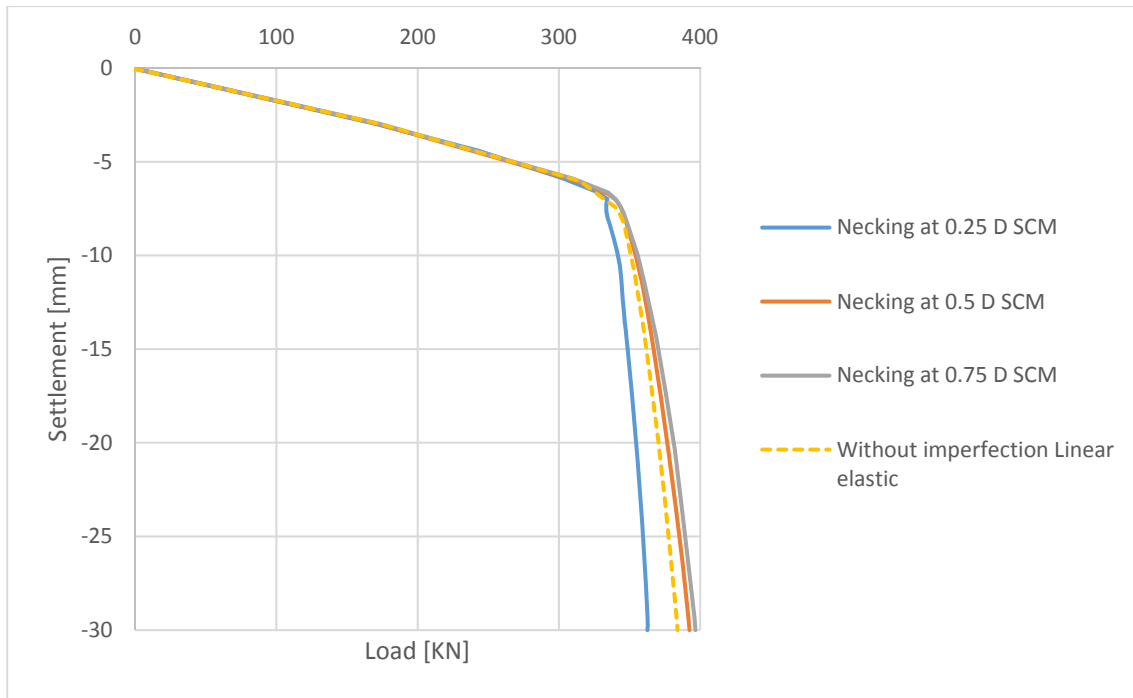


Fig. 9 Load-settlement curves with necking for $B = 0.3$ m (shotcrete model)

4.1.2 Vertical stresses and principal effective stresses σ'_3

Fig. 10 illustrates the vertical stresses for necking at $0.25 D$. All analyses show a similar stress distribution, but some differences in the area where the diameter is decreased can be noticed. One can see stress concentrations at the corners of the necking zone for a linear elastic behavior. They are in a range of ~ 20 MPa and therefore the compressive strength of the concrete is exceeded. In case of the shotcrete model these stress concentrations have moved to the left, inside the necking area. For all other necking positions the vertical stresses in the column are almost the same.

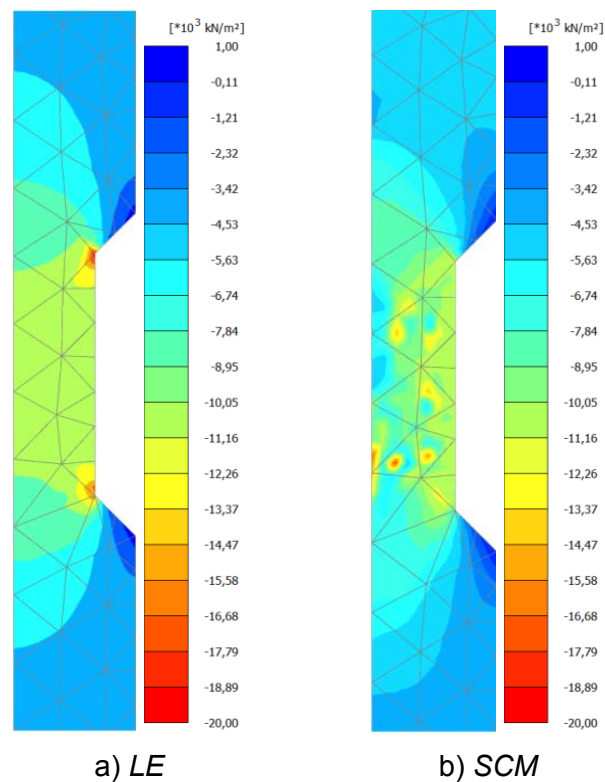


Fig. 10 Vertical stresses for necking at $0.25 D$ (*LE* and *SCM*)

Fig. 11 represents the principal effective stresses σ'_3 . Different results are obtained from the calculation with a linear elastic behavior and the shotcrete model. Considering only tensile stresses one can see that the area of high tensile stresses at the corner where the decrease of the diameter starts is significantly larger for shotcrete model than for a linear elastic behavior of the column. Furthermore, Fig. 11 b) represents tensile stresses directly in the necking zone. These stresses indicate that the column has cracked. For a linear elastic calculation these tensile stresses do not develop. A similar effect can be observed in Fig. 12 for necking at $0.5 D$. For necking at $0.75 D$ both constitutive models give almost the same tensile stresses σ'_3 . The column does not crack any more for the position of the necking zone at 0.75 percent of D .

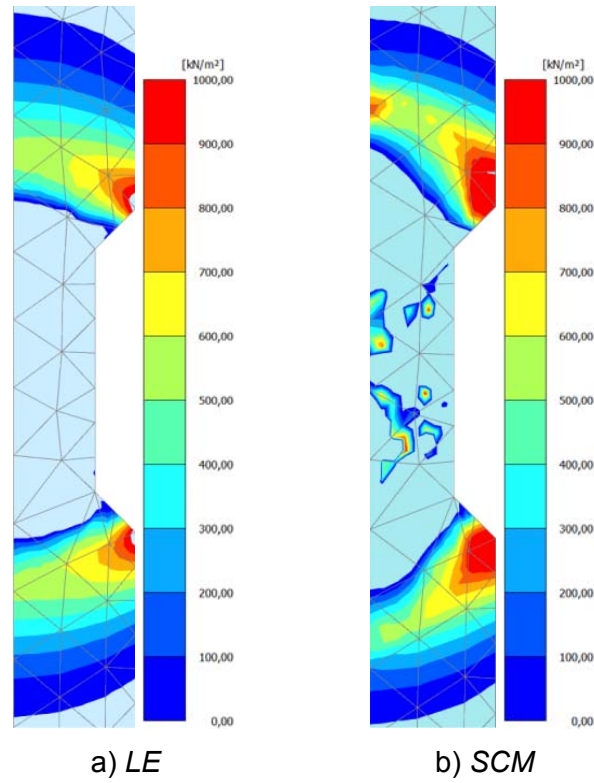


Fig. 11 Principal effective stresses σ'_3 (tensile stresses) for necking at $0.25 D$ (*LE* and *SCM*)

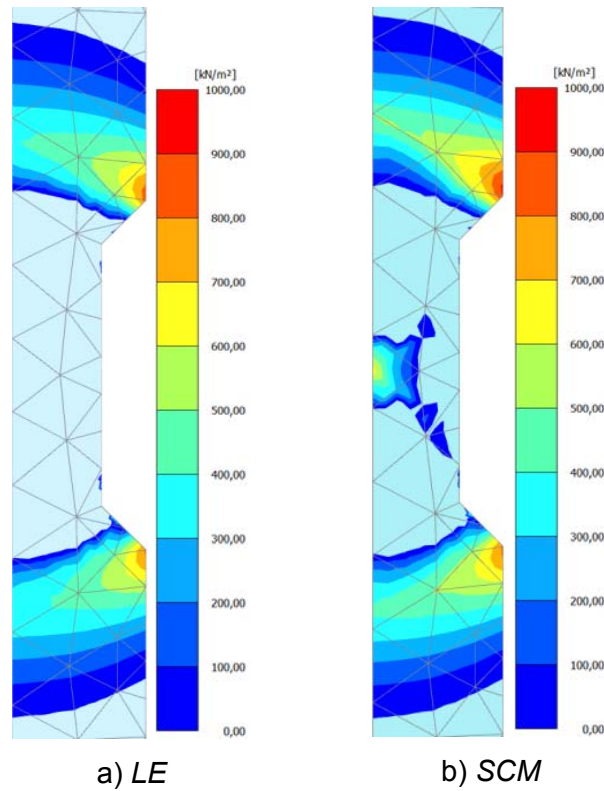


Fig. 12 Principal effective stresses σ'_3 (tensile stresses) for necking at $0.5 D$ (*LE* and *SCM*)

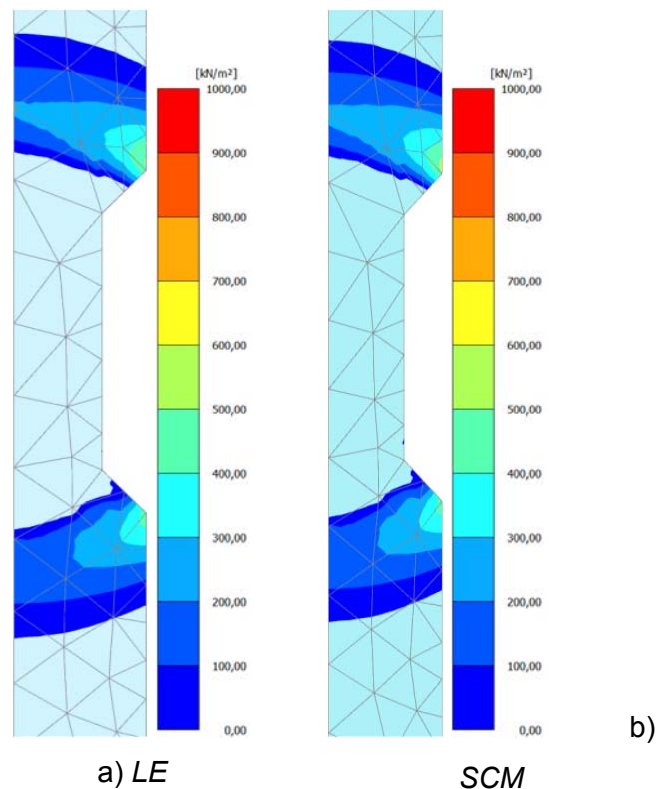


Fig. 13 Principal effective stresses σ'_3 (tensile stresses) for necking at $0.75 D$ (*LE* and *SCM*)

4.1.3 Crack pattern for columns with necking

A special parameter of the shotcrete model is the normalized tension softening parameter H_t (normalized tension softening parameter: 0: no softening; 0-1: softening; > 1: residual), which represents the crack pattern of concrete in the contour plots. Such a crack pattern is presented in Fig. 14 for necking at $0.25 D$. For areas with high tensile stresses one can see that cracks develop, especially in the necking area.

For necking at $0.5 D$ the crack pattern is slightly different compared to the crack pattern for necking at $0.25 D$. Due to the fact that the necking position is in a greater depth less cracks develop in concrete. For necking in a depth of $0.75 D$ no cracks develop.

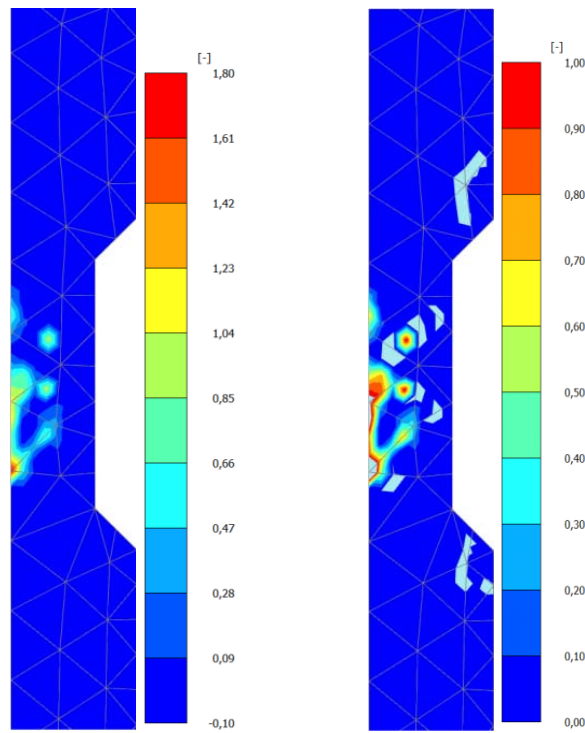


Fig. 14 Crack pattern - $G_{t,28} = 0.01$ for necking at $0.25 D$

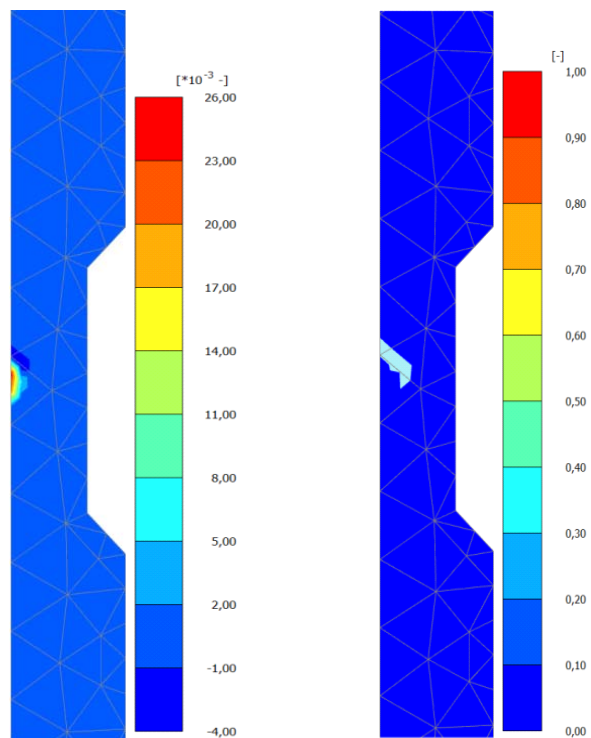


Fig. 15 Crack pattern - $G_{t,28} = 0.01$ for necking at $0.5 D$

4.2 Bulging

The calculation for bulging is performed in three different depths ($0.25 D$, $0.5 D$, and $0.75 D$) again with a linear elastic behavior of the column and subsequently with the shotcrete model.

4.2.1 Load-settlement curves

For a linear elastic analysis (Fig. 16) and a calculation with the shotcrete model (Fig. 17), no significant variation of the load-settlement curves can be recognized. As in the case of necking a slight increase of bearing capacity can be observed. The difference is that the increase of bearing capacity compared to necking is larger since a supporting force from the surrounding soil is acting against the bulging area. It can be also observed that the bearing capacity increases slightly with the depth of bulging.

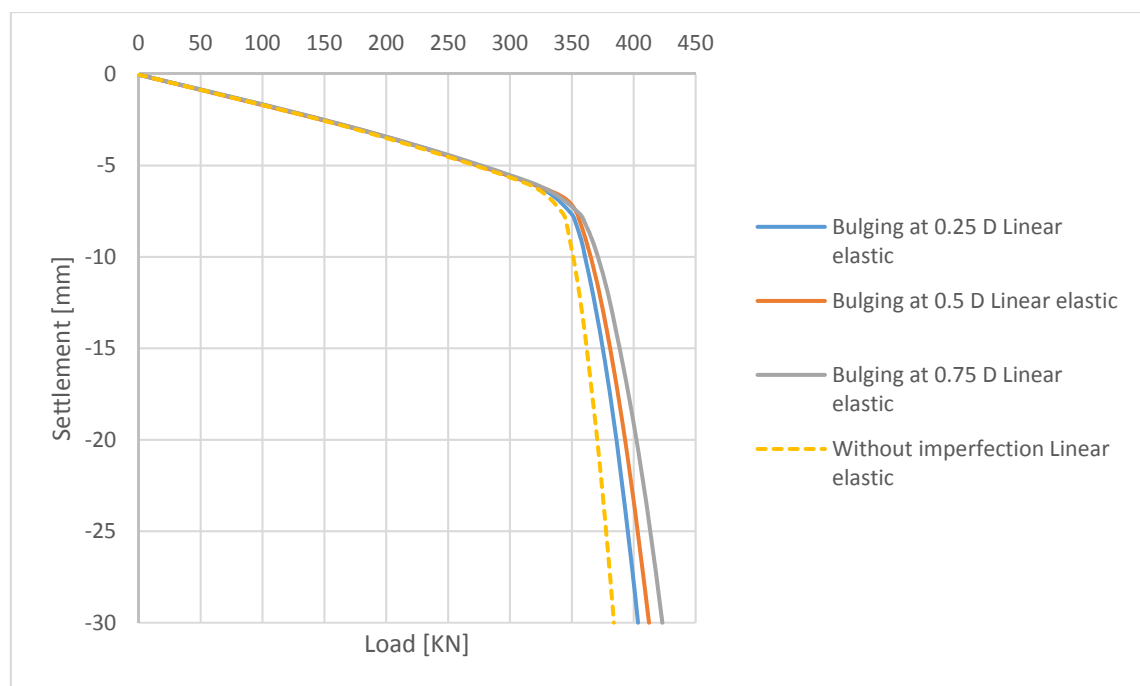


Fig. 16 Load-settlement curves with bulging for $B = 0.3$ m (LE)

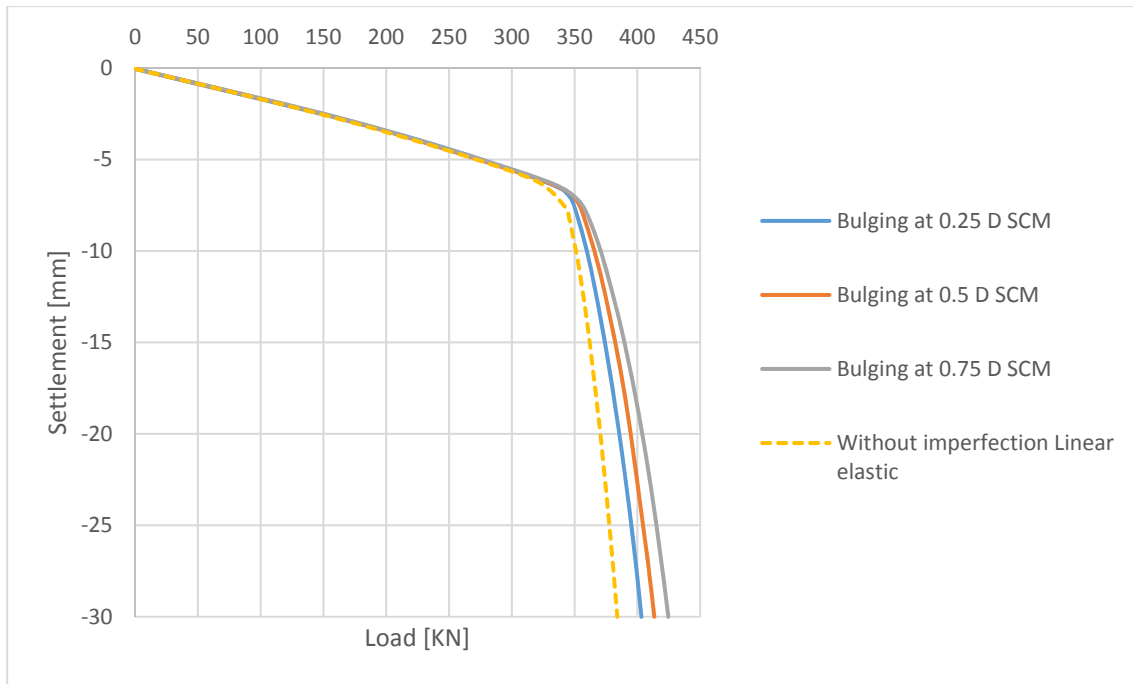


Fig. 17 Load-settlement curves with bulging for $B = 0.3$ m (SCM)

4.2.2 Vertical stresses and principal effective stresses σ'_3

As expected, the vertical stresses and the effective principal stresses σ'_3 do not change significantly. This is visible in Fig. 18 and Fig. 19 for bulging at $0.25 D$. The vertical stress distribution in the bulging area of the column consists only of compression stresses. The principal effective stresses σ'_3 do not exceed the allowed tensile stress of 1000 KN/m^2 , the maximum calculated being 800 KN/m^2 . For bulging in all other depths no differences can be noticed concerning the vertical stresses and the principle effective stresses σ'_3 .

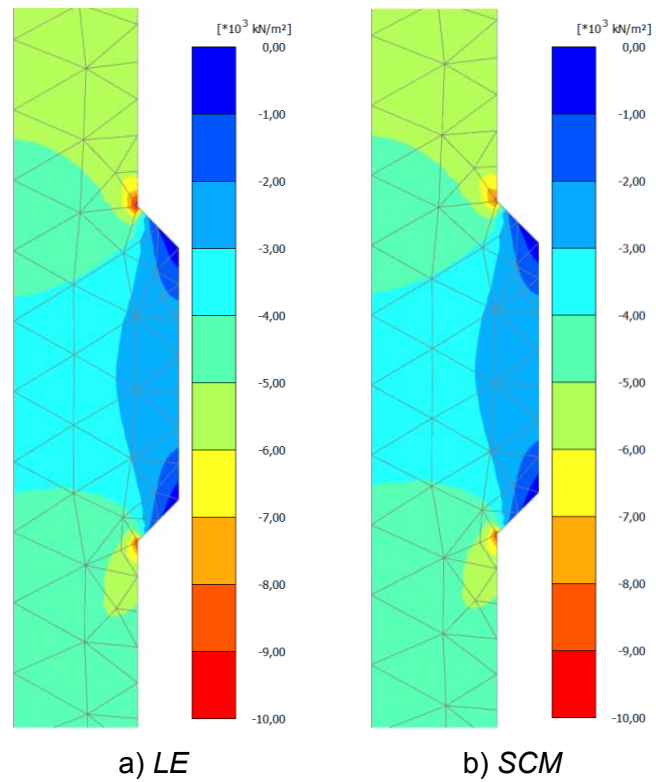


Fig. 18 Vertical stresses for bulging at 0.25 *D* (*LE* and *SCM*)

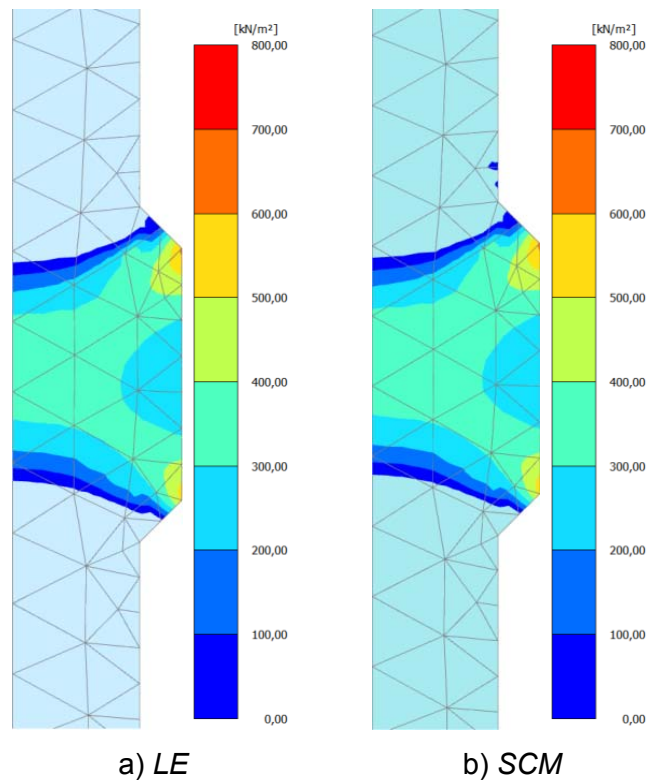


Fig. 19 Principal effective stresses σ'_3 (tensile stresses) for bulging at 0.25 *D* (*LE* and *SCM*)

5 Inclination

An inclined column is another imperfection type, which could appear while installing a column in a soft soil. Six different inclinations, which can be seen in Fig. 20 are investigated.

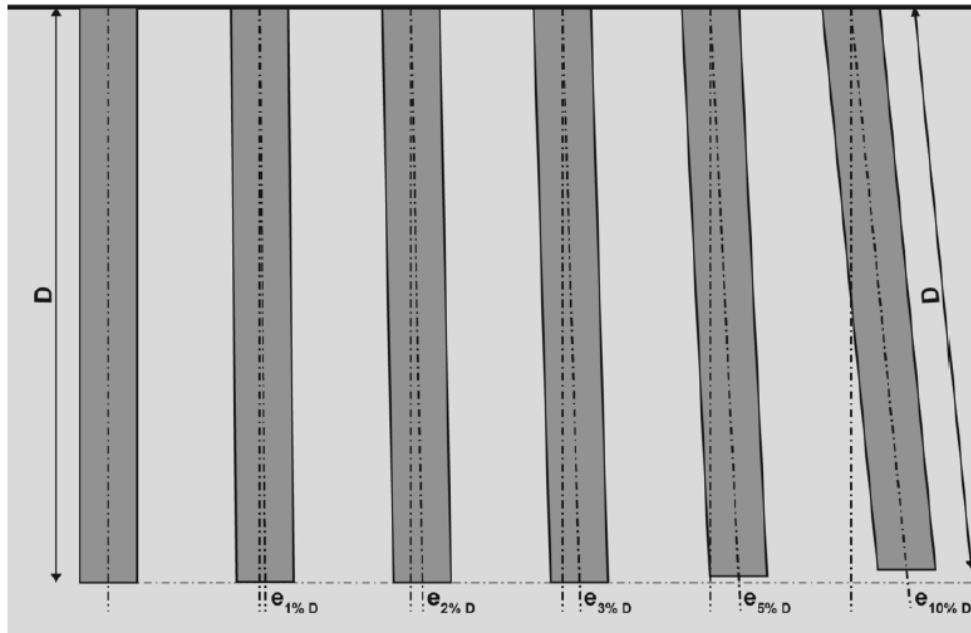


Fig. 20 Inclination levels from 1 % up to 10 % of D (Bohn, 2015)

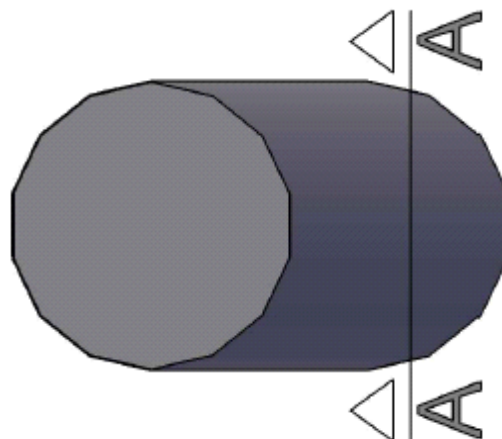


Fig. 21 Top view of an inclined column with cross section A - A

5.1 Load-settlement curves

The load-settlement curves obtained by applying the Mohr Coulomb model (Fig. 22) and the shotcrete model (Fig. 23) have to be compared. It is noticeable that there is a decrease of bearing capacity for an inclined column with $e = 10\% D$ (Fig. 22). This is an indication that the entire column had cracked. Due to a so-called passive soil support on the left side of the column, all other inclinations show a small increase of bearing capacity. (Bohn, 2015)

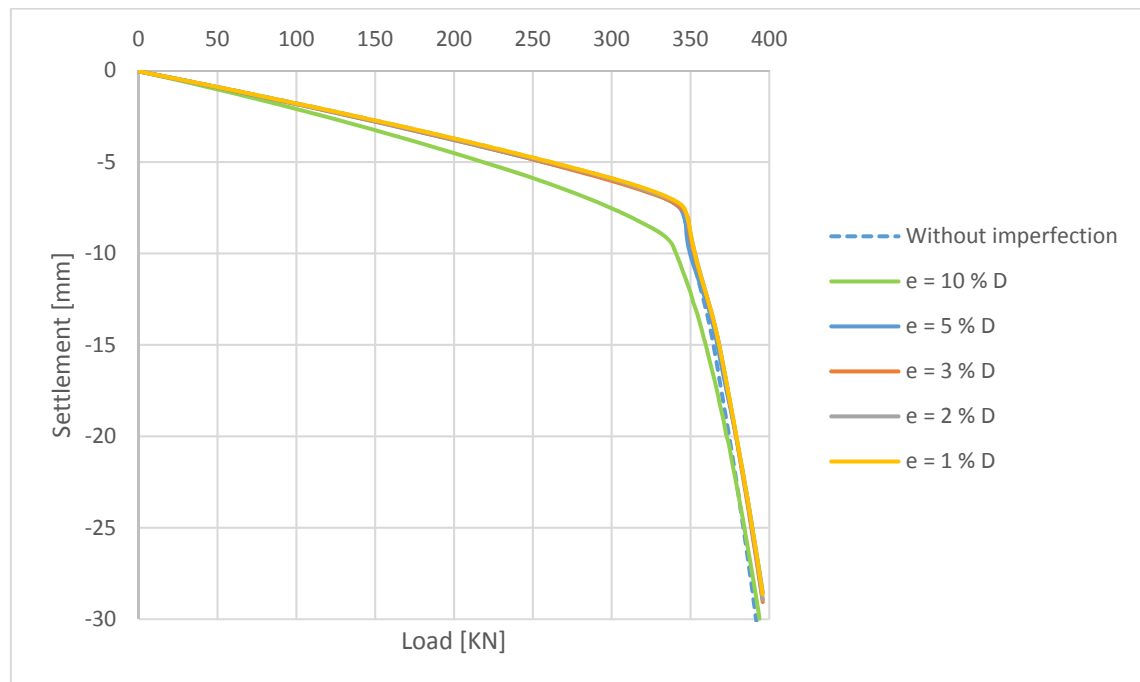


Fig. 22 Load-settlement curves with column inclination for $B = 0.3$ m (MC)

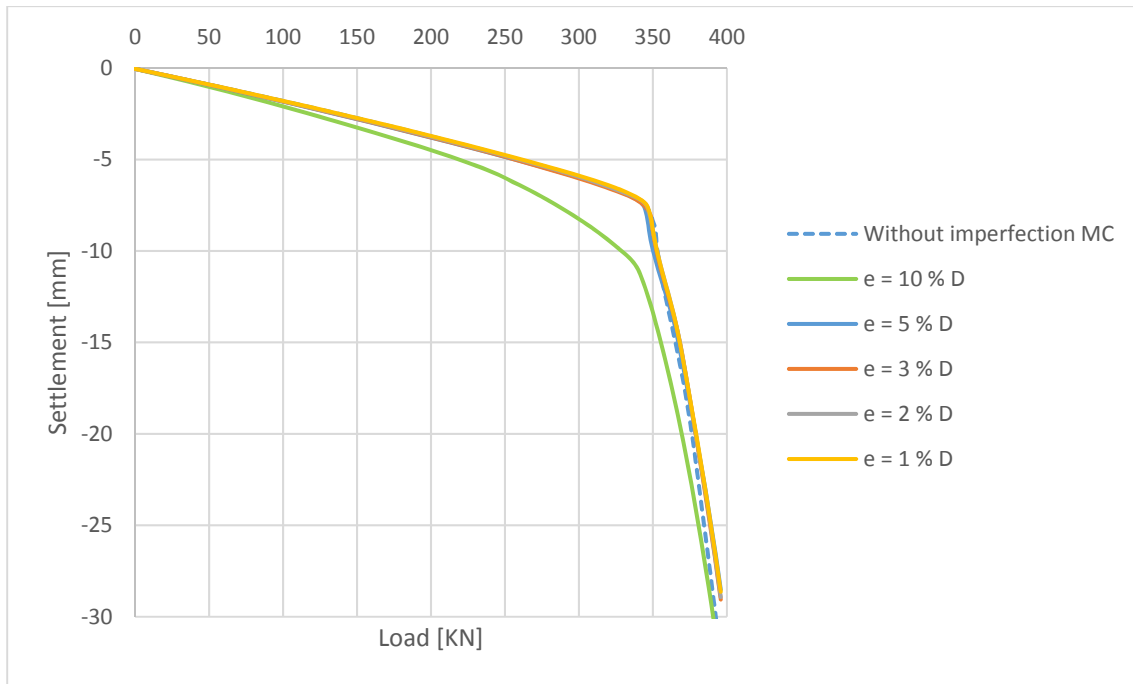


Fig. 23 Load-settlement curves with column inclination for $B = 0.3$ m (SCM)

In case of an inclined column with $e = 10\% D$ the calculation with the shotcrete model gives a slightly lower bearing capacity compared to Mohr Coulomb. This is the result of high tensile stresses on the right hand side of the column which causes cracks in the concrete.

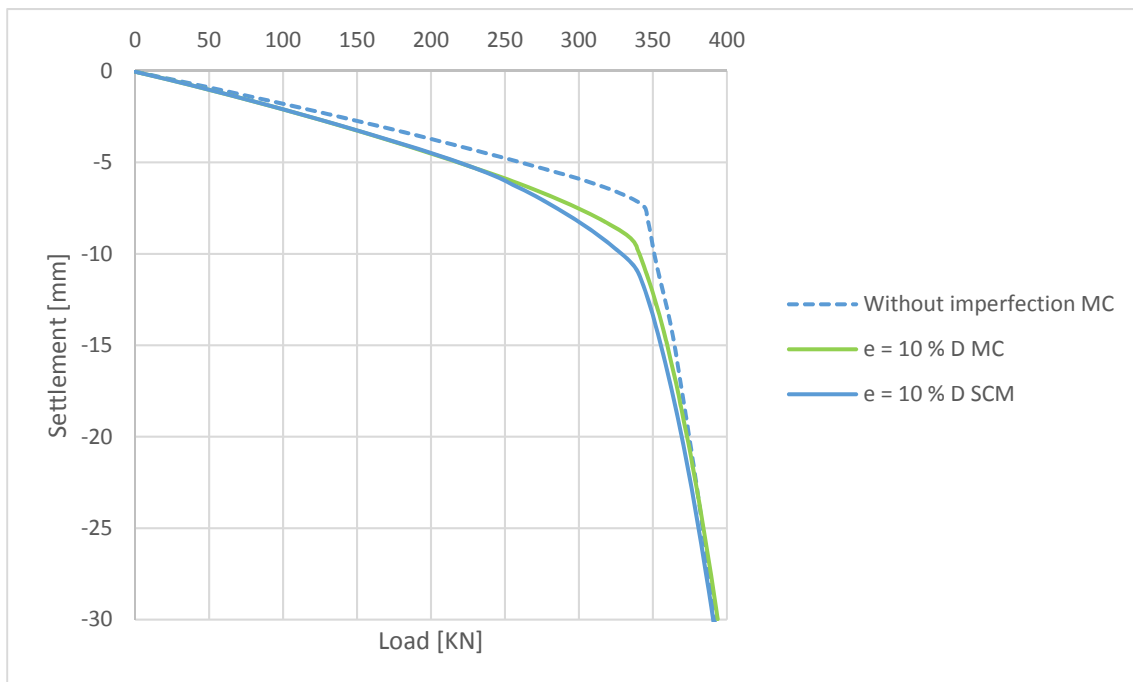


Fig. 24 Load-settlement curves with inclination for $B = 0.3$ m (MC and SCM)

5.2 Vertical stresses and principal effective stresses σ'_3

Generally, high compressive stresses or tensile stresses appear in the column. Comparing the vertical stresses (Fig. 25) obtained from the Mohr Coulomb model with those from the shotcrete model shows that for Mohr Coulomb a larger area in compression arises. On the contrary, the tension area is much smaller for Mohr Coulomb. The remaining plots of the vertical stresses in the column can be found in Appendix A. Only for an inclination of $e = 5 \% D$ a small area of tension develops on the right side of the column. For all other inclination no significant big differences can be observed between Mohr Coulomb and the shotcrete model. A look at the principal effective stresses σ'_3 from the shotcrete model shows tensile stresses higher than 1000 KN/m^2 although the uniaxial tensile strength $f_{t,28}$ has been set to 1000 KN/m^2 . This problem arises through to interpolation for plotting contours. The yellow area in Fig. 26 b) shows the stress points higher than $f_{t,28}$. However, a control of each stress point in Excel gives results just below 1000 KN/m^2 for all stress points.

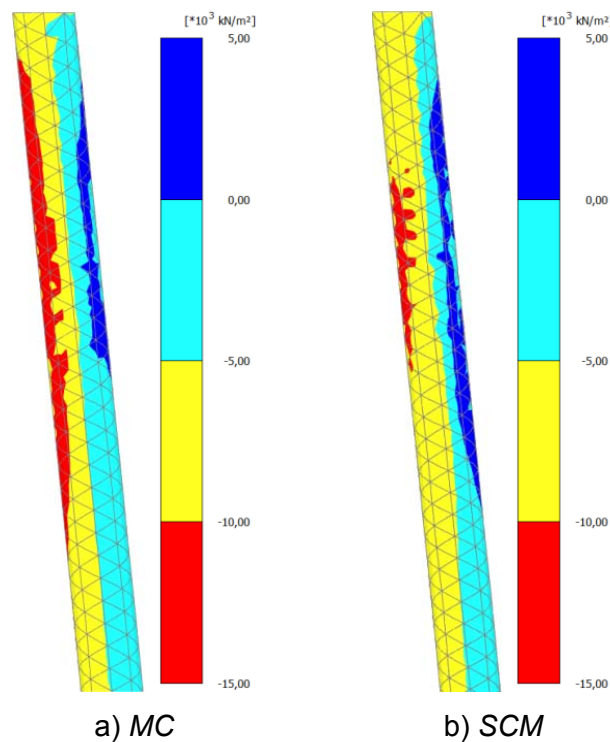


Fig. 25 Vertical stresses in the column for $e = 10 \% D$ (MC and SCM)

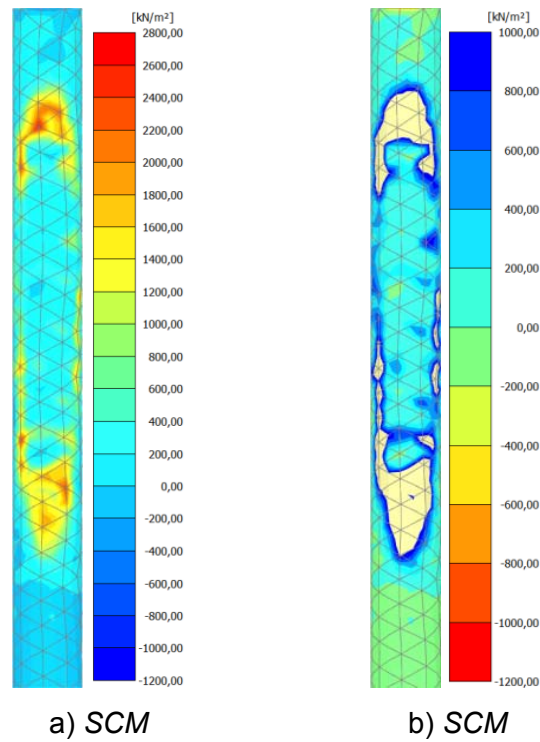


Fig. 26 A – A: stress points with interpolation error for $e = 10 \% D$ (MC and SCM)

Fig. 27 displays only tensile stresses from principal effective stresses σ'_3 . Thus, the yellow area is in compression. Significant differences in these contour plots are clearly visible. For Mohr Coulomb tensile stresses are limited but not reduced to a residual value like in the shotcrete model (Schweiger, Sedighi, Henke, & Borchert, 2014). All other plotted principal effective stresses σ'_3 are shown in Appendix A. For reduced inclination the plots of σ'_3 look very similar for all calculations.

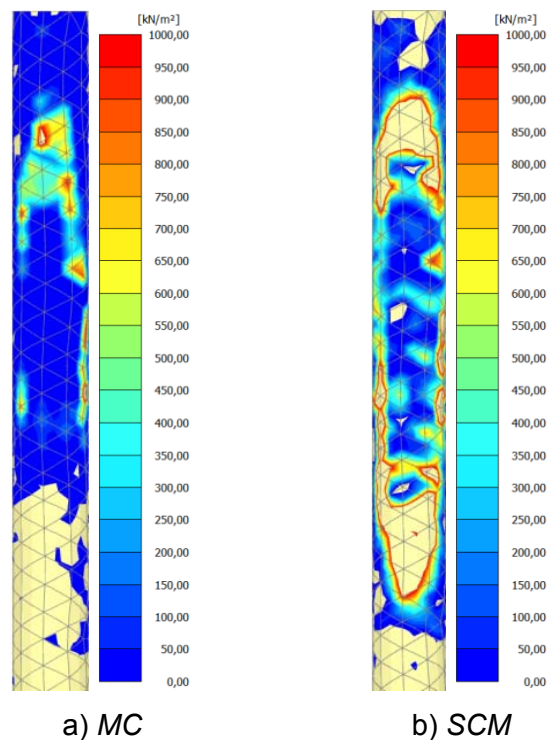


Fig. 27 A – A: principal effective stresses σ'_3 (tensile stresses) for MC and SCM

5.3 Crack pattern for columns with inclination $e = 10 \% D$

The following figures show the state variable H_t (normalized tension softening parameter: 0: no softening; 0-1: softening; > 1: residual) which is an internal variable of the shotcrete model to monitor the crack pattern. (Schädlich & Schweiger, 2016) Varying the $G_{t,28}$ parameter gives different results for the crack pattern since $G_{t,28}$ defines whether the concrete is rather brittle or ductile. The crack pattern, which is the consequence of a loaded inclined column with 10 % D , is represented in Fig. 28. The entire yellow surface indicates the cracked zone of the column for $G_{t,28} = 0.01$. Compared to that, Fig. 29 shows the crack pattern for a more ductile concrete ($G_{t,28} = 0.05$) where the cracked area is much smaller.

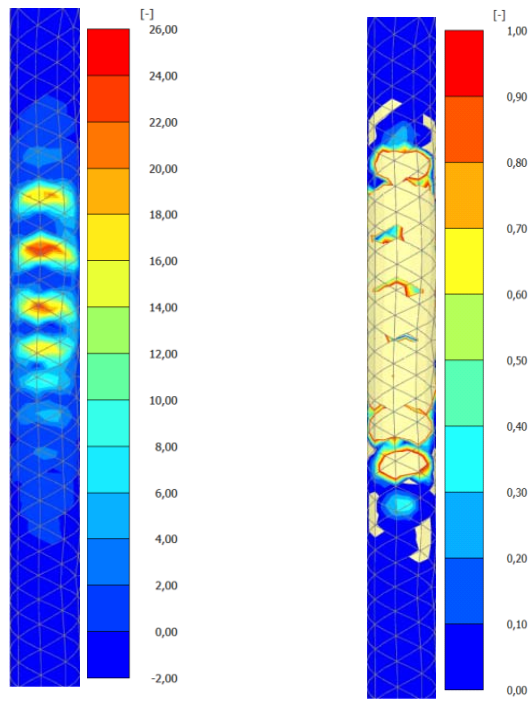


Fig. 28 A – A: Crack pattern - $G_{t,28} = 0.01$

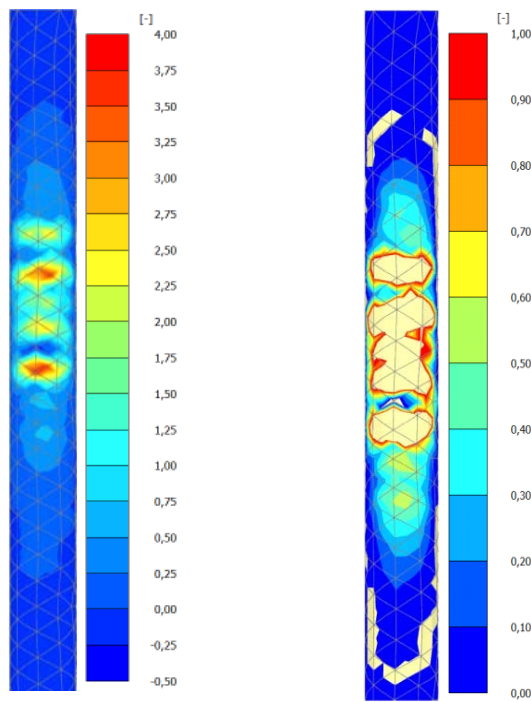


Fig. 29 A – A: Crack pattern - $G_{t,28} = 0.05$

5.4 Normal force and bending moment

Through the “Structural forces in volumes” option the structural forces in the column are worked out. Since the load in the column for Mohr Coulomb model and the shotcrete model does not change, no significant differences appear in the development of the normal force over the length of the column. The bending moment reaches the largest value in a depth of about 1.15 m. Mohr Coulomb yields higher bending moments compared to the shotcrete model. In Appendix A structural forces for all other inclinations are displayed. The bending moment obtained from the shotcrete model gets closer to the bending moment of Mohr Coulomb when the inclination is decreasing.

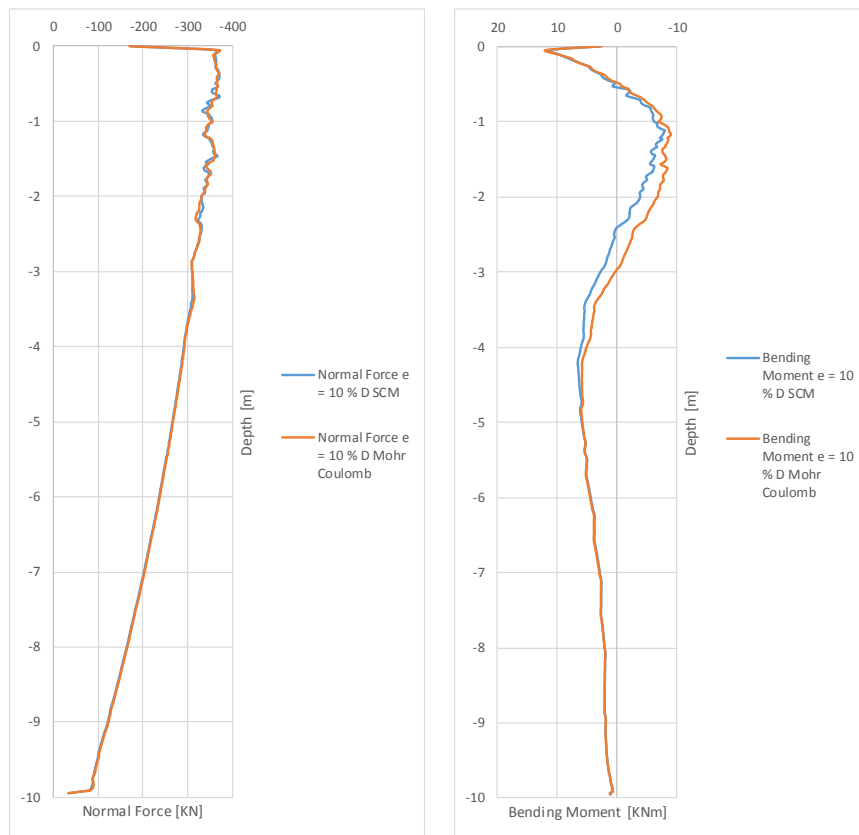


Fig. 30 Structural forces for a column with $e = 10\% D$ (MC and SCM)

Varying the parameter $G_{t,28}$ does not result in large differences in the shape of the normal force and the bending moment according to Fig. 31.

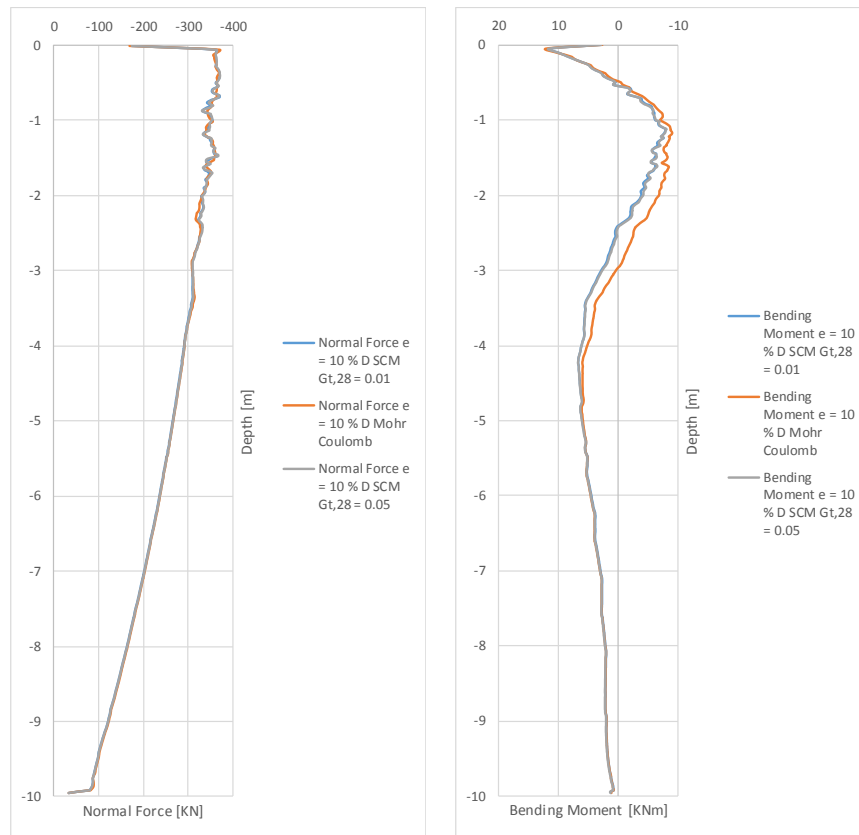


Fig. 31 Structural forces for a column with $e = 10 \% D$ for different $G_{t,28}$ values (*MC* and *SCM*)

5.5 Activation of the “updated mesh” option

The “updated mesh” option is a tool in PLAXIS 3D which includes “second order effects” due to large deformations. In case of an inclined column with $e = 10 \% D$ deformations are relatively high and hence this option has an influence on the bearing capacity of the column. For all other inclinations, this option has no impact on the bearing capacity. In comparison to a calculation without “updated mesh” option, the bearing capacity is reduced by approximately 15 % (see Fig. 32). The calculation stops after a loading of $\sim 4100 \text{ KN/m}^2$ instead of 5600 KN/m^2 .

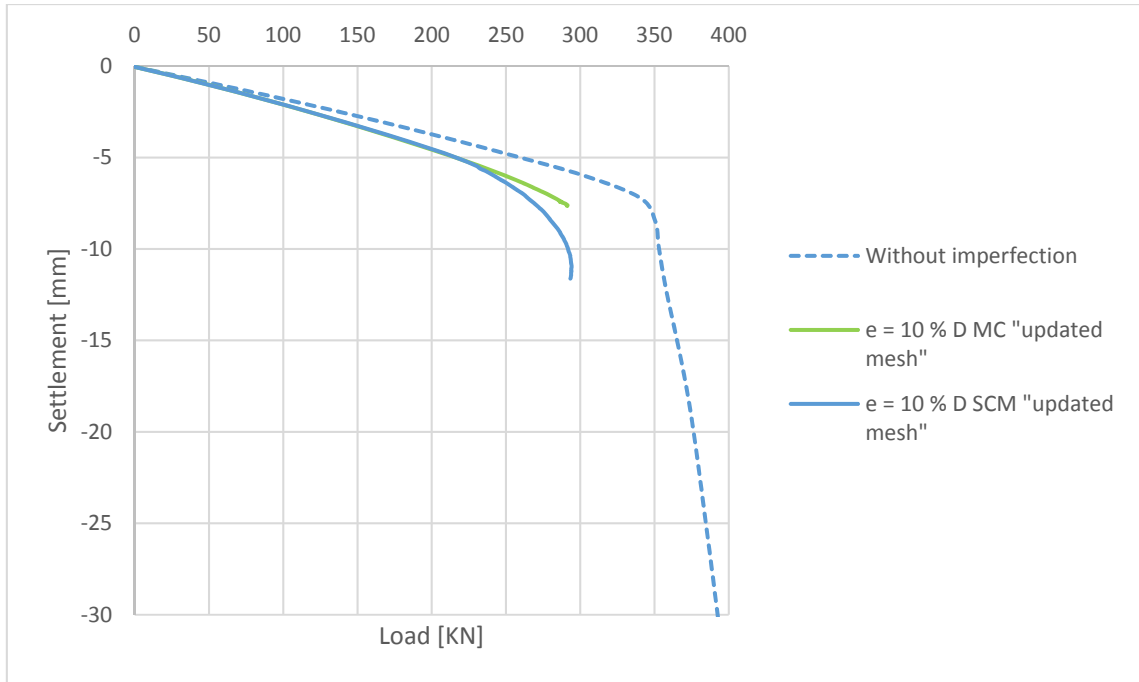


Fig. 32 Load-settlement curves with activation of the „updated mesh“ option (MC and SCM)
 The crack pattern changes slightly as presented in Fig. 33. The cracked yellow area becomes smaller considering the updated mesh option. The red area in Fig. 33 a) has not been cracked yet but is instantly before.

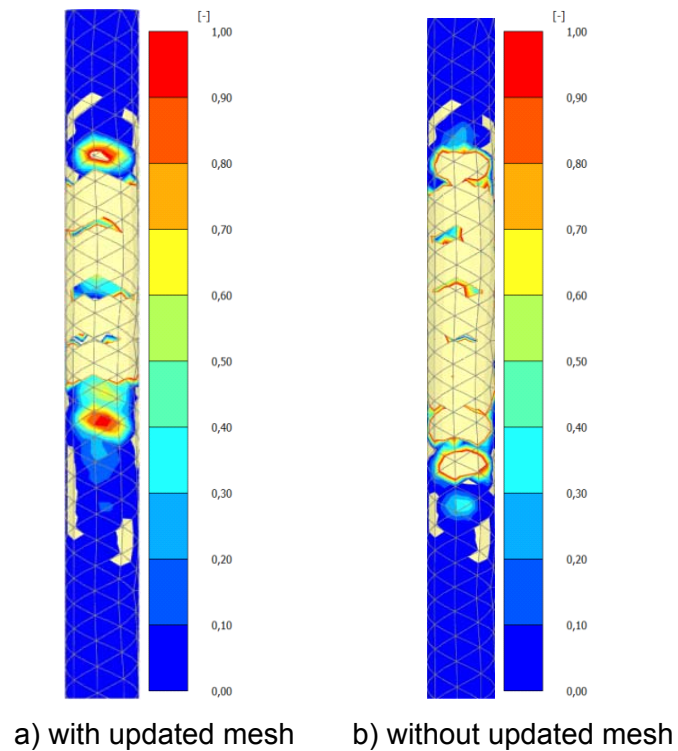


Fig. 33 A – A: Crack pattern - $G_{t,28} = 0.01$

6 Load eccentricity

Load eccentricity may lead to tension in the column, investigated are load eccentricities of $B/8$ and $B/7$. Fig. 34 represents a scheme how the column with a diameter of 0.3 m is loaded to achieve different eccentricities of $B/8$ and $B/7$. Due to a linear increasing trapezoidal load, the resultant force moves to the right of the column.

The 3D model in PLAXIS as well as the parameters for all soil layers, the column and the calculation phases remain the same as for inclined columns. Only the surface load changes from a uniform load to a trapezoidal load.

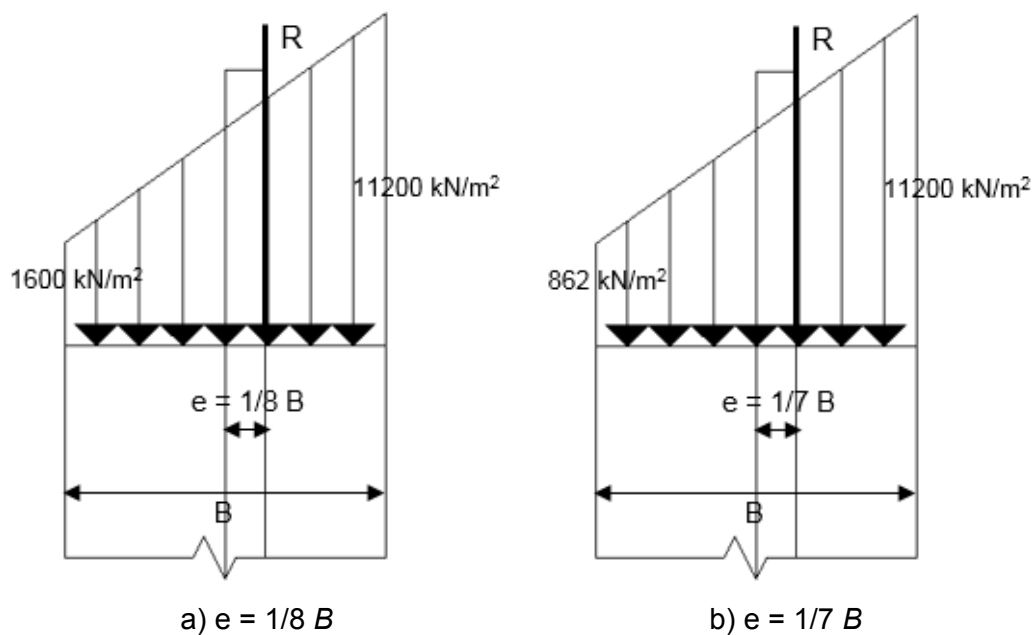


Fig. 34 Load eccentricity for $e = 1/8 B$ and $e = 1/7 B$

6.1 Load-settlement curves

Load eccentricities of $B/8$ and $B/7$ have no noticeable influence on the load-settlement curves for both constitutive models as shown in Fig. 35. There is no change of geometry of the column itself and therefore skin friction and tip resistance behave in the same way as for a normally loaded column without imperfection.

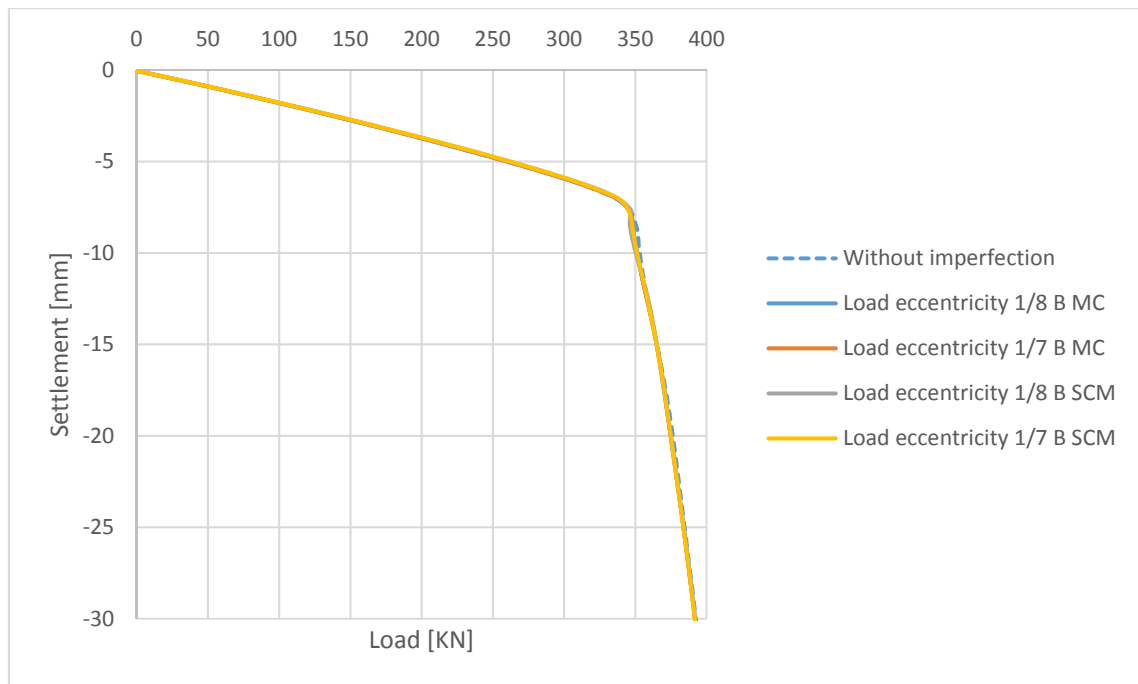


Fig. 35 Load-settlement curves for load eccentricity (MC and SCM)

6.2 Vertical stresses

The vertical stresses are different in case of Mohr Coulomb and the shotcrete model. For a load eccentricity of $B/8$ no tension (Fig. 36) appears at the edge of the column. The only difference which can be seen in the following figure is the area where the compressive strength is exceeded. The area in compression is much larger for the Mohr Coulomb model than for the shotcrete model.

For load eccentricity higher than $B/8$ tensile stresses develop on the left side of the column when performing a calculation with the shotcrete model. In Fig. 37 the vertical stresses and the development of tensile stresses on the left side of the column are shown. High compressive stresses appear for both applied constitutive models.

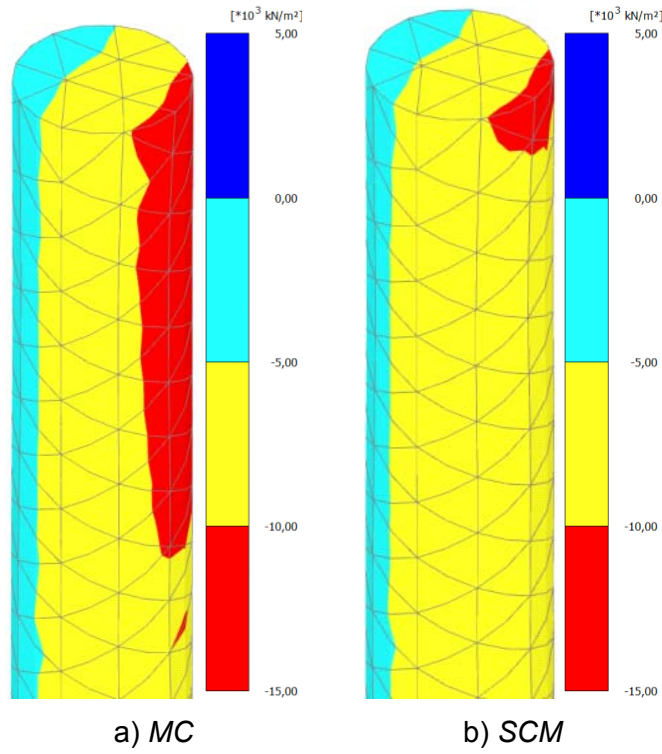


Fig. 36 Vertical stresses for load eccentricity $B/8$ (MC and SCM)

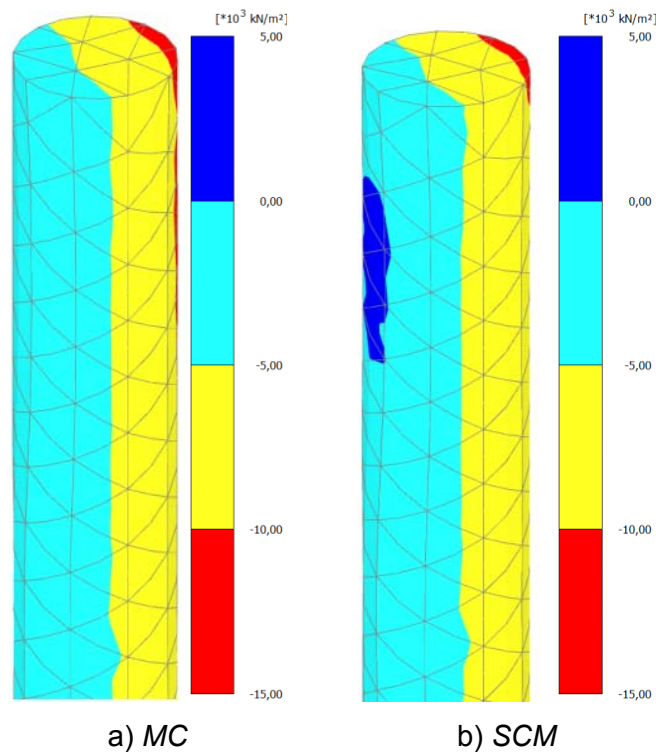


Fig. 37 Tensile stresses for load eccentricity $B/7$ (MC and SCM)

6.3 Normal force and bending moment

The structural forces, which are calculated in PLAXIS 3D with the structural force option, of a column with a diameter of 0.3 m with different load eccentricities are presented in Fig. 38. No significant differences in the shape of the normal force and the bending moment for Mohr Coulomb and the shotcrete model are apparent.

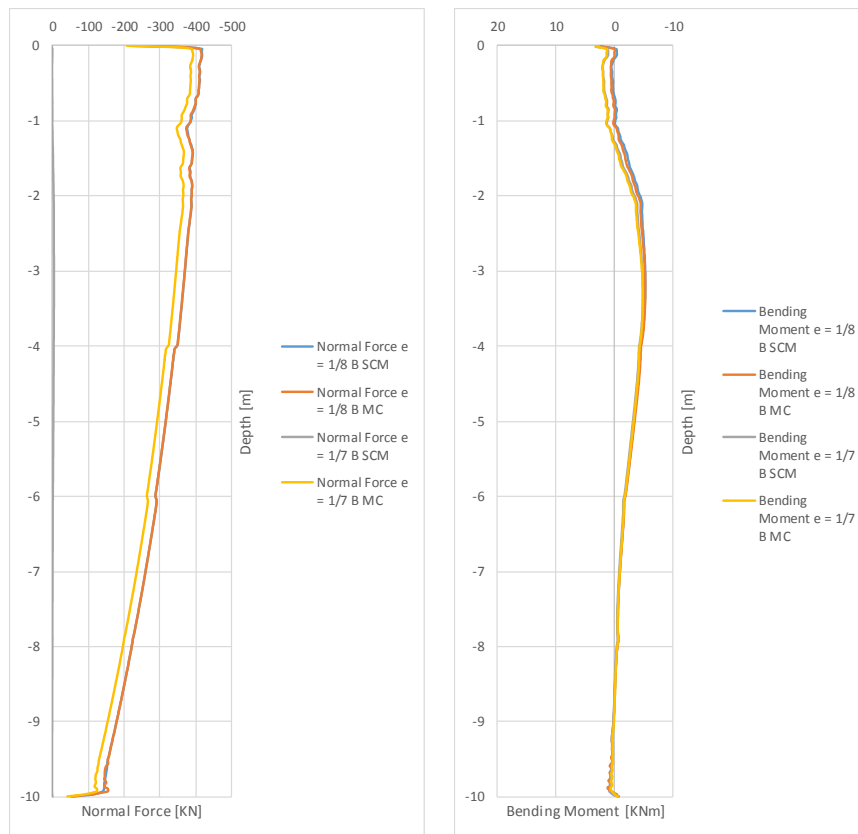


Fig. 38 Structural forces for a column with load eccentricity for $e = 1/8$ & $1/7 B$ (MC and SCM)

7 Curvature

Columns with a diameter of 0.3 m and different curvatures with $r = 200$ m, $r = 100$ m and $r = 50$ m were investigated in *3D FEM* analysis. For columns with curvature buckling problems may occur. The basic model in *PLAXIS 3D* does not change. In addition, the calculation phases and parameters for the different soil layers and the column remain the same as for load eccentricity. The uniform surface load as for inclined columns is equal to 5600 KN/m^2 . Fig. 39 represents the column with different curvatures and a top view of an inclined column for the *3D FEM* calculation.

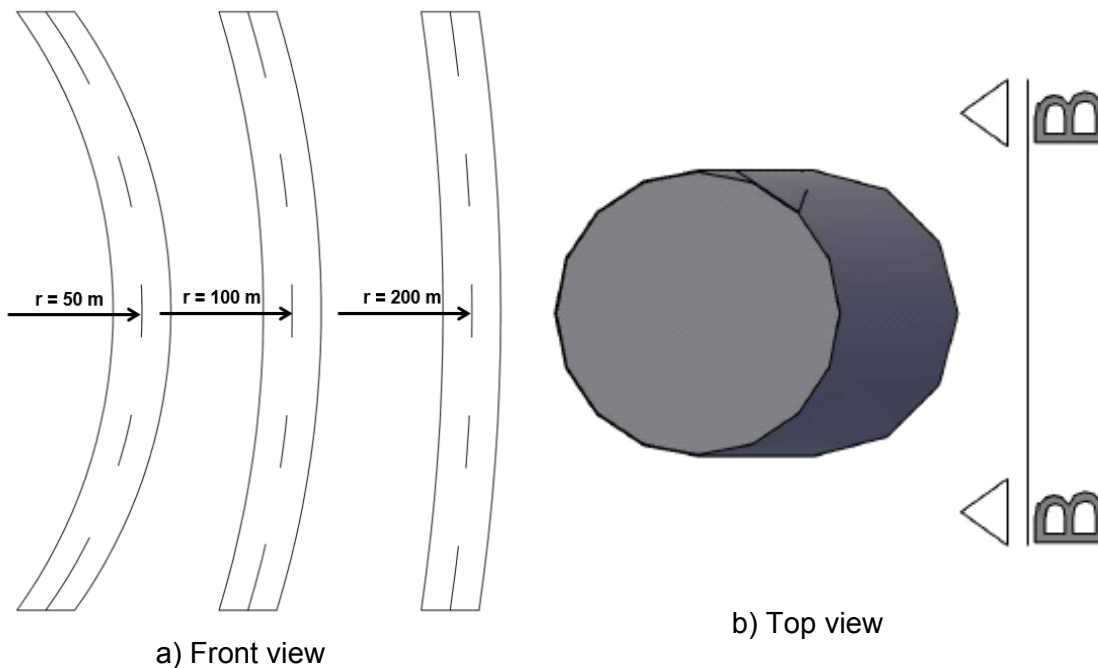


Fig. 39 Column with different curvatures for *3D FEM* calculation

7.1 Load-settlement curves

Similar to inclined columns the bearing capacity increases for columns with a curvature of $r = 100$ m and $r = 200$ m. Again, the surrounding soil that is acting against the curved column on the left side is responsible for that. The use of the shotcrete model has no influence on the load-settlement curves. For both curvatures and constitutive models the shape is almost the same.

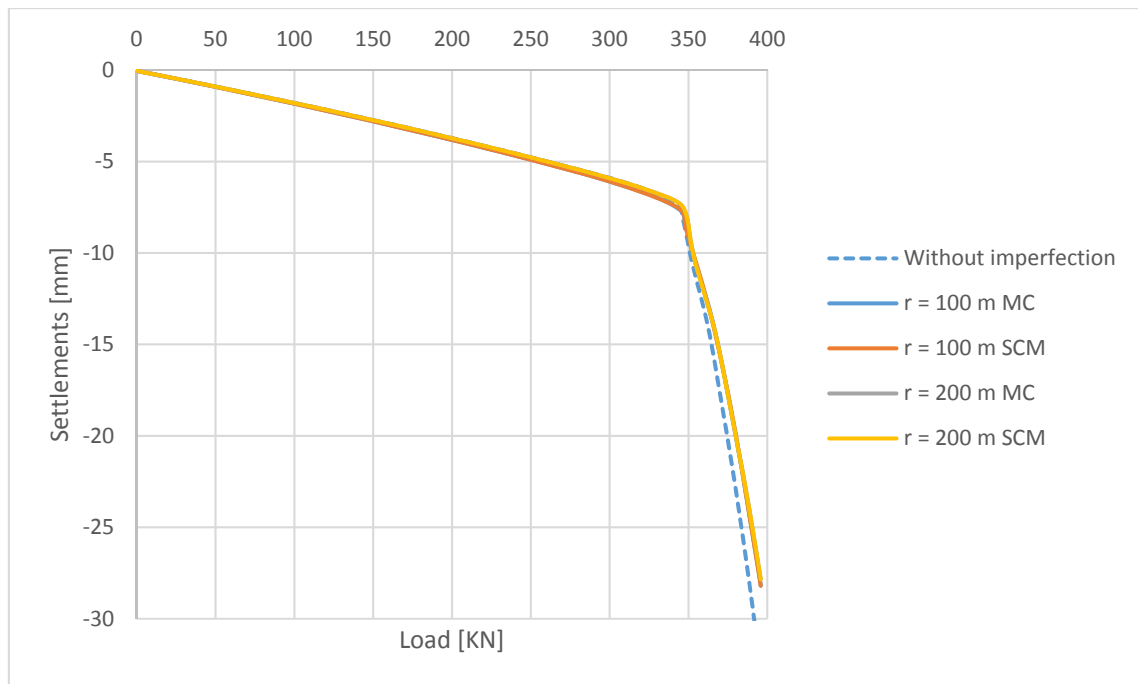


Fig. 40 Load-settlement curves for columns with curvature (MC and SCM)

7.2 Vertical stresses and principal effective stresses σ'_3

The vertical stress development for a curved column is comparable to inclined columns. For Mohr Coulomb the column is under compression in the upper part. In contrary, for the shotcrete model a small area with tensile stresses appear. The compressive and the tensile strength are not exceeded (Fig. 41).

A comparison of the principal effective stresses σ'_3 (Fig. 42) makes clear that higher tensile stresses develop for the shotcrete model. For Mohr Coulomb the range of tensile stresses in the upper part of the column is roughly from 0.0 to 100 KPa whereas for the shotcrete model tensile stresses are (in the middle turquoise area) between 300 and 400 KPa. However, the radius of the curvature of the column would have to be smaller for significant development of cracks.

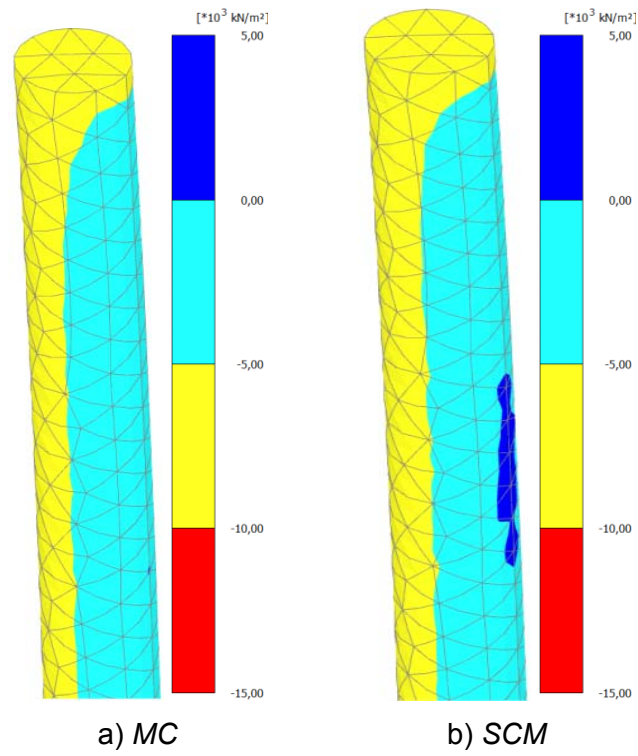


Fig. 41 Vertical stresses for curvature $r = 100$ m (MC and SCM)

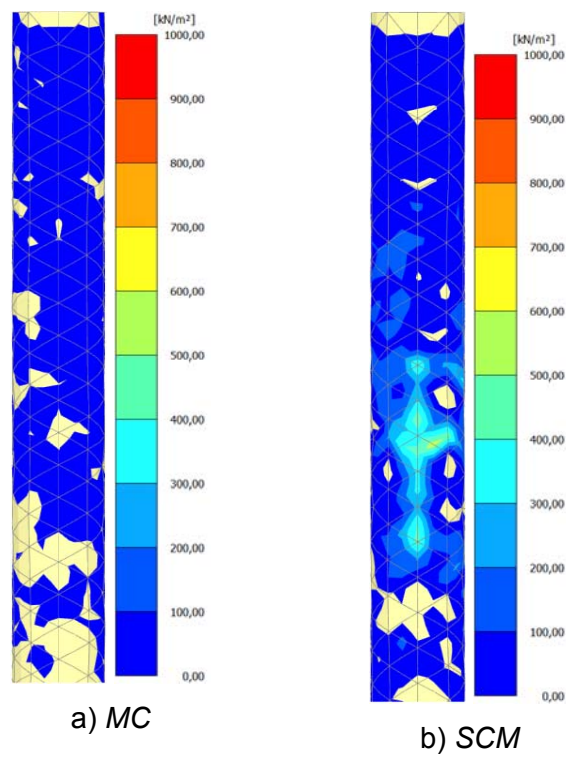


Fig. 42 Principal effective stresses σ'_3 for curvature $r = 100$ m (MC and SCM)

7.3 Normal force and bending moment

The normal force of a curved column with $r = 100$ m resulting from Mohr Coulomb and the shotcrete model have almost the same shape. The maximum positive bending moment appears in a depth of approximately 5 m with ~ 30 KNm. Mohr Coulomb gives a slightly smaller bending moment than the shotcrete model.

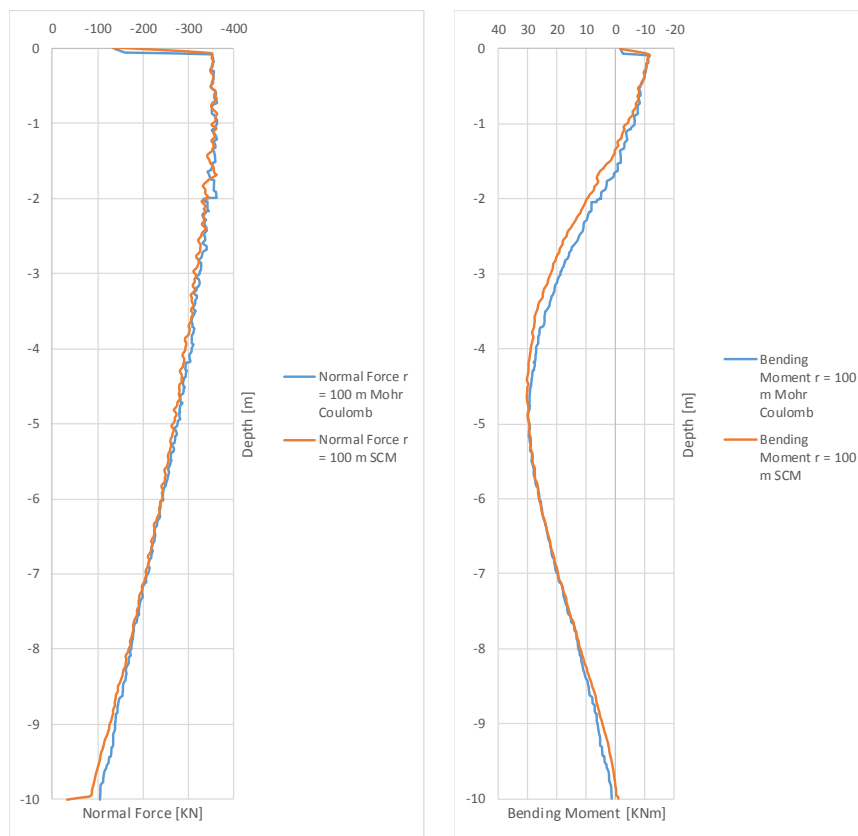


Fig. 43 Structural forces for curved column with $r = 100$ m (MC and SCM)

7.4 Activation of the “updated mesh” option

One could expect that the “updated mesh” option also influences the load-settlement curves like it does for an inclined column with $e = 10\% D$. This is not the case for a column with curvature of $r = 100$ m and $r = 200$ m.

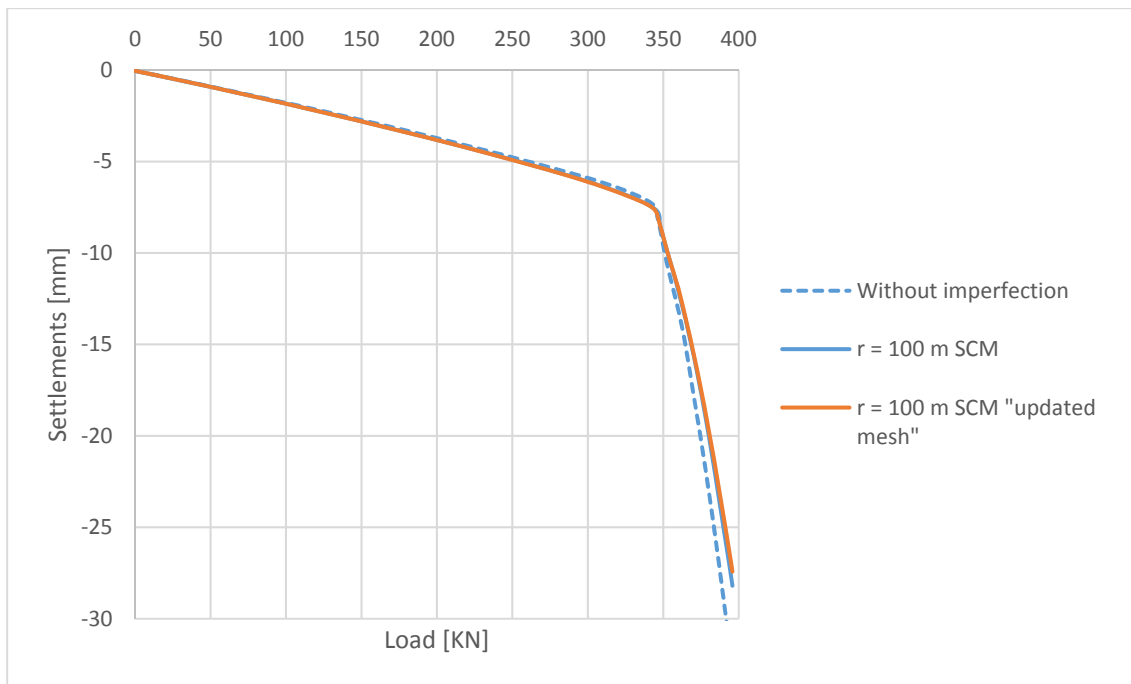


Fig. 44 Load-settlement curves with curvature and “updated mesh” option (SCM)

As curved columns tend to larger deformations during loading, the “updated mesh” option has an influence on the vertical stress development and the principal effective stresses σ'_3 . Fig. 45 has to be compared to Fig. 41 (page 38). Due to the activation of the “updated mesh” option tensile stresses appear for the Mohr Coulomb model. Comparing the vertical tensile stresses of the shotcrete model it becomes clear that the “updated mesh” option results in a bigger area in tension. Fig. 46 represents the principal effective stresses σ'_3 with the activation of the “updated mesh” option for curvature $r = 100$ m. The influence of the “updated mesh” option is not negligible. The tensile stresses increase approximately three to four times when Mohr Coulomb and the shotcrete model are compared.

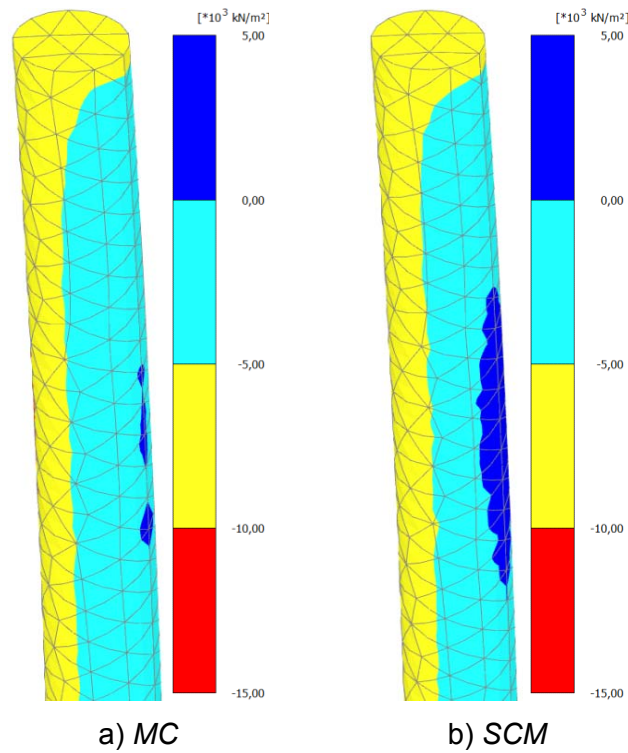


Fig. 45 Vertical stresses for curvature $r = 100$ m with “updated mesh” option (MC and SCM)

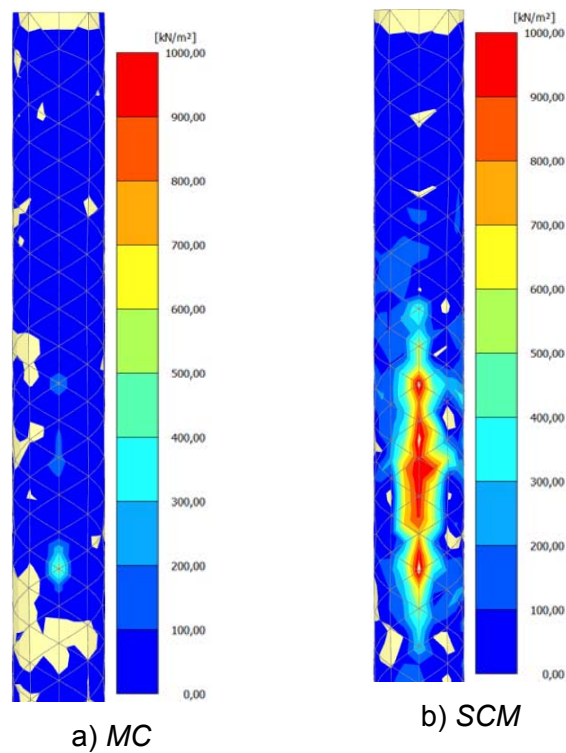


Fig. 46 Principal effective stresses σ'_3 (tensile stresses) with „updated mesh“ option (MC and SCM)

The structural forces (Fig. 47) are not influenced by the activation of the updated mesh option.

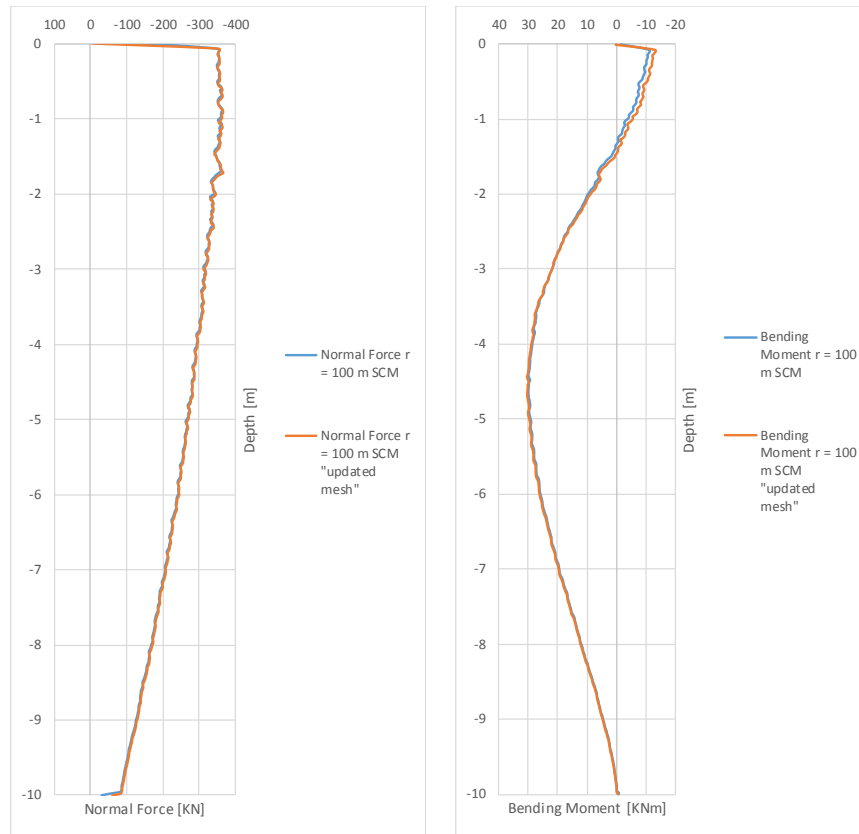


Fig. 47 Comparison of the structural forces with „updated mesh“ option (*MC* and *SCM*)

7.5 Curved column with $r = 50$ m

With an applied load of 5600 kN/m^2 for columns with $r = 200$ m and $r = 100$ m no crack pattern develops in the column. To represent a crack pattern, a *FEM* analysis of a column with $r = 50$ m is performed.

7.6 Load-settlement curves

For a curved column with $r = 50$ m one can see in Fig. 48 compared to a column without imperfection that higher settlements occur for both constitutive models. Because of this, the column may crack during loading.

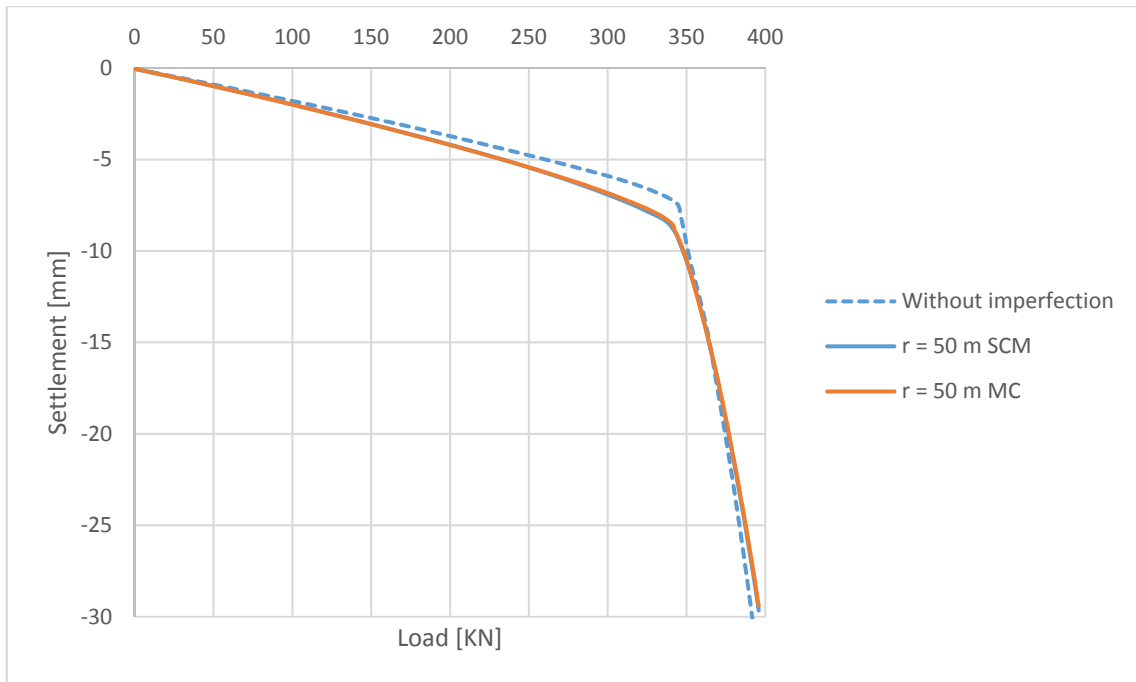


Fig. 48 Load-settlement curves for curvature $r = 50$ m (MC and SCM)

7.7 Vertical stresses

The vertical stresses for a column with curvature $r = 50$ m (Fig. 49) are different for Mohr Coulomb and the shotcrete model. Again, as it is for inclined columns, the tension area for the shotcrete model is larger than for Mohr Coulomb.

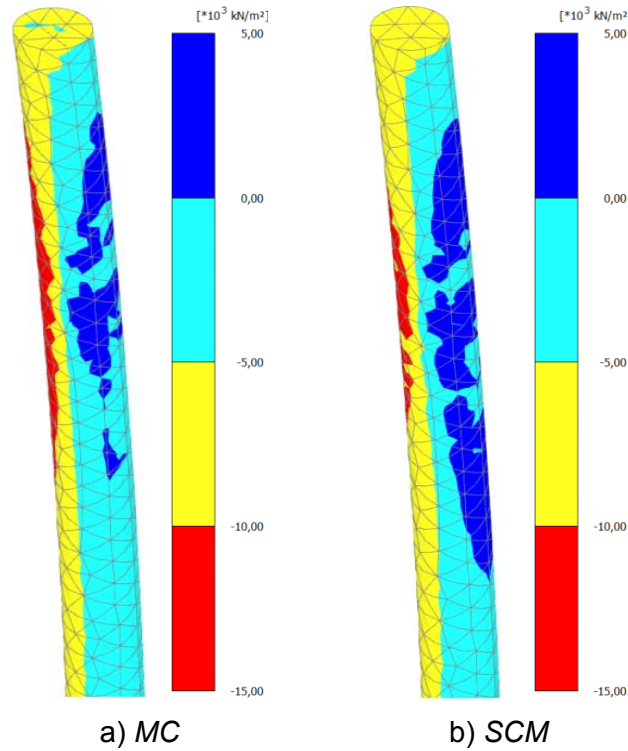


Fig. 49 Vertical stresses for curvature $r = 50$ m (MC and SCM)

Fig. 50 shows the crack pattern of such a column where the yellow area represents the cracked area. These cracks arise due to high tension forces on the right side of the column in combination with an imperfection of $r = 50$ m.

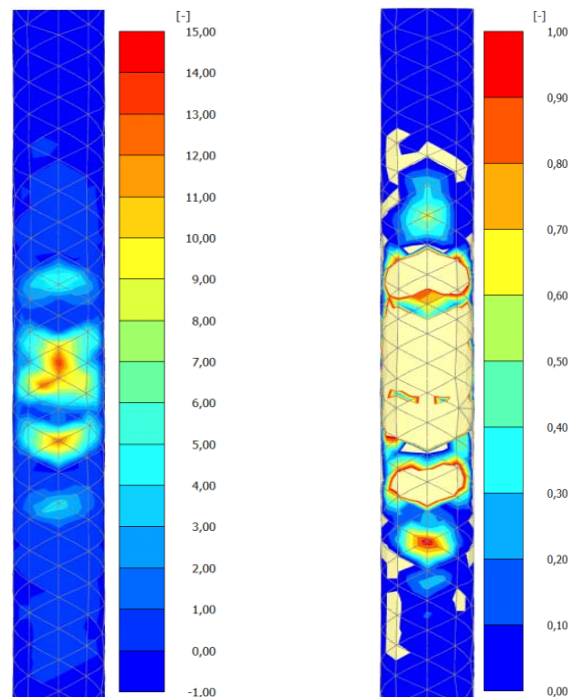


Fig. 50 Crack pattern – $G_{t,28} = 0.01$

8 Conclusion

It can be concluded that geometrical imperfections in a single grouted column have no significant influence on the bearing capacity and the load-settlement curve. Even a slight increase of bearing capacity for bulging, necking, inclination and load eccentricity is apparent in the load-settlement curves for Mohr Coulomb and a linear elastic behaviour.

In comparison to that, the shotcrete model gives partly different load-settlement curves and different stress distributions in the column concerning the vertical stress and the principle effective stress σ'_3 . Furthermore, the developed crack pattern in the column is an important information for designing ground improvements. The different imperfection types can be interpreted individually.

Necking is a more critical imperfection than bulging, especially if the necking area is in the upper part of the column. For that case, the column gets cracks in the necking area and the bearing capacity, which can be observed in the load-settlement curves, is decreasing. Consequently, the stress state in the column changes compared to a linear elastic behavior. An influence on the bearing capacity for necking in deeper parts of the column is not observed. A look on the load-settlement curves for bulging gives as expected no dramatic changes in the shape of the load-settlement curves. Therefore, the vertical stress and the principle effective stresses σ'_3 do not change.

Inclinations from $e = 1 \% D$ up to $e = 5 \% D$ have no influence on the bearing capacity. For an inclined column with $e = 10 \% D$ the entire column cracks and a difference in the shape of the load-settlement curves between Mohr Coulomb and the shotcrete model is the consequence. The vertical stress situation in the column is also quite different. The shotcrete model shows a bigger area of tension in the column. The development of cracks in this area is quite well visible for different $G_{t, 28}$ values, which defines whether the concrete behaves more brittle or ductile. Due to the crack formation in the column the bending moments are smaller in comparison to Mohr Coulomb.

Load eccentricity of $e = 1/8 B$ and $e = 1/7 B$ has no significant influence on the load-settlement curves for both constitutive models. The geometry of the column does not change and therefore the skin friction and the tip resistance are the same as for normally loaded columns without imperfection. The stress distribution is the same as for inclined columns. The shotcrete model allows tension forces but the column does not crack.

The last imperfection type is curvature. A curvature larger than 100 m has no impact on the load-settlement curve for both constitutive models. If the curvature is reduced to 50 m

the bearing capacity of the column gets reduced due to the cracks in the column. The vertical stress distribution is similar as for inclined columns.

9 Embankment

Second part of this thesis is a numerical analysis of an embankment, constructed on cemented columns in alluvial sediments (Estuarine clay). Although modelling piles is a 3D problem, different possibilities to do a *FEM* analysis of piles in 2D plane strain exist:

1. Block with “smeared properties”
2. wall: $B = D'$ with reduced E
3. wall: $B < D'$ with consistent E
4. plate without end bearing
5. plate with end bearing
6. embedded beam row

9.1 Model for *FEM* analysis in PLAXIS 2D

Fig. 51 shows the symmetric model with its dimensions. The profile consists of four soil layers and the constructed embankment with an applied load of 34 KPa. Under the embankment, a load transfer platform (*LTP*) and the columns with a diameter of 0.35 m and a spacing of 2 m are installed. The groundwater level is located at ground surface. Since the soil layers have low permeability, it is important to consider consolidation and excess pore pressures during construction of the embankment. A very fine mesh for the model is applied and for the *FEM* analysis the Hardening Soil Small model, the Soft Soil Creep model and the Mohr Coulomb model are used.

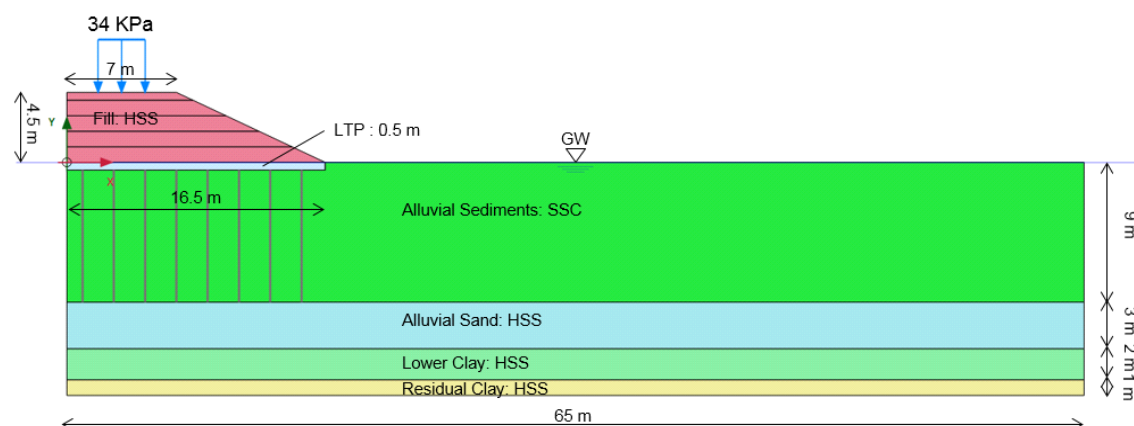


Fig. 51 Soil profile for analysis

9.1.1 Calculation phases

The initial phase consists of a K_0 procedure. The columns and the *LTP* (load transfer platform) are already installed. The embankment construction is divided into five

consolidation analysis (staged construction: 4 x 1 m layers + 1 x 0.5m layers and a time interval of 10 days) with a consolidation phase of 10 days in between. After completion of the dam construction, a loading phase (34 KPa) is introduced and followed by a consolidation analysis until a degree of 90 % of consolidation is reached. The last two phases are a safety phase after the last consolidation phase and a loading phase until failure. In the safety phase only the FOS of the embankment is calculated because the columns are modelled as linear elastic material. Fig. 52 shows the phases explorer with the list of the calculation phases.

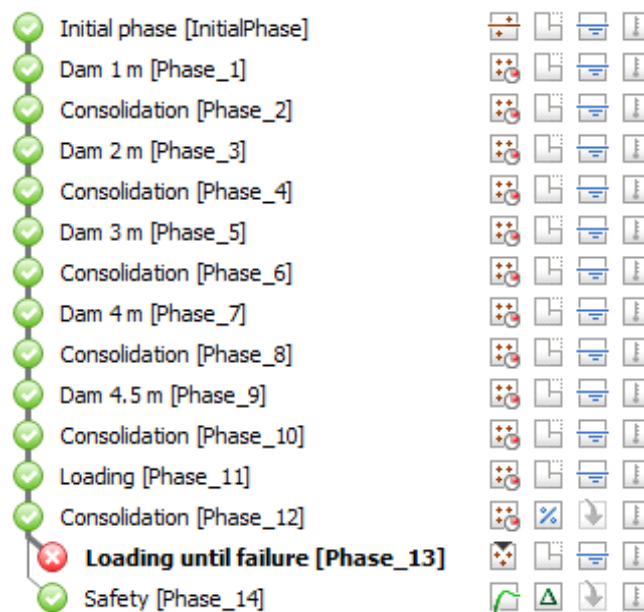


Fig. 52 phases explorer

9.1.2 Soil parameters

The following tables represent the soil properties for the different soil layers.

Tab. 7 Soil properties fill

Parameter	Name	Value	Unit
material model	HSS	[-]	[-]
specific weight	γ	18	[KN/m ³]
oedometer modulus	$E_{\text{oed,soil}}^{\text{ref}}$	40.5	[MPa]
secant stiffness	E_{50}^{ref}	40.5	[MPa]
unloading/reloading stiffness	$E_{\text{ur}}^{\text{ref}}$	121.5	[MPa]
reference pressure	p_{ref}	100	[KPa]

power for stress-level dependency	m	0.5	[-]
friction angle	φ'	35	[°]
cohesion	c'	5	[KPa]
dilatancy angle	ψ'	0	[°]
reference shear modulus	G_0^{ref}	270	[MPa]
threshold shear strain	$\gamma_{0.7}$	0.15E-3	[-]
drainage type	[-]	Undrained (A)	[-]
permeability	k_x	90	[m/d]
permeability	k_y	90	[m/d]

Tab. 8 Soil properties alluvial sand

Parameter	Name	Value	Unit
material model	HSS	[-]	[-]
specific weight	γ	19	[KN/m ³]
oedometer modulus	$E_{\text{oed,soil}}^{\text{ref}}$	14	[MPa]
secant stiffness	E_{50}^{ref}	14	[MPa]
unloading/reloading stiffness	$E_{\text{ur}}^{\text{ref}}$	42	[MPa]
reference pressure	p_{ref}	100	[KPa]
power for stress-level dependency	m	0.5	[-]
Friction angle	φ'	33	[°]
cohesion	c'	0	[KPa]
dilatancy angle	ψ'	3	[°]
reference shear modulus	G_0^{ref}	168	[MPa]
threshold shear strain	$\gamma_{0.7}$	0.15E-3	[-]
drainage type	drainage type	Undrained (A)	[-]
permeability	k_x	0.04	[m/d]
permeability	k_y	10	[m/d]

Tab. 9 Soil properties lower clay

Parameter	Name	Value	Unit
material model	HSS	[-]	[-]
specific weight	γ	18	[KN/m ³]
oedometer modulus	$E_{\text{oed,soil}}^{\text{ref}}$	10	[MPa]
secant stiffness	E_{50}^{ref}	10	[MPa]
unloading/reloading stiffness	$E_{\text{ur}}^{\text{ref}}$	30	[MPa]
reference pressure	p_{ref}	100	[KPa]
power for stress-level dependency	m	0.8	[-]
friction angle	φ'	24	[°]
cohesion	c'	15	[KPa]
dilatancy angle	ψ'	0	[°]
reference shear modulus	G_0^{ref}	120	[MPa]
threshold shear strain	$\gamma_{0.7}$	0.15E-3	[-]
drainage type	drainage type	Undrained (A)	[-]
permeability	k_x	0.04	[m/d]
permeability	k_y	0.02	[m/d]

Tab. 10 Soil properties residual clay

Parameter	Name	Value	Unit
material model	HSS	[-]	[-]
specific weight	γ	19	[KN/m ³]
oedometer modulus	$E_{\text{oed,soil}}^{\text{ref}}$	20	[MPa]
secant stiffness	E_{50}^{ref}	20	[MPa]
unloading/reloading stiffness	$E_{\text{ur}}^{\text{ref}}$	60	[MPa]
reference pressure	p_{ref}	100	[KPa]
power for stress-level dependency	m	0.8	[-]
friction angle	φ'	24	[°]

cohesion	c'	30	[KPa]
dilatancy angle	ψ'	0	[°]
reference shear modulus	G_0^{ref}	240	[MPa]
threshold shear strain	$\gamma_{0.7}$	0.15E-3	[-]
drainage type	drainage type	Undrained (A)	[-]
permeability	k_x	0.09	[m/d]
permeability	k_y	0.09	[m/d]

Tab. 11 Soil properties alluvial sediments

Parameter	Name	Value	Unit
material model	SSC	[-]	[-]
specific weight	γ	16	[KN/m ³]
initial void ratio	e_{init}	1.546	[-]
friction angle	ϕ'	24	[°]
cohesion	c'	3	[KPa]
dilatancy angle	ψ'	0	[°]
compression index	C_c	0.321	[KPa]
swelling index	C_s	0.058	[KPa]
creep index for secondary compression	C_α	0.0035	[KPa]
drainage type	[-]	Undrained (A)	[-]
permeability	k_x	2.5E-3	[m/d]
permeability	k_y	6.0E-4	[m/d]

Tab. 12 Soil properties LTP

Parameter	Name	Value	Unit
material model	MC	[-]	[-]
specific weight	γ	22	[KN/m ³]
Young's modulus	E'	60	[MPa]
Poisson's ratio	ν'	0.3	[-]
friction angle	φ'	38	[°]
cohesion	c'	0	[KPa]
dilatancy angle	ψ	8	[°]

9.2 FEM analysis with columns modelled as “block” with “smeared properties”

Fig. 53 shows the model with the exchanged “block” and the cross section where the settlement trough (Fig. 54) just below the embankment is evaluated. The properties of the “block” below the embankment represents Tab. 13.

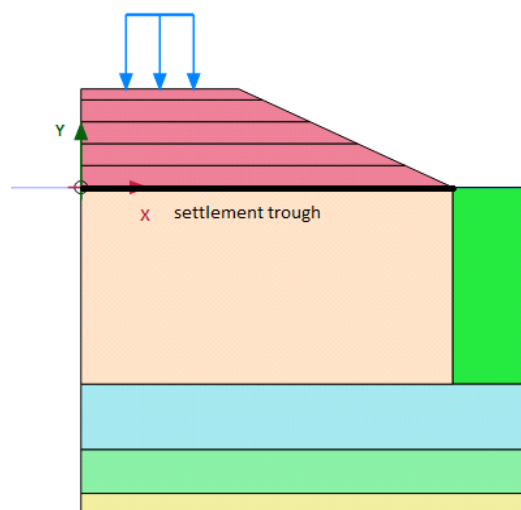


Fig. 53 FEM model with exchanged “block” with “smeared properties”

Tab. 13 Properties of the “block” below the embankment

Parameter	Name	Value	Unit
material model	MC	[-]	[-]
specific weight	γ	20	[KN/m ³]
Young’s modulus	E'	18	[MPa]
Poisson’s ratio	ν'	0.3	[-]
friction angle	φ'	35	[°]
cohesion	c'	19	[KPa]
dilatancy angle	ψ	0	[°]

The maximum settlements of ~ 40 mm are in the centre of the embankment. They are decreasing to ~ 10 mm at the toe of the embankment.

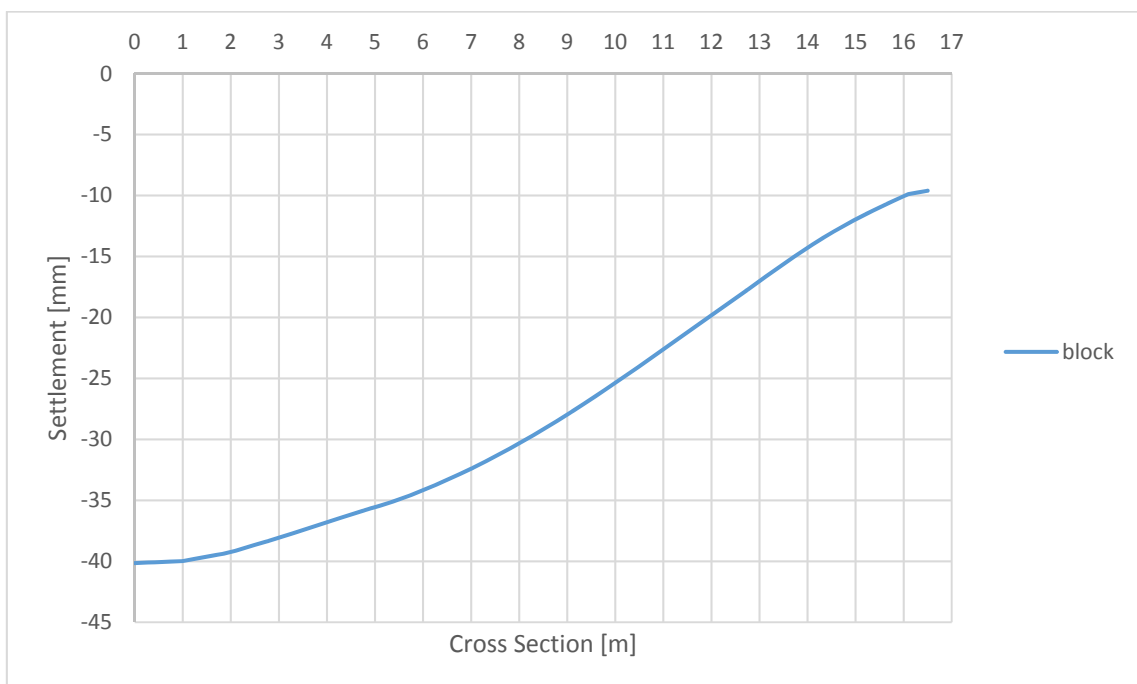


Fig. 54 Settlement trough for “block” with “smeared properties”

9.3 FEM analysis with columns modelled as “wall”

The FEM models in 2D plane strain for columns modelled like a “wall” and the cross section where the settlement trough is evaluated, are shown in Fig. 55. Around the columns, interfaces are defined with a R_{inter} factor of 0.67 for the adjacent soil. The column properties are summarized in Tab. 14.

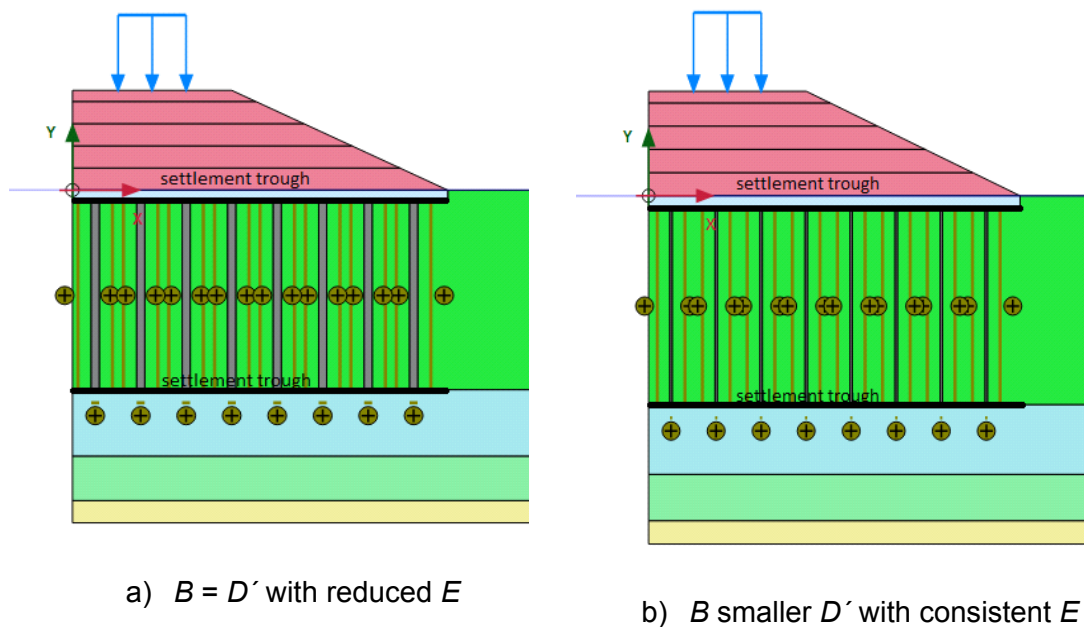


Fig. 55 FEM model for columns modelled like a “wall”

Tab. 14 Properties of the column

Parameter	Name	Value	Unit
material model	LE	[-]	[-]
Young's modulus	E'	10.8	[GPa]
Poisson's ratio	ν'	0.3	[-]
specific weight	γ	23	[KN/m ³]

Since modelling columns is a 3D problem, the width of the column or the Young's modulus have to be changed in case of plane strain modelling. Fig. 56 explains the plane strain approach for modelling columns. The ratio between area and stiffness has to be considered.

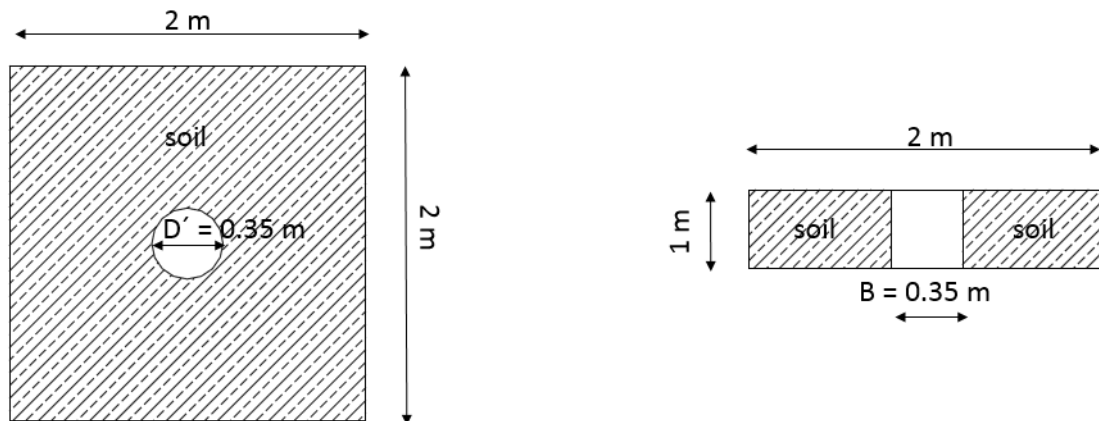


Fig. 56 Plane strain approach

With the following formula, the right stiffness and width of the column in plane strain can be calculated.

$$\frac{D'^2 * \pi}{4} * E_{column} + \left(4 - \frac{D'^2 * \pi}{4}\right) * E_{soil} = B * E_{column} + (2 - B) * E_{soil} \quad (1)$$

D' [m] diameter of the column in a unit cell

B [m] width of the column

E_{column} [N/m²] Young's modulus of the column

E_{soil} [N/m²] Young's modulus of the surrounding soil

$$\frac{0.35^2 * \pi}{4} * 10800 + \left(4 - \frac{0.35^2 * \pi}{4}\right) * 4.5 = 0.35 * E + (2 - 0.35) * 4.5$$

$$E = \sim 3000 \text{ MPa}$$

$$\frac{0.35^2 * \pi}{4} * 10800 + \left(4 - \frac{0.35^2 * \pi}{4}\right) * 4.5 = B * 10800 + (2 - 0.35) * 4.5$$

$$B = \sim 0.1 \text{ m}$$

If the width (B) of the column in plane strain is the same as the diameter (D') of the column in a unit cell the Young's modulus has to be decreased to 3000 MPa. On the contrary, if the Young's modulus stays the same the width of the column has to be decreased to 0.1 meters.

The deformed mesh $|u|$ after loading until failure for both types of modeling columns as a “wall” is shown in Fig. 57.

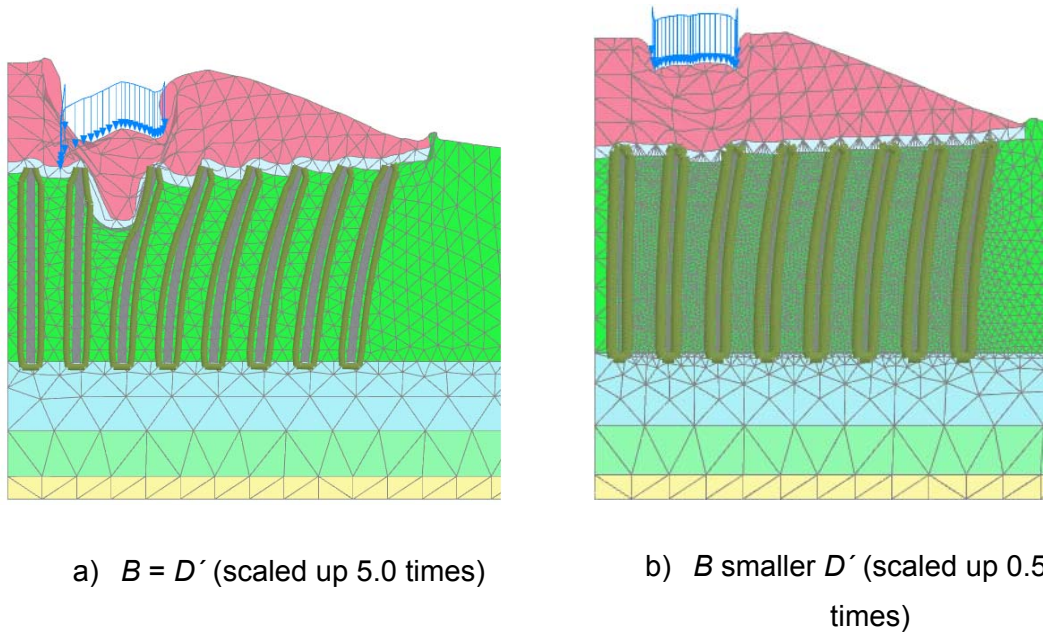


Fig. 57 Deformed mesh $|u|$

Through the different input of the stiffness for the columns in PLAXIS different stress distributions in the piles develop. Piles with a higher stiffness tend to attract the force during the loading phase. Due to this fact, for piles B smaller D' , higher effective normal stresses can be observed during the loading phase. This effect can be seen in Fig. 58 in three different depths from the ground surface of the column.

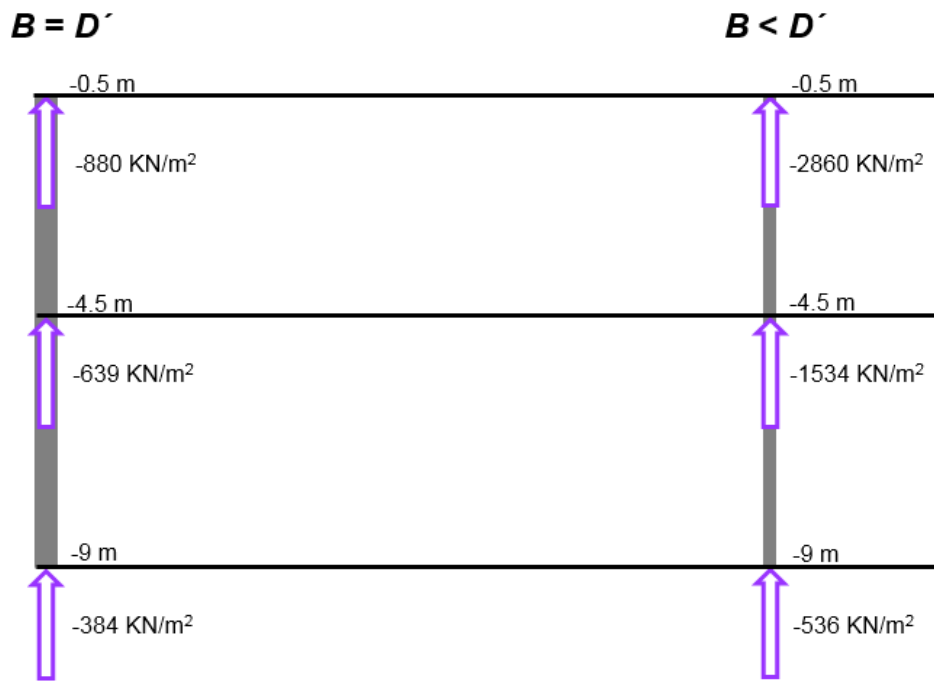


Fig. 58 Normal stress distribution of the columns

Fig. 59 represents the settlement trough on top of the columns. For columns B smaller D' the settlements around the column are clearly higher than for columns $B = D'$. This results from a geometrical problem of the column. By decreasing the diameter of the column in plane strain, the problem of punching in (Fig. 60) occurs in the soil layer above or under the column.

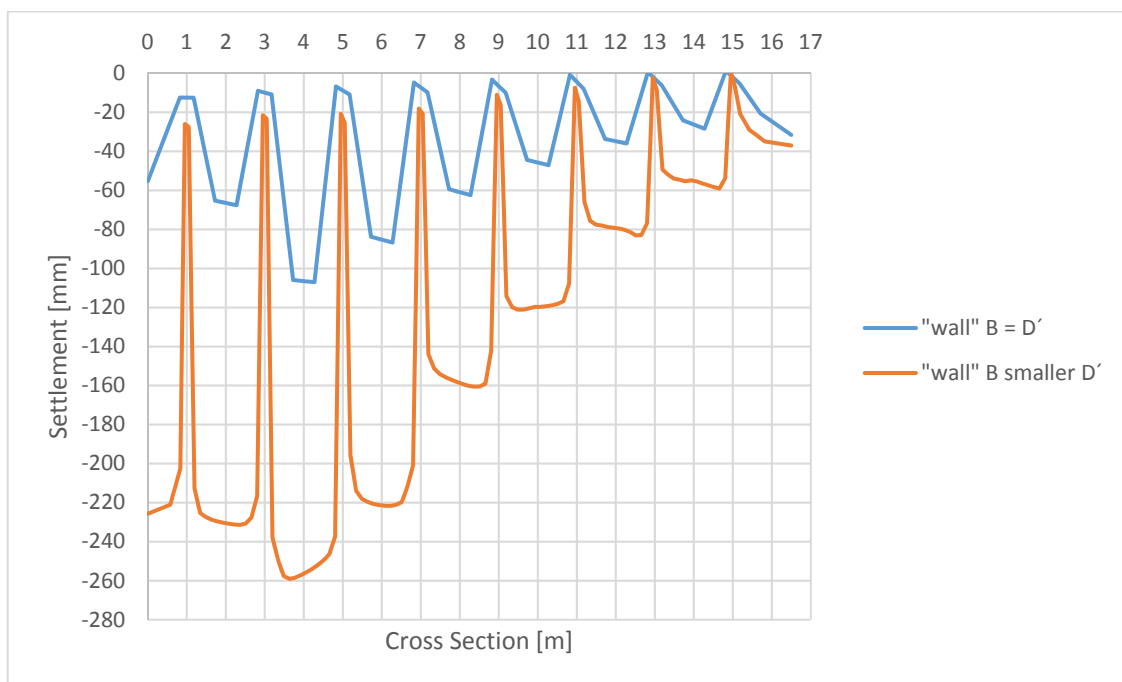
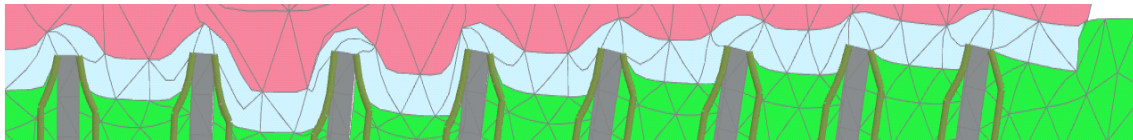
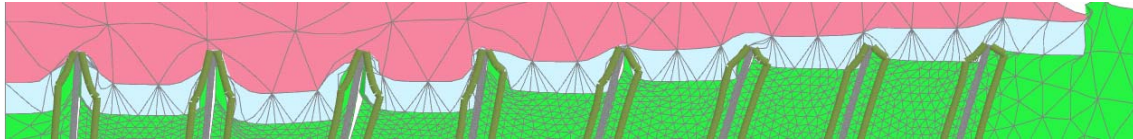


Fig. 59 Settlement trough on top of the columns



Deformed mesh for $B = D'$



Deformed mesh for B smaller D'

Fig. 60 Stamping in of the columns in the *LTP*

9.4 FEM analysis with columns modelled as plate

Also a calculation with plate elements (length: 8.5 m) is performed. Fig. 61 represents the *FEM* model and Tab. 15 the plate properties.

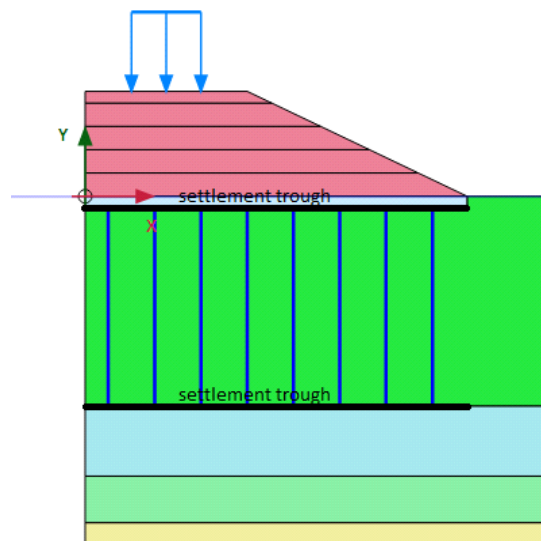


Fig. 61 *FEM* model for columns modelled like a plate

Tab. 15 Plate properties

Parameter	Name	Value	Unit
material type	elastic	[-]	[-]
Isotropic	yes		

End bearing	yes/no		
axial stiffness	EA	3.78E6	[KN/m]
Flexural rigidity	EI	38.59E3	[KNm ² /m]
thickness	d	0.35	[m]
specific weight	w	8	KN/m/m
Poisson´s ratio	ν'	0.3	[-]

In the material data set of plates, it is possible to use end bearing of plates. Normally plate elements have no thickness and therefore no end bearing. If end bearing is considered, an elastic zone is developed at the bottom of the plates. (PLAXIS 2D, 2016)

This effect can be observed in Fig. 62. On the left side the calculation is performed with plates without end bearing. It is clearly visible that the plate elements have moved into the sand layer. In contrary to that, the right picture shows the deformed mesh $|u|$ where an elastic zone is developed at the bottom of the plates. Therefore, no move into the sand layer occurs.

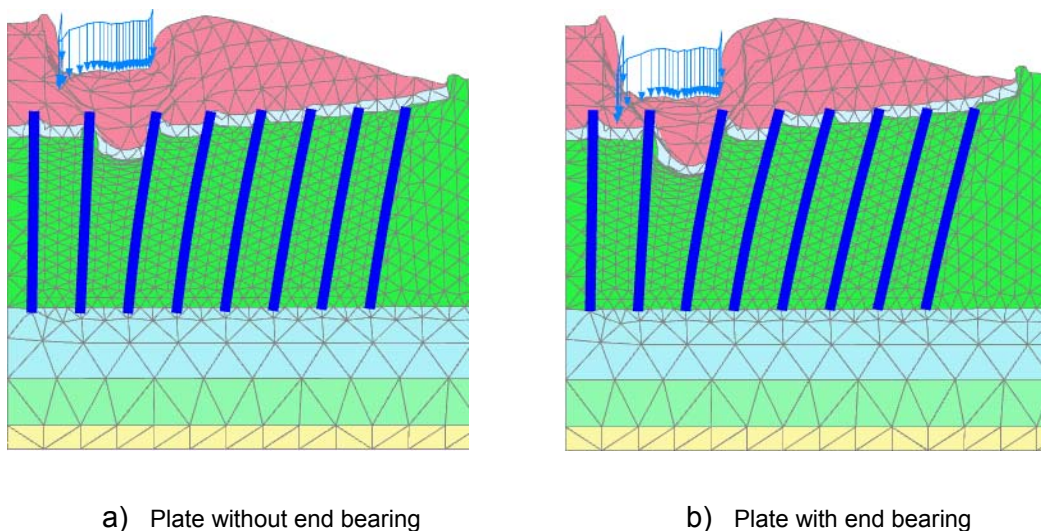


Fig. 62 Deformed mesh $|u|$

Considering the settlement trough (Fig. 63) the difference between plate elements with and without end bearing is also evident. Plate elements without end bearing produce higher settlements.

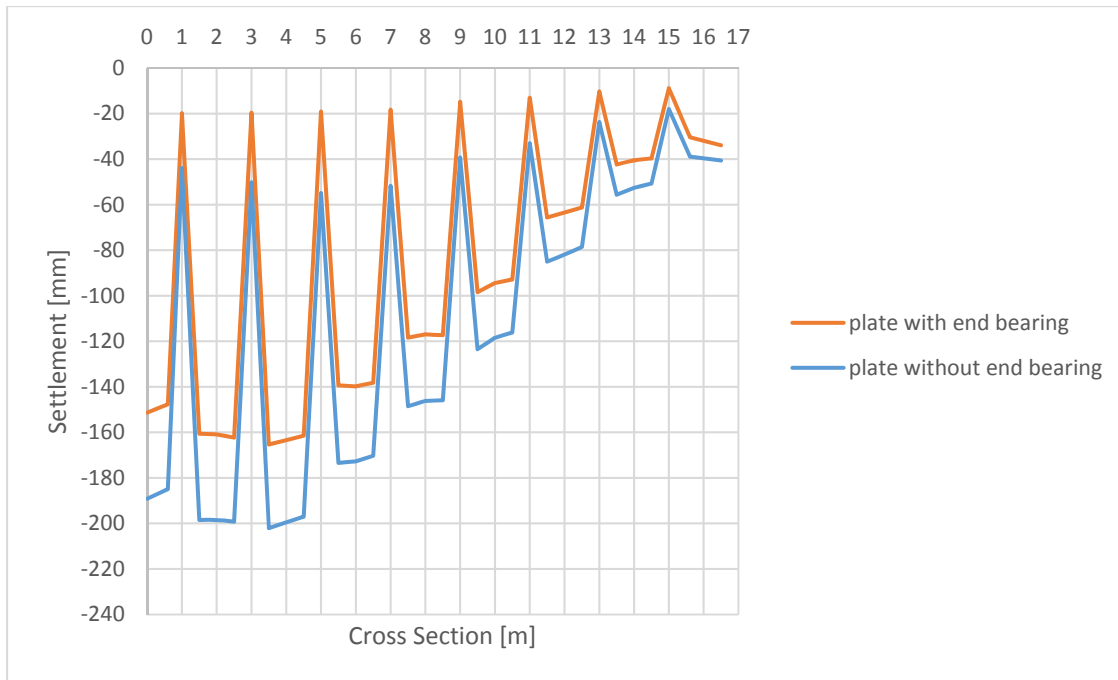


Fig. 63 Settlement trough on top of the plates

9.5 FEM analysis with columns modelled as embedded beam row

An embedded beam row is installed under the embankment (Fig. 64). The connection point is set to “Hinged”. This means that the beam is connected directly with the element where the connection point is located. Therefore, they have the same displacement but not the same rotation (PLAXIS 2D, 2016). The chosen parameters of the embedded beam row can be seen in Tab. 16.

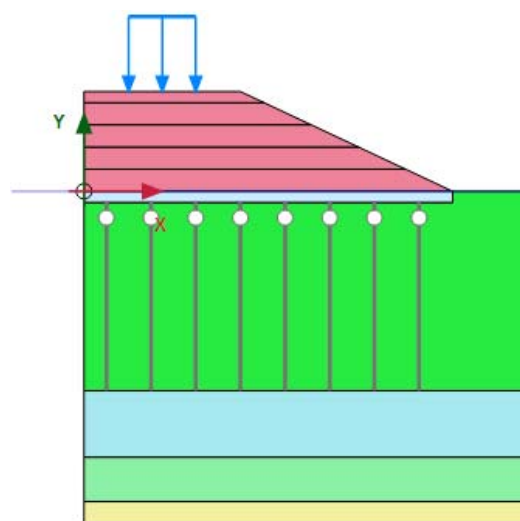
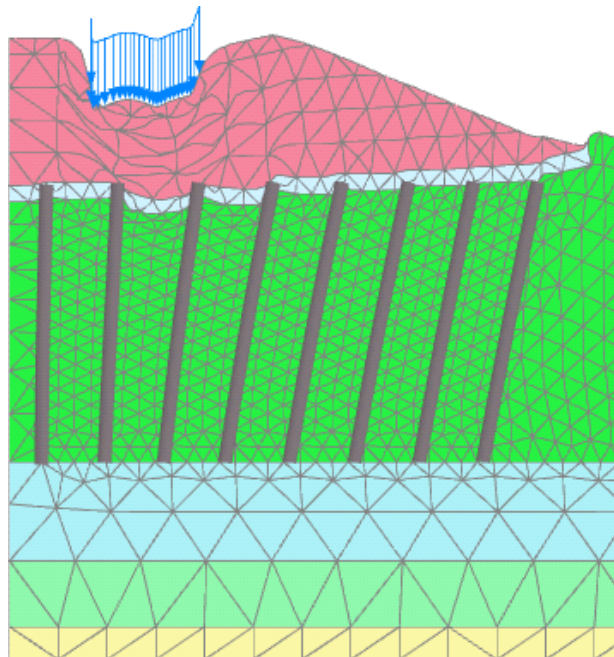


Fig. 64 FEM model for columns modelled with an embedded beam row

Tab. 16 Embedded beam row properties

Parameter	Name	Value	Unit
material type	elastic	[-]	[-]
Young's modulus	E	10.8	[GPa]
specific weight	γ	23	[kN/m ³]
diameter	D	0.35	[m]
axial skin friction	T_{skin}	30	[kN/m]
lateral skin friction	T_{lat}	30	[kN/m]
base resistance	F_{max}	200	kN
interface stiffness factor	[-]	default	[-]

The deformed mesh $|u|$ after loading until failure (Fig. 65) from the calculation with the embedded beam row looks quite similar to Fig. 62.

Fig. 65 Deformed mesh $|u|$

The settlement of the embedded beam row (Fig. 66) is significantly higher than for columns modelled as plate or "wall" since the bearing capacity (F_{max}) is not reached.

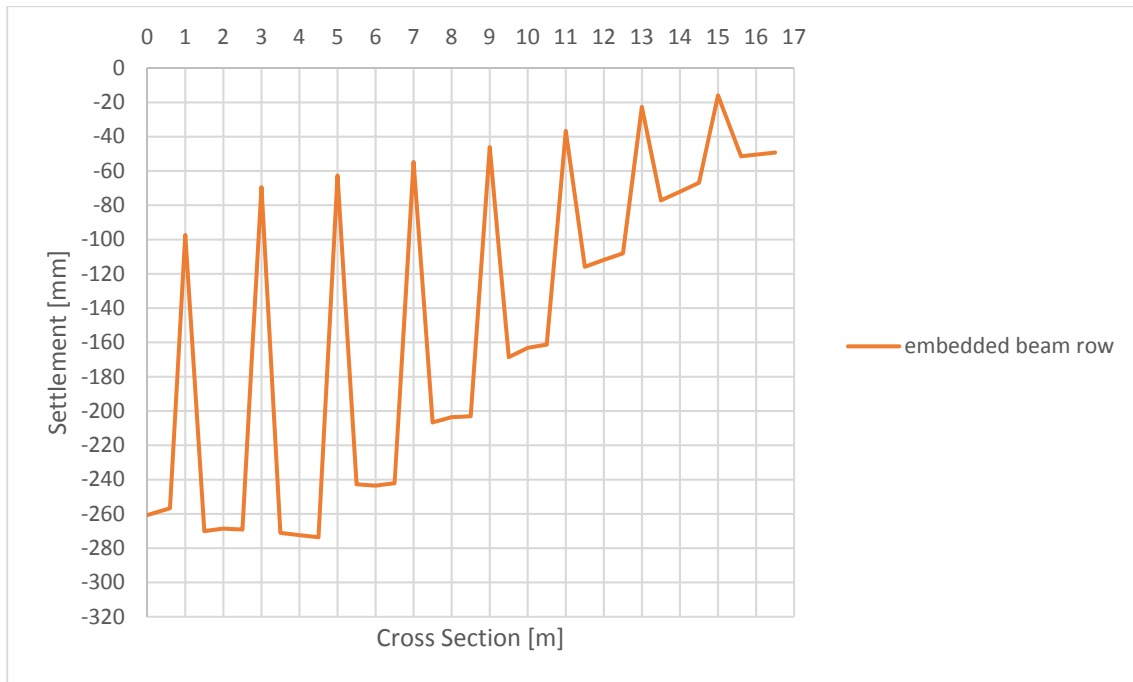


Fig. 66 Settlement trough on top of the embedded beam row

9.6 3D FEM analysis

A calculation with a 3D FEM model as shown in (Fig. 67) was also performed. Therefore, the plane strain model is extended 2 m in depth. The columns are modelled as volume piles. For the pile in the centre of the embankment, settlements of ~ 26 mm can be observed. The maximum settlement of the soil between the columns is below the surface load and ~ 80 mm (Fig. 68).

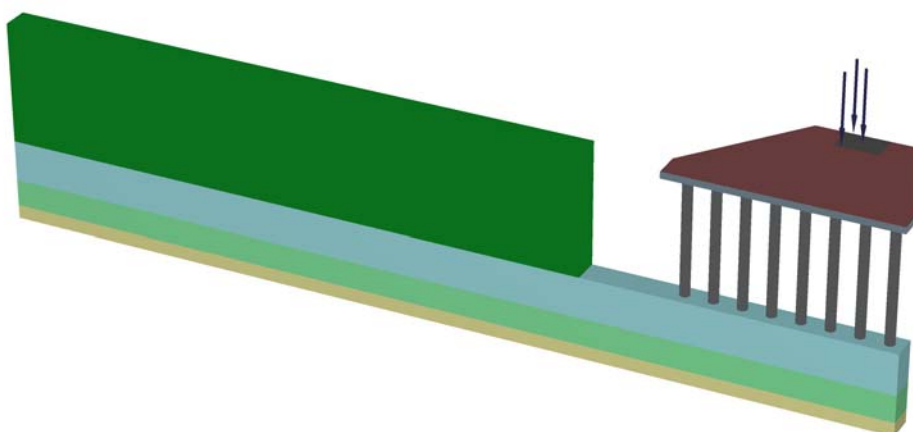


Fig. 67 3D model

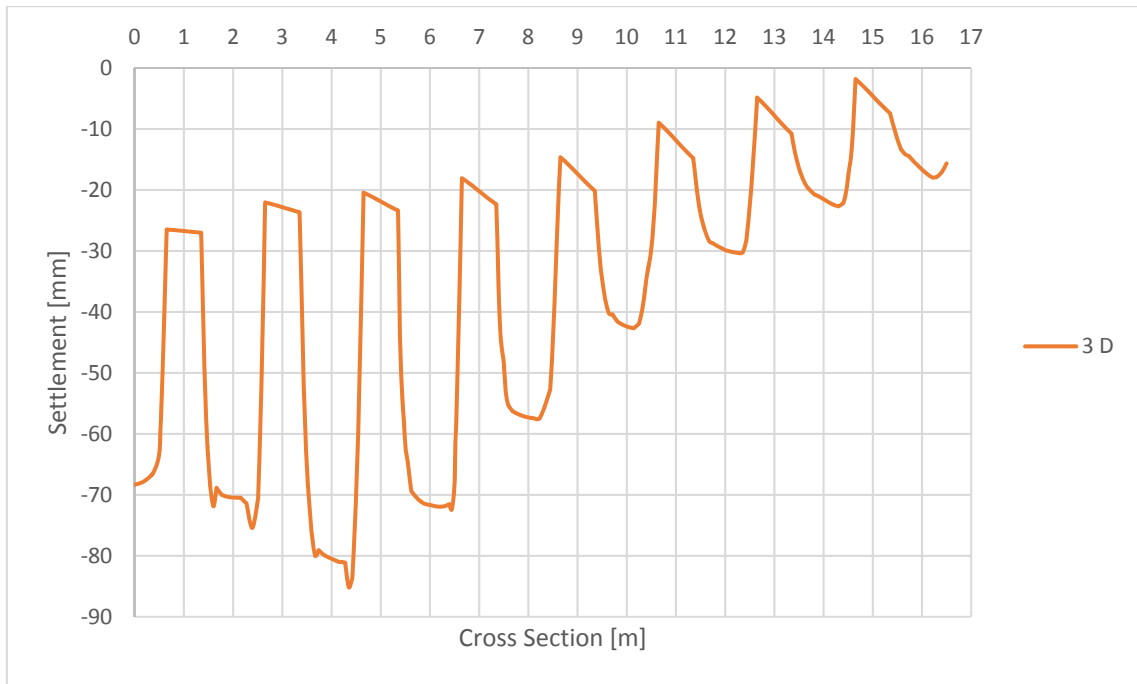


Fig. 68 Settlement trough on top of the columns

In addition, a calculation where the stiffness of the LTP is increased from 60 MPa to 100 MPa is performed in order to optimize load distribution. As shown in Fig. 69 the stiffness of the LTP has no big influence on the settlement trough.

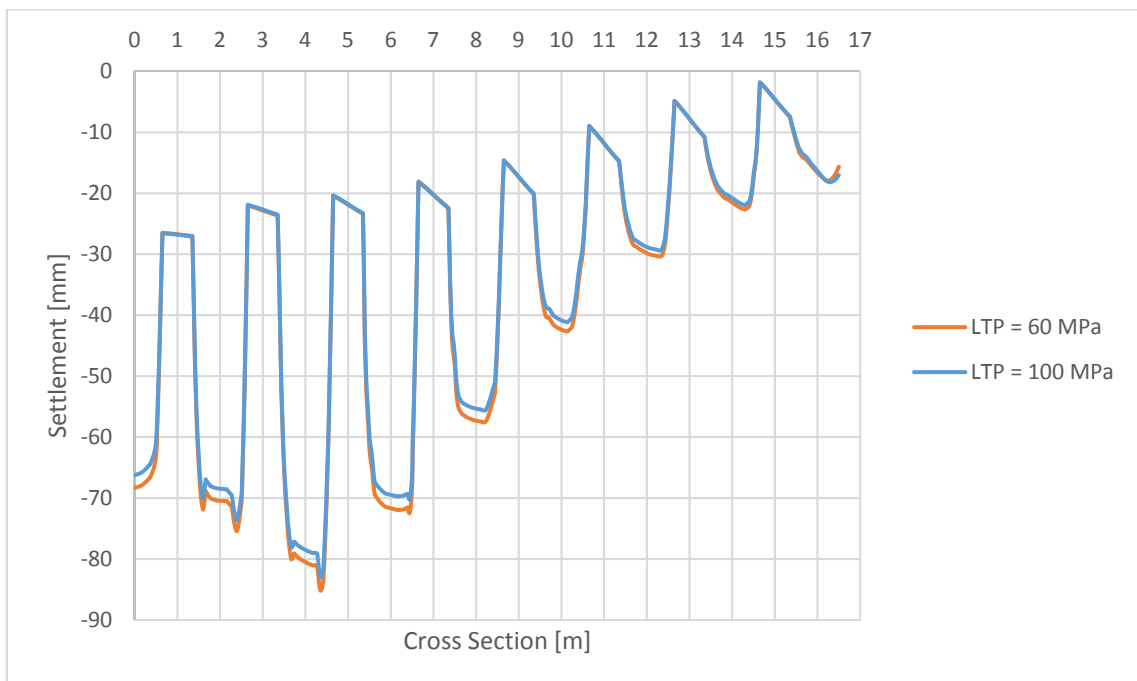


Fig. 69 Comparison of the settlement trough for different stiffness of the LTP

Fig. 70 represents all different load-settlement troughs on top of the columns combined in one graph. One can see that there is quite a good accordance concerning the settlements of the columns. The embedded beam row overestimates the settlements but the significant differences are observed in displacements of the soil between the columns.

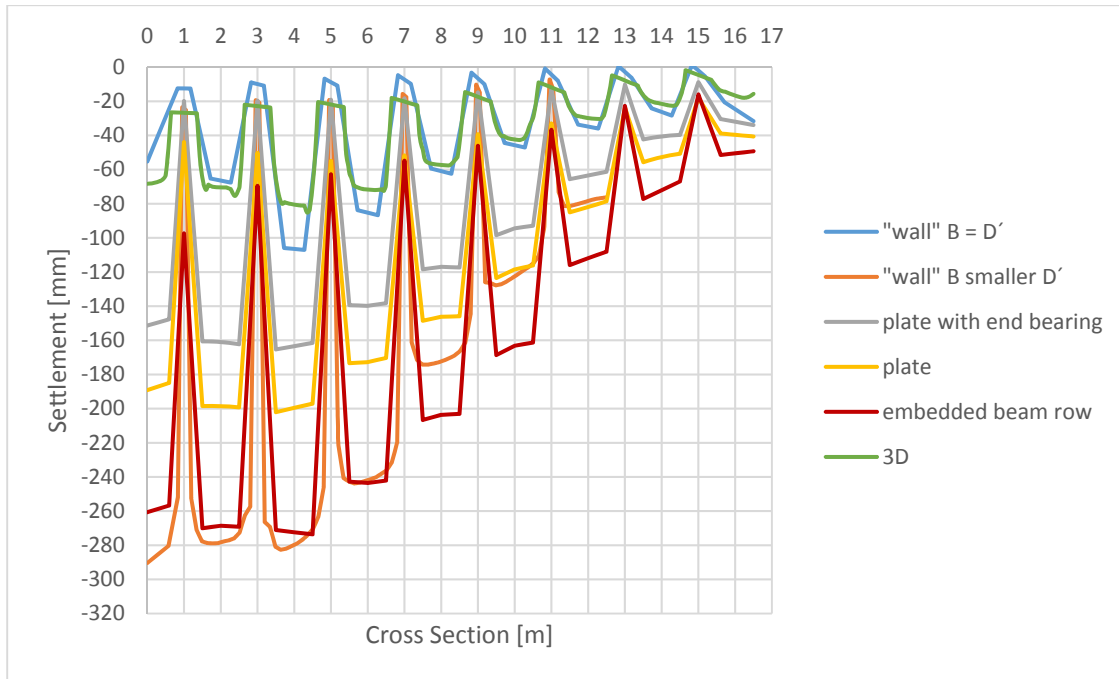


Fig. 70 Load-settlement trough on top for all different types of calculations

10 Conclusion

It has to be mentioned here, that the final chapter is supposed to be a starting point to investigate the different possibilities for modelling piles/columns in *2D* plane strain. A look on the settlement troughs for all different models makes it clear that the settlements of the columns itself are relatively low compared to the soil in between. The reason for this is a relatively stiff layer where the piles are embedded. Therefore, the complete negative skin friction is acting on the piles. A calculation with floating columns would be the next logical step. Therefore the length of the columns has to be decreased or the sand layer below the columns defined as alluvial sediments.

In the examples, it is shown that in principal the settlements of the columns for all types of modeling piles are composing well except for the embedded beam row.

If one looks at the deformed mesh after loading until failure it is quite the same for all examples. Furthermore, it is clearly visible that columns B smaller D' are punching in the *LTP* above compared to columns with $B = D'$. For plate elements with and without end bearing the difference concerning settlements of the plates are also obvious.

The settlement trough of a *3D* calculation with two different stiffness of the *LTP* is almost the same. Hence modelling columns is a *3D* problem, this result should be the most reliable one.

11 Literature

Bohn, C. (2015)

Serviceability and safety in the design of rigid inclusions and combined pile-raft foundations. Civil Engineering. Ph.D. Thesis, Université Paris-Est, 2015 <NNT: 2015PESC1096>. <tel-01259962>

Brinkgreve, R.B.J.; Kumarswamy, S.; Swolfs, W.M. (2016)

PLAXIS 2D Reference Manual 2016. Build 8122. Plaxis bv. Delft, The Netherlands

Brinkgreve, R.B.J.; Kumarswamy, S.; Swolfs, W.M. (2016)

PLAXIS 3D Reference Manual 2016. Build 8327. Plaxis bv. Delft, The Netherlands

Schädlich, B.; Schweiger, H.F. (2016)

SHOTCRETE MODEL Implementation, validation and application. Internal report, Graz University of Technology

Schweiger, H.F.; Schädlich, B.; Sedighi, P.; Saurer, E.; Marcher, T.; Henke, S.; Borchert, K.-M. (2014)

Finite element analysis of tunnel excavation and ground improvement techniques employing a new constitutive model for shotcrete. Proceedings 14th International Conference Computer Methods and Recent Advances in Geomechanics (Oka, Murakami, Uzuoka & Kimoto, eds.) Taylor & Francis Group, London, 2014, 71-80

Schweiger, H.F.; Sedighi, P.; Henke, S.; Borchert, K.-M. (2014)

Numerical modelling of ground improvement techniques considering tension softening. Proc. Geotechnical Aspects of Underground Construction in Soft Ground (Yoo Park, Kim & Ban, eds) CRC Press, 2014, 209-214

12 Appendix A: Inclined Columns

In addition, this part shows the structural forces, vertical stresses and principal effective stresses from inclined columns with $e = 5, 2, 1 \% D$. A closer look at the structural forces for Mohr Coulomb model and the shotcrete model makes it clear that the difference of the bending moment is getting smaller with the inclination of the column. The vertical stresses as well as the principal effective stresses show minimal differences between Mohr Coulomb and the shotcrete model when the inclination is decreasing.

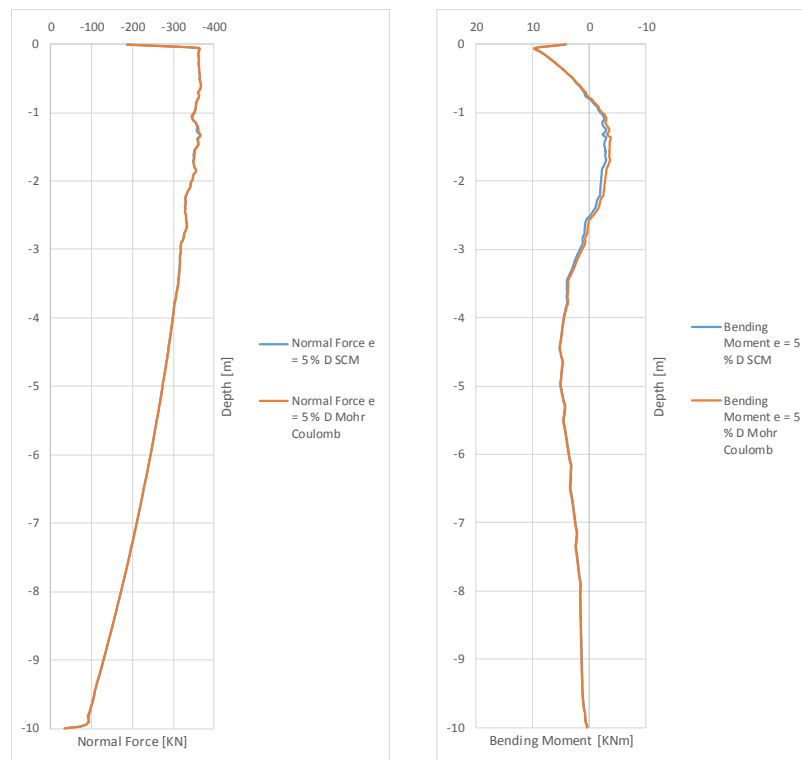


Fig. 71 Structural forces for a column with $e = 5 \% D$ (MC and SCM)

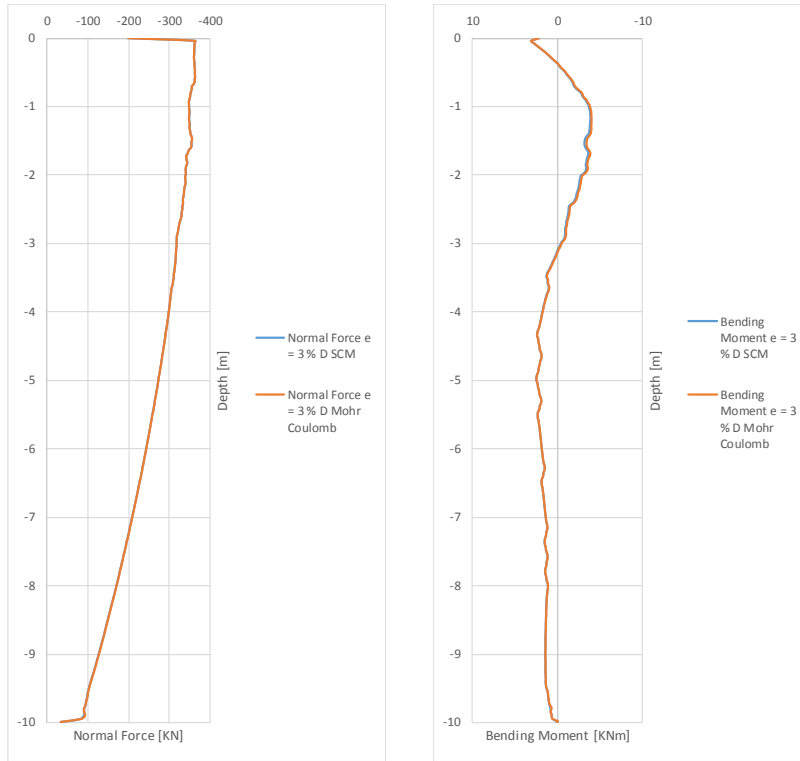


Fig. 72 Structural forces for a column with $e = 3\% D$ (MC and SCM)

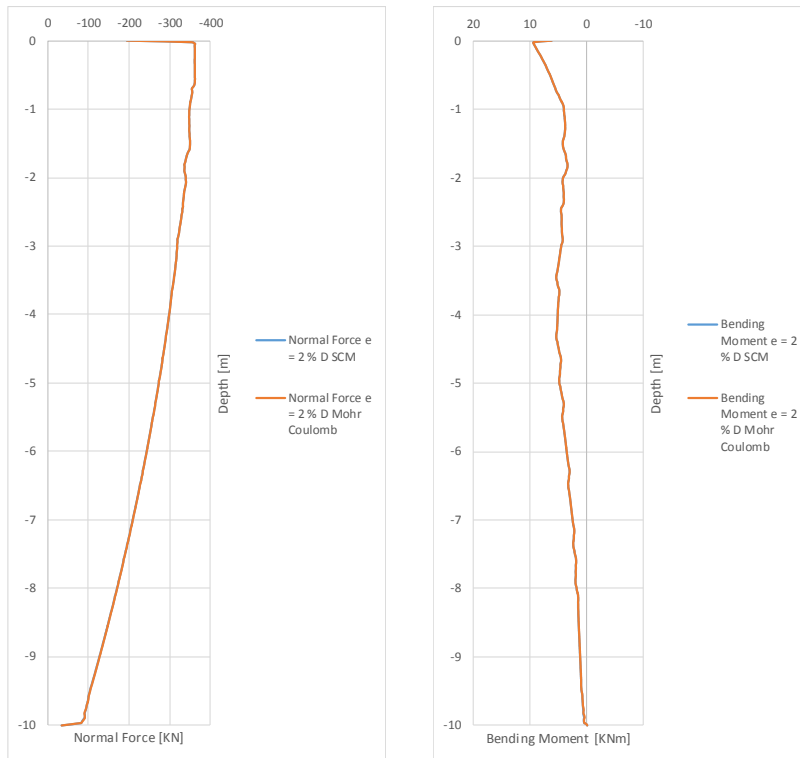


Fig. 73 Structural forces for a column with $e = 2\% D$ (MC and SCM)

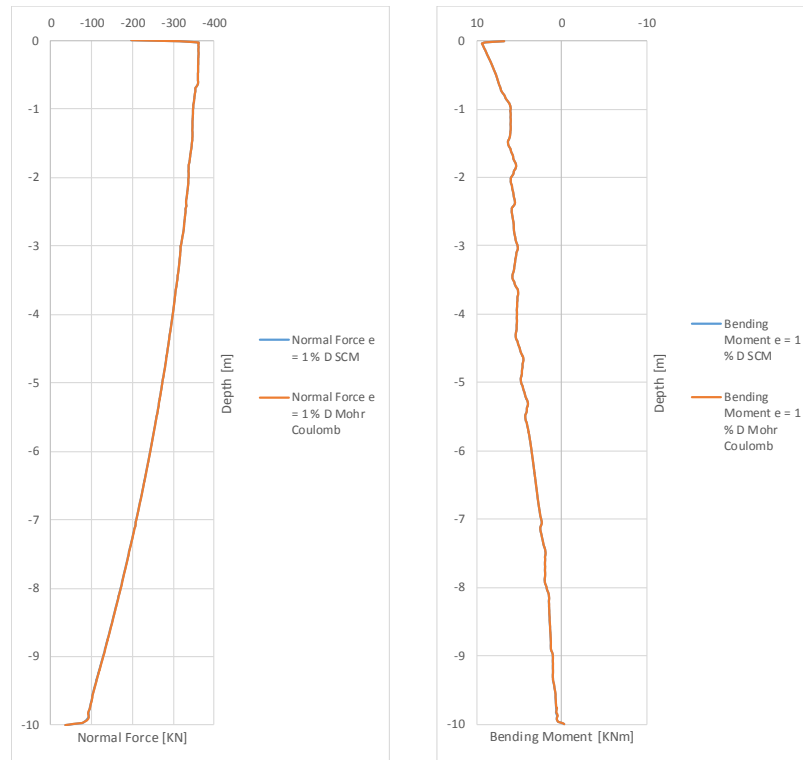


Fig. 74 Structural forces for a column with $e = 1\% D$ (MC and SCM)

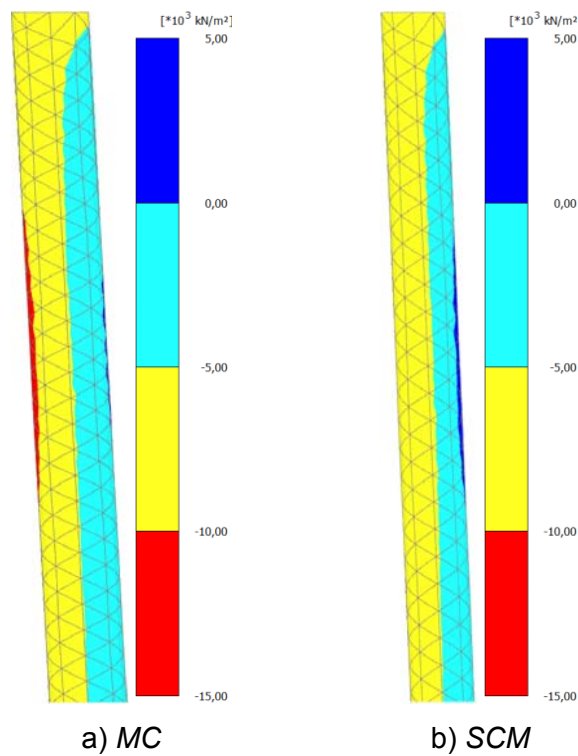


Fig. 75 Vertical stresses in the column for $e = 5\% D$ (MC and SCM)

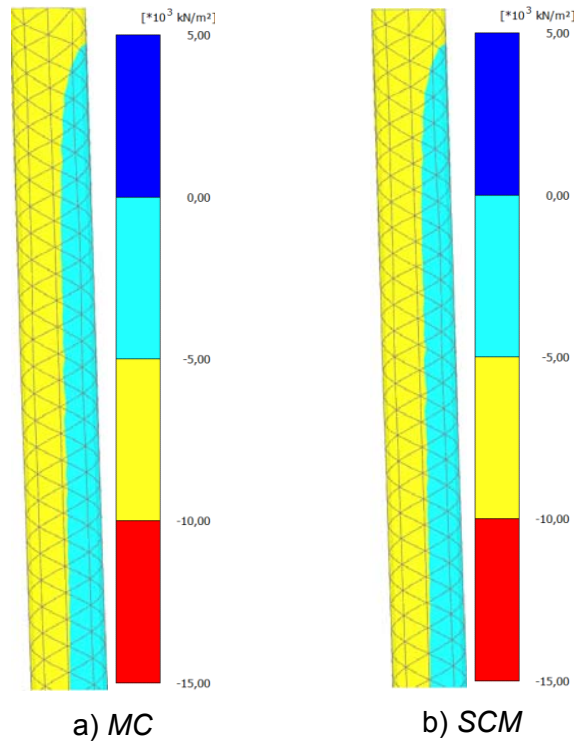


Fig. 76 Vertical stresses in the column for $e = 3 \% D$ (MC and SCM)

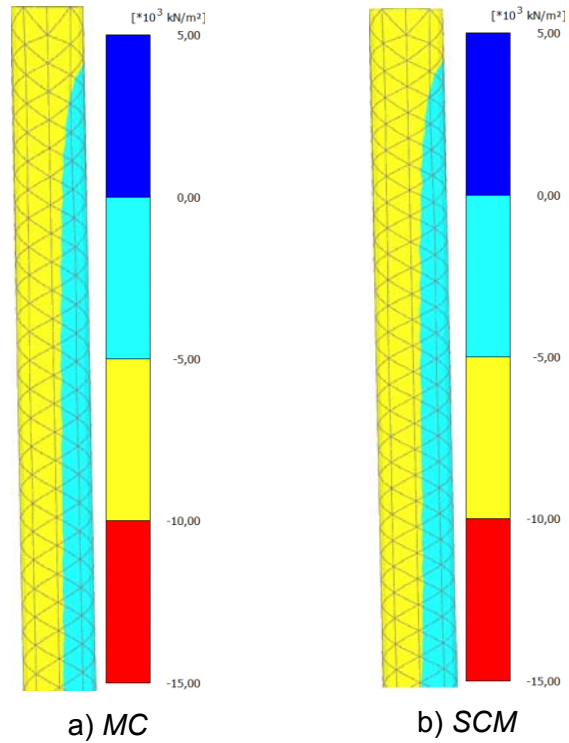


Fig. 77 Vertical stresses in the column for $e = 2 \% D$ (MC and SCM)

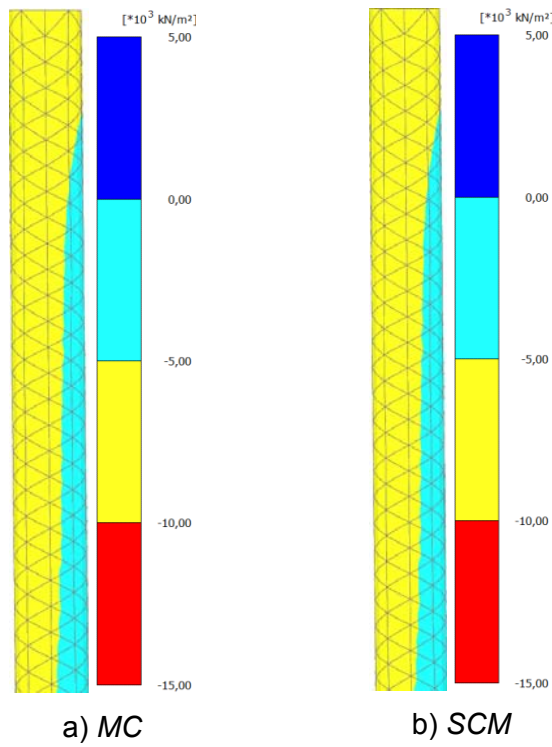


Fig. 78 Vertical stresses in the column for $e = 1 \% D$ (MC and SCM)

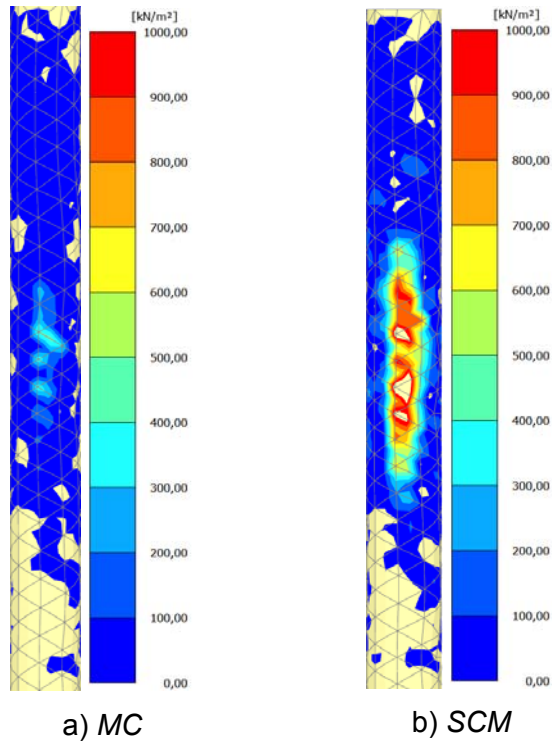


Fig. 79 Principal effective stresses σ'_3 (only tension) for $e = 5 \%$ (MC and SCM)

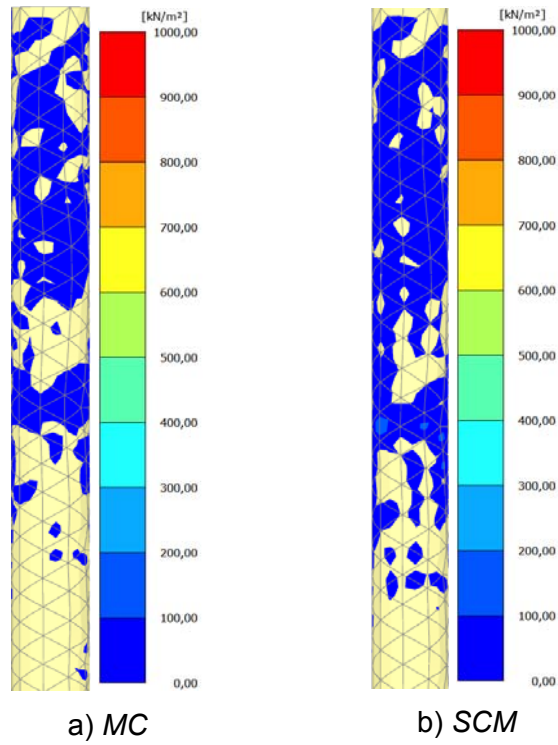


Fig. 80 Principal effective stresses σ'_3 (only tension) for $e = 3\%$ (MC and SCM)

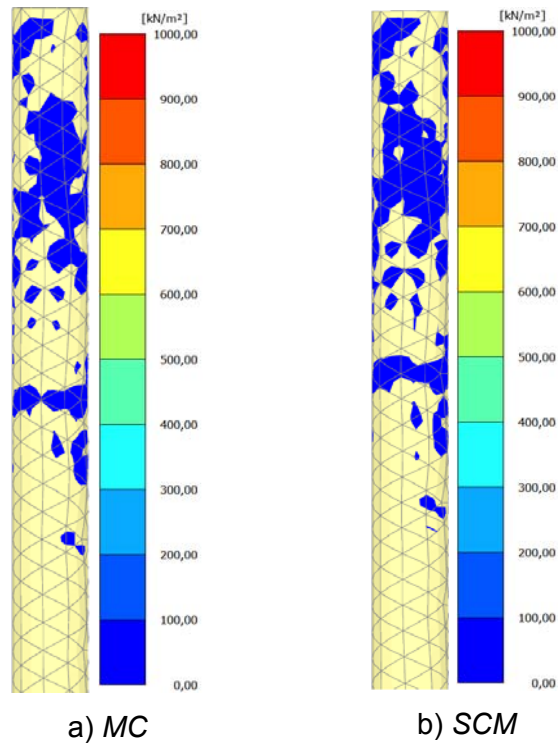


Fig. 81 Principal effective stresses σ'_3 (only tension) for $e = 2\%$ (MC and SCM)

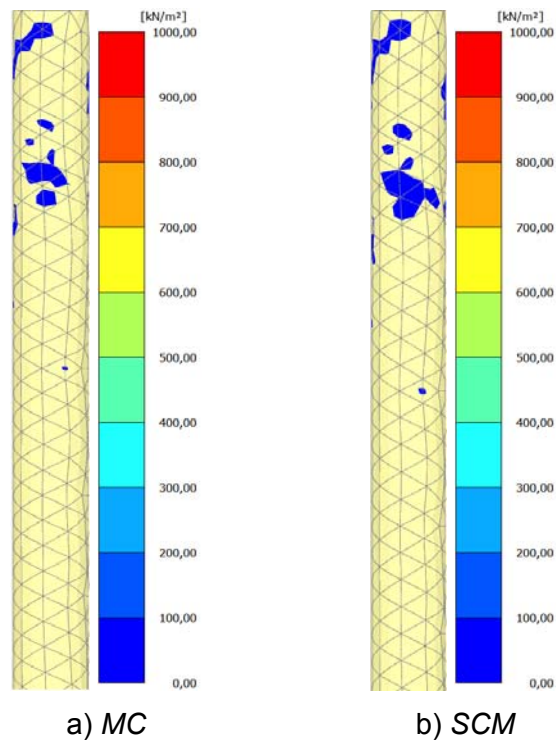


Fig. 82 Principal effective stresses σ'_3 (only tension) for $e = 1\%$ (MC and SCM)

13 Appendix B: Load-settlement trough embankment

In addition, the following graphs show the settlement trough below the columns for all examples of chapter 9.

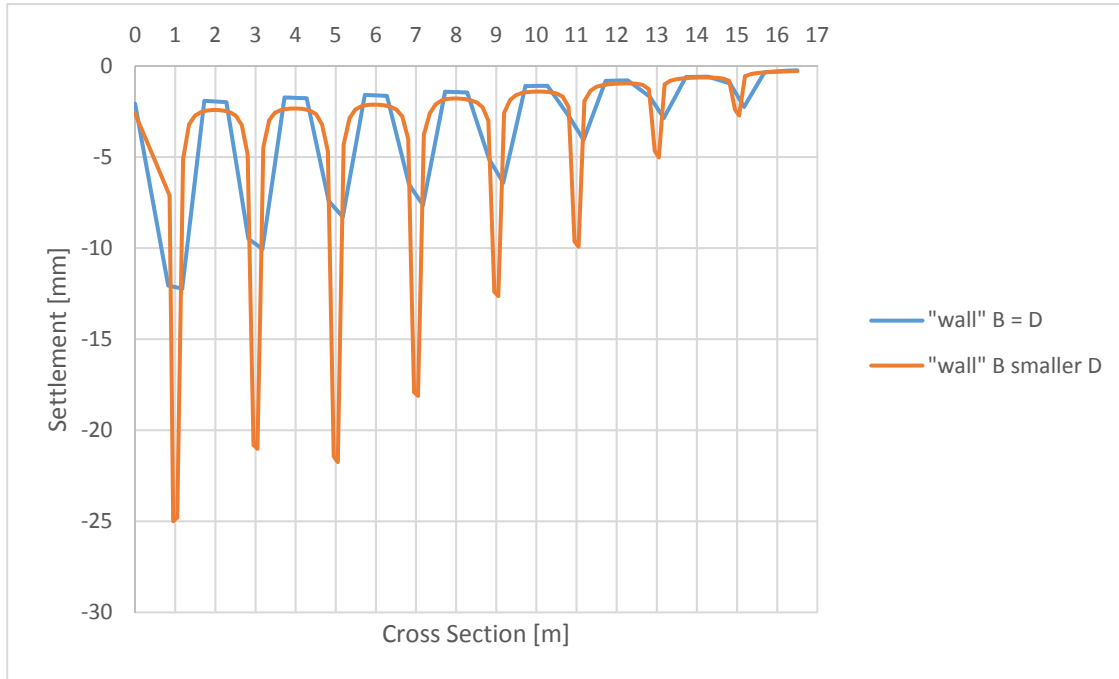


Fig. 83 Settlement trough below the columns

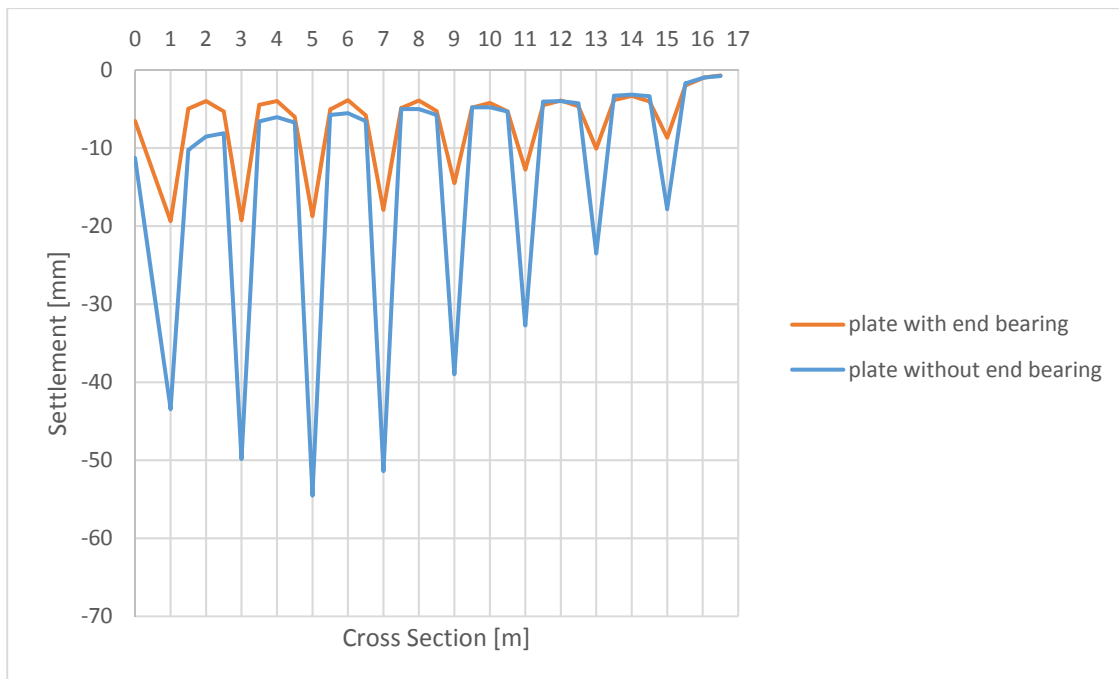


Fig. 84 Settlement trough below the plates

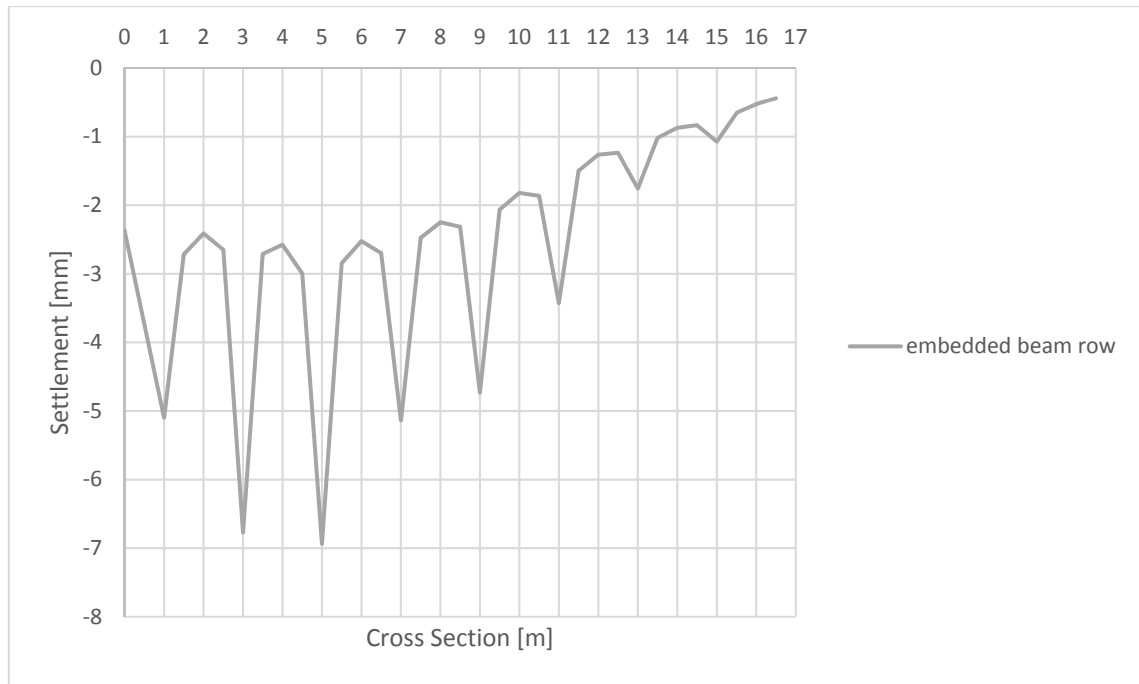


Fig. 85 Settlement trough below the embedded beam row

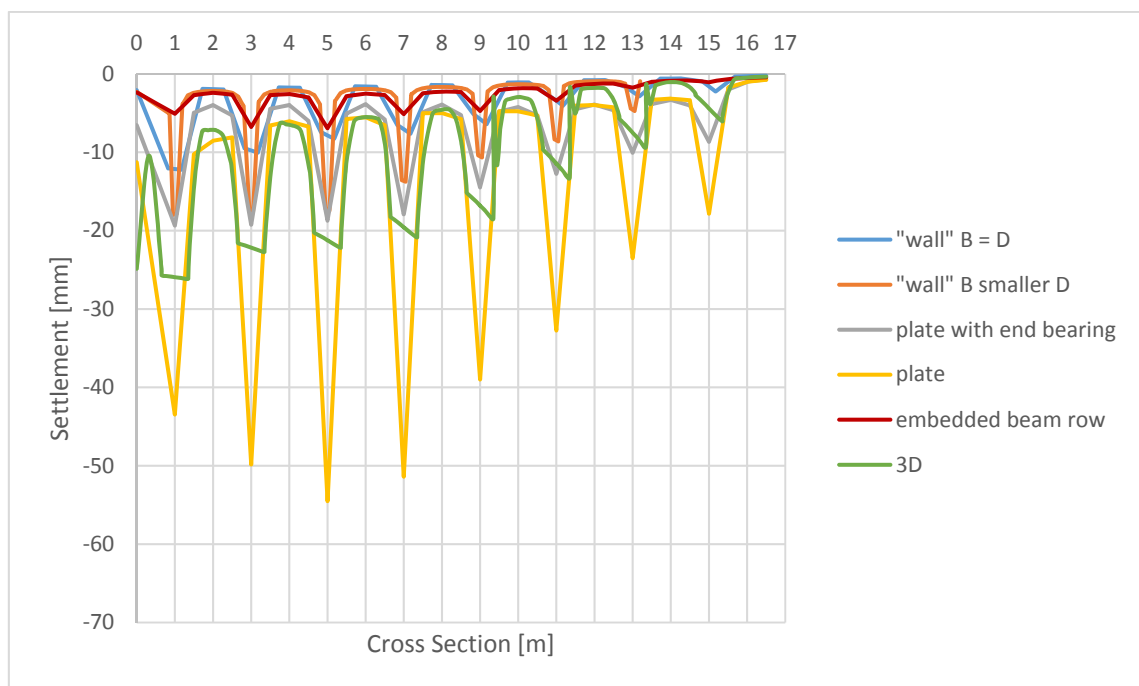


Fig. 86 Load-settlement trough below the columns for all examples